INFRASOUND FROM HAWAIIAN TO PLINIAN ERUPTIONS: CONSTRAINING VOLCANIC SOURCE PARAMETERS

A DISSERTATION SUBMITTED TO THE GRADUATE DIVISION OF THE UNIVERSITY OF HAWAI‘I AT MĀNOA IN PARTIAL FULFILLMENT OF THE REQUIREMENTS FOR THE DEGREE OF

DOCTOR OF PHILOSOPHY

IN

GEOLOGY AND GEOPHYSICS

AUGUST 2010

By

David E. Fee

Dissertation Committee:

Milton Garces, Chairperson
Matthew Patrick
Fred Duennebier
Roy Wilkens
Mark Merrifield

ACKNOWLEDGEMENTS

This body of work and degree would not be possible without the extensive help and support from many people. For the past six years Milton Garces has been my advisor, employer, and friend. I started with him and the University of Hawaii Infrasound Lab fresh out of graduate school. The next three years I was traveling around the world deploying infrasound arrays and going to conferences. It was through this experience that my interest in research and becoming a Ph.D. was reinvigorated. Milton has taught me much about infrasound and gave me the opportunity to study volcanoes, something that I have always wanted. I will always look back on my time at ISLA fondly. Also, I am not sure I would have made it through all of this sanely without lunchtime kiteboarding and surf breaks.

Numerous colleagues kept me interested and on the right track along the way. Roger Waxler has been a great resource on acoustics and infrasound propagation. Curt Szuberla has answered many questions and kept things fun and interesting, and I look forward to working with him in the future at the University of Alaska Fairbanks. Darren Hart, David Green, Laslo Evers, Michael Hedlin, Kris Walker, and many others have been helpful resources and were always available for post conference beers. Doug Drob provided the G2S files and is another great source of information. Darcy Ogden has also been a great resource on volcanic jetting. Claus Hetzer has at all times been an invaluable resource on all things.

The Acoustic Surveillance for Hazardous Eruptions (ASHE) project provided the impetus (and funding) for much of this work. Hugo Yepes, Patricio Ramon, and the rest of the Instituto Geofisco in Ecuador made our Tungurahua Volcano work possible, as well as being gracious hosts to our two memorable visits to Ecuador. Hank Bass and David McCormack provided some of the funding and vision for the project. Jack Seiner and Hank Bass gave me and Robin Matoza a great week-long introduction to jet noise at the University of Mississippi.

Members of the Hawaiian Volcano Observatory have also been very helpful. In particular, Tim Orr, David Wilson, Paul Okubo, Rick Hobblitt, Mike Poland, Don Swanson, Jim Kauahikaua, and Matt Patrick. Matt has been a great resource, collaborator,

and friend, and I feel lucky to have worked with and have him on my committee. Frank Trusdell and Zoe Thorne have also been very gracious in hosting our array. Bernard Chouet and Phil Dawson were extremely helpful in our understanding of Kilauea. Bernard has also served as an invaluable mentor.

The various employees at ISLA have made my work both enjoyable and worthwhile. James Robertson has always been there to listen when I needed to talk, and was a great travel partner. Joe Park has an immense knowledge of acoustics and science in general, and was more than glad to share it. Grace Furuya has any answer to any question, and has made my life as a student and employee much easier. Eric Pilger provided invaluable networking expertise and took quite a lot of stress off me. A big thanks to the rest of my committee, Fred Duennebier, Roy Wilkens, and Mark Merrifield, for helping me along the way and being great resources on academia and science in general. Andy Harris briefly served on my committee and pointed me the right way on a number of topics.

Chapter 2 will soon be submitted to *Geophysical Research Letters*. Chapter 3 is currently in review as: Fee, D., M. Garces, M. Patrick, B. Chouet, P. Dawson, and D. Swanson (in review), Infrasonic Harmonic Tremor and Degassing Bursts from Halema`uma`u Crater, Kilauea, *Journal of Geophysical Research-Solid Earth*. Chapter 4 is published in full as: Fee, D., M. Garces, and A. Steffke (2010), Infrasound from Tungurahua Volcano 2006–2008: Strombolian to Plinian eruptive activity, *Journal of Volcanology and Geothermal Research*, *193*, 67-81. Chapter 5 is currently being published in full as: Fee, D., A. Steffke, and M. Garces (in press), Characterization of the 2008 Kasatochi and Okmok eruptions using remote infrasound arrays *Journal of Geophysical Research-Atmospheres*. Financial support was provided by NSF grant EAR-0609669 and NOAA via University of Mississippi subcontract 09-09-022. Other co-authored papers of mine are mentioned in the subsequent chapters. A huge thanks to all coauthors on all papers, none of it would have been possible without their help.

Robin Matoza and Andrea Steffke have both been more than just great collaborators. Due to my unique graduate student situation away from the UH campus, Andrea gave me a great deal of insight on what is required of students. I would not have been able to graduate without her. She also taught me a lot about remote sensing, quite a

feat considering I started from not knowing anything. I met Robin when he was just beginning as a graduate student, and we hit it off right away. As he (and I) progressed along our academic paths, our mutual interest for science, infrasound, and volcanoes kept us in touch often. His knowledge, collaboration, and encouragement has made anything I have been involved with that much better. Further, many of my life's concerns have been dealt with over a beer (or email) with Robin. Above all I feel that I have made two lasting friends.

Lastly, I want to thank my family. As long as I can remember, my parents and sister have been supportive of my endeavors, and this is time is no different. Whenever I was feeling stressed or overworked my family knew just the right thing to say to help me get through it. I feel blessed to have such an amazing family. Finally, I am extraordinarily grateful to my wonderful wife Elizabeth. We started our journey together roughly the same time as I started my Ph.D., and she has put up with all my late nights and often hectic schedule without a complaint. Her unwavering support, interest, and love have made this all possible.

ABSTRACT

Volcanoes produce a diversity of acoustic signals that may propagate thousands of kilometers through the atmosphere. These signals are indicative of the volcano's eruption style and dynamics. This dissertation details the diverse infrasound from four volcanoes: Kilauea, Hawaii; Tungurahua, Ecuador; and Okmok and Kasatochi, Alaska. I demonstrate the ability to constrain eruption source parameters, such as location, onset, duration, intensity, and escalation, by combining infrasound and other geophysical techniques.

Kilauea Volcano produced two unexpected fissure eruptions in 2007 that varied spatially and temporally. Infrasound was the first technology to detect the 19 June fissure eruption. Changes in the infrasonic source azimuth from the 21 July fissure eruption are used to infer rupture timing of individual fissure segments. In 2008 activity returned to Halema'uma'u Crater, Kilauea after a 25 year hiatus. Numerous degassing bursts produced infrasound, including the initial vent-clearing event. Near-continuous harmonic tremor followed the initial burst. The harmonic tremor and degassing burst signatures are consistent with a process which excites a steam-filled cavity overlying the magma surface into Helmholtz and acoustic resonance.

Between 2006-2008, Tungurahua Volcano produced over 20,000 transient explosions and numerous sustained explosive eruptions. The spectrum of the sustained eruptions is recurrent, readily recognizable, and indicative of volcanic jetting and significant atmospheric ash injection. Broadband, sustained low-frequency (<0.5 Hz) infrasound appears to be indicative of stratospheric emissions. This work has direct civil defense application in providing notifications of ash injection into the atmosphere. Using

previous eruptions as case studies, an automatic detection system was designed and successfully notified aviation authorities of the onset, escalation, and cessation of a hazardous February 2008 eruption within 6 minutes.

The 2008 Plinian eruptions of Okmok and Kasatochi produced stratospheric ash clouds and infrasound focused below 0.5 Hz that was detected thousands of kilometers away. Ray tracing and parabolic equation modeling are performed to determine the propagation path, travel time, and attenuation for the eruptions. The long-range infrasound from Kasatochi displays a characteristic jet noise-like spectrum regardless of ash content. Future detailed volcano infrasound studies will assist in hazard mitigation, and could advance the understanding of volcanic processes and acoustic propagation considerably.

TABLE OF CONTENTS

LIST OF TABLES

LIST OF FIGURES

CHAPTER 1: INTRODUCTION

By nature volcanoes are a dynamic, complex, and intriguing part of earth's system. Monitoring and understanding volcanic eruptions remains a challenging task for scientists. Numerous techniques and advances over the years have been employed, with varying degrees of success. For years volcano seismology has been the primary technique used to examine subsurface volcanic activity. Volcano acoustics is a relatively new field and provides a means to record the atmospheric oscillations of active volcanoes at distances of meters to thousands of kilometers, providing insight into the depressurization and dynamics of the system. Using specialized recording equipment and data processing techniques, insight into the eruptive activity of volcanoes can be discerned and used for hazard mitigation. This chapter serves as an introduction to the author's dissertation research with a brief review of the relevant literature and topics.

1.1 Infrasound Background

Sound energy is produced by a multitude of oscillatory processes. Once produced, sound energy travels as a wave through a medium. In the atmosphere sound waves pass through a gas, compressing and rarifying the medium. The motion of the sound wave is in the same direction as its propagation, thus it is a longitudinal or compressional wave [*Pierce*, 1981]. Sound is also produced over a wide range of frequencies. Audible sound lies between ~20-20,000 Hz, with sound energy above 20,000 Hz classified as ultrasound and that below 20 Hz as infrasound, the focus of this dissertation. At even lower frequencies (and longer wavelengths) gravity begins to act as a restoring force, creating acoustic-gravity waves. The cut-off frequency for acoustic waves is approximately 3 mHz [*Evers and Haak*, 2010].

The speed of sound c, within an ideal gas is given by:

$$c = \sqrt{\gamma RT} \qquad (1.1)$$

where γ is the specific heat ratio, R is the universal gas constant, and T is the temperature [*Pierce*, 1981]. For a typical atmospheric temperature of 20°C at sea level, the sound speed is 343 m/s. Supersonic sources travel faster than the speed of sound and produce nonlinear shock waves, which decay and eventually transition to linear sound waves. Subsonic gravity waves in the atmosphere occur at very low frequency and propagate at velocities less than 10 m/s [*Evers and Haak*, 2010]. Wind may also affect the sound speed, and will be discussed in Section 1.4.2.

Attenuation of sound waves occurs from two sources: absorption and geometrical spreading. Acoustic energy loss by absorption in the atmosphere is divided into two types: classical and rotational. Classical losses are associated with the transfer of energy from the kinetic energy of the gas molecules to heat, while rotational losses are associated with excitation of the gas molecule's energy states. Absorption varies in the atmosphere with height, and with frequency approximately to the power of 2. The relatively low amount of absorption in the infrasound band (~10^{-6} dB/km at 0.1 Hz vs. ~2.4 dB/km at 125 Hz) allows infrasound to propagate long distances [*Sutherland and Bass*, 2004]. Geometrical spreading occurs as a consequence of wavefront expansion. For

a point source in an unbounded homogeneous medium, spherical spreading prevails and the pressure decreases as $1/r$, where r is the distance. Cylindrical spreading can result from either an extended (line) source or where the normally spherically spreading wave is ducted. The pressure loss for cylindrical spreading occurs as $1/\sqrt{r}$ [*Pierce*, 1981]. Energy in the wave is conserved as it spreads but not as it is absorbed.

Infrasound sources are plentiful in both the man-made and natural world in the form of: man-made explosions [*Ceranna et al.*, 2009], aurora [*Wilson*, 1967], lightning [*Assink et al.*, 2008], surf [*Garces et al.*, 2006], wave-wave ocean interactions [*Waxler and Gilbert*, 2006], meteors [*ReVelle*, 1975], high-speed aircraft [*Liszka and Waldemark*, 1995], earthquakes [*Mikumo*, 1968], and tsunamis [*Le Pichon et al.*, 2005a]. This dissertation focuses on the wide range of infrasound from volcanoes, another plentiful acoustic source [*Garces et al.*, in review].

Specialized microphones deployed to detect these low frequency pressure oscillations record the pressure changes relative to the ambient atmospheric pressure. Compared to the sea level atmospheric pressure ($\sim 10^5$ Pa), the amplitude of recorded infrasound signals are usually less than 5 Pa. The primary source of recorded incoherent noise is wind, and extensive research has gone in to reducing the effects of wind-induced noise [*Christie and Campus*, 2010; *Walker and Hedlin*, 2010].

In 1996, the Comprehensive Nuclear-Test-Ban-Treaty (CTBT) was adopted by the United Nations to ban all testing of nuclear test explosions. To enforce this treaty, the International Monitoring System (IMS) was constructed and consists of global networks of seismic, infrasound, hydroacoustic, and radionuclide stations. The infrasound portion consists of 60 planned arrays dispersed throughout the globe to detect atmospheric nuclear tests (Fig. 1.1). The development of the IMS has led to a surge in infrasound research and technology advancements [*Christie and Campus*, 2010].

1.2 Volcano Acoustics

As magma rises within the earth, pressure oscillations are created from fluid dynamic processes and the brittle fracturing of rock. These oscillations propagate into the

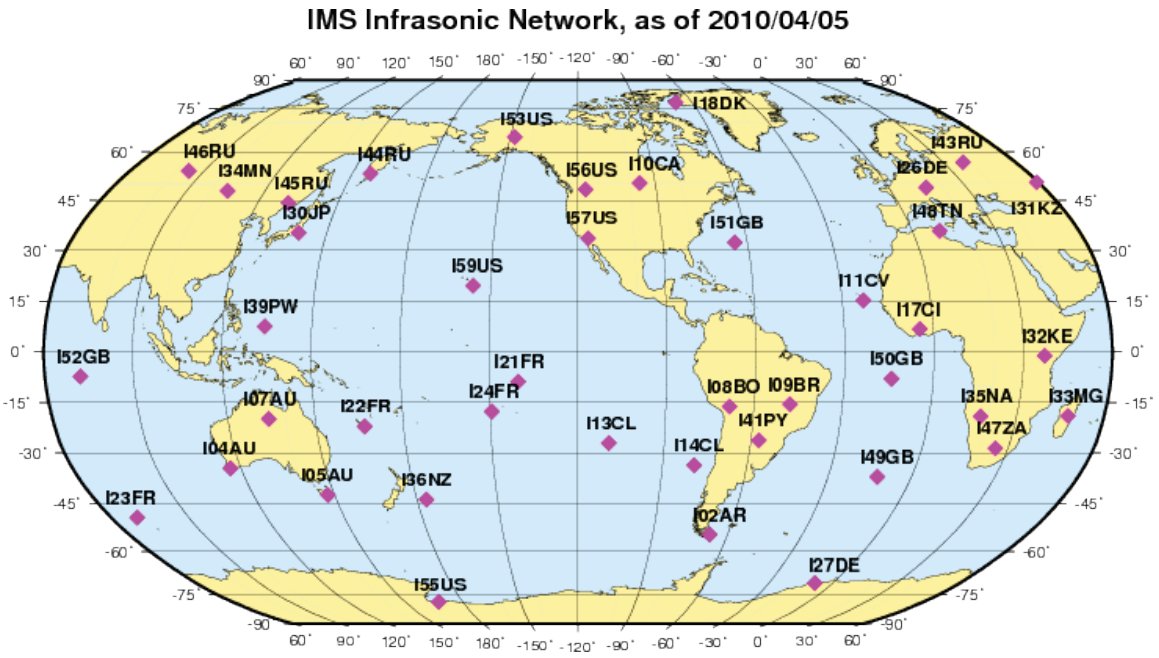

Figure 1.1 Map of the IMS Infrasound Network. Purple diamonds indicate the currently installed infrasound arrays and their five letter designation. Several other arrays are planned but are not installed as of 2010/4/5. Image courtesy of www.rdss.info (Science Applications International Corporation).

ground in the form of seismic energy and/or into the atmosphere in the form of acoustic energy. The majority of the acoustic oscillations lie within the infrasound band due to the large length scales often present at volcanoes. The basic model for an acoustic signal from a volcano is [*Garces et al.*, in review]:

$$p(t) = s(t) * l(t) * g(t) \qquad (1.2)$$

where $p(t)$ is the observed signal, $s(t)$ is the source-time function at the source (also known as the excitation mechanism), $l(t)$ are local resonance effects, $g(t)$ is the atmospheric transfer function, and * indicates convolution. Thus to gain a proper

understanding of the source, one must characterize *l(t)* and *g(t)*. This topic will be the focus of later chapters.

1.2.1 Brief History of Volcano Acoustics

The first recorded and detected instance of volcano infrasound occurred with the 1883 eruption of Krakatoa Volcano [*Evers and Haak*, 2010]. The Indonesian volcano erupted cataclysmically in August 1883, producing powerful explosions, tsunamis, and ash and gas plumes that affected world climate. Numerous explosions were detected worldwide on barographs, and pioneering research was able to determine these signals traveled as acoustic waves high in the atmosphere. The first microphone studies began in 1906 by Frank Perett, in which he studied numerous audible volcanic sounds, including those from Kīlauea Volcano, Hawaii [*Perret*, 1950]. *Richards* [1963] made the first recorded sounds from submarine and airborne volcanoes and categorized the eruptive activity based on their acoustics. *Woulff and McGetchin* [1975] followed with ground-breaking work on correlating a volcano's acoustics with fluid mechanical processes, focusing on the type of acoustic radiation from different degassing styles. More recent volcano acoustics work is presented in the following sections.

1.2.2 Volcano Acoustic Classification and Nomenclature

The general types of volcanic activity each have characteristic acoustic signals. Infrasonic tremor is perhaps the most common and varied volcano acoustic signal, and is broadly defined as a continuous vibration of the atmosphere lasting from seconds to months. Numerous types of volcanic tremor exist, largely classified based on their time and frequency domain characteristics. Harmonic tremor is distinguished by a frequency spectrum containing a fundamental peak and associated harmonics, while monochromatic tremor has a relatively simple spectrum with a single peak. Harmonic tremor is more common than monochromatic tremor. Gliding refers to the tremor's spectral peaks changing frequency over time. Broadband tremor has a wide frequency range with no sharp spectral peaks. Spasmodic tremor is continuous in time with amplitude variations. Banded or episodic tremor has bursts of tremor separated in time, with the bursts resembling "bands" on a spectrogram [*Garces et al.*, in review; *Konstantinou and*

Schlindwein, 2002]. Similar tremor nomenclature exists in volcano seismology. Turbulence related sound from high-velocity gas flow (jet noise) at volcanic vents has also been postulated [*Matoza et al.*, 2009a; *Woulff and McGetchin*, 1975], and may resemble broadband tremor in the time and frequency domain.

Explosions are transient events characterized by a rapid volume expansion (compression) into the atmosphere followed by a coda of a few to tens of seconds [*Garces et al.*, in review]. Volcanic explosions have a wide variety of characteristics and at times complicated source-time functions, but typically have impulsive onsets and durations of seconds to minutes. They are commonly associated with Strombolian and Vulcanian eruptions (Section 1.2.3.2), but can occur during nearly every type of activity.

To further classify volcanic seismoacoustic oscillations, signals have been classified based on their period (inverse of frequency): very long period (VLP) with dominant periods between ~2-100 seconds (0.02-0.5 Hz), long period (LP) between ~0.2-2 s (0.5-5 Hz), and short period (SP) greater than ~0.2 s (5 Hz) Extensive work in volcano seismology has shown that volumetric sources associated with fluid-filled conduits and cracks beneath volcanoes can generate VLP and LP events. The unique signal characteristics of seismic LPs are: a broadband onset, coda of tens of seconds to minutes focused in the LP band, and spectral peaks independent of source azimuth and distance. The rapid collapse of the crack may create the broadband onset, while the coda is produced by interface (crack) waves propagating within the fluid. LP events have further been shown to be possible precursors to an eruption, as they are characteristic of shallow magmatic and hydrothermal activity [*Chouet*, 1996]. It has also been postulated that tremor may represent the continuous activation of an LP source due to their often common signal characteristics [*Chouet*, 1985]. Infrasound VLPs and LPs may or may not be related to their seismic counterpart [*Johnson et al.*, 2008b; *Matoza et al.*, 2009b], and will be discussed in subsequent sections. SP events are often associated with brittle failure and have more traditional double-couple source mechanisms from tectonic forces [*Chouet*, 1996].

1.2.3 Types and Sources of Volcano Infrasound

Eruptive activity can broadly be assigned to categories based on the viscosity of the magma and its subsequent eruptive activity. These categories are by no means comprehensive, and volcanoes can exhibit multiple types of activity. Below are the various eruption categories and a brief overview of the observations and acoustic source models.

1.2.3.1 Hawaiian

Hawaiian eruptive activity is the least explosive due to the low viscosity of the magma, either basaltic or basaltic andesite. As magma rises within the earth it decompresses. The relatively low viscosity in basaltic magma allows gas to exsolve from the melt and escape into the atmosphere with relatively little vigor. Hawaiian eruptions typically consist of long lived, non-explosive, low-level effusive eruptions. The gas phase in the magma during passive effusive exists as relatively small bubbles rising through the magma [*Vergniolle and Mangan*, 2000].

Seismoacoustic signals from Hawaiian eruptive activity display a wide range of characteristics. Infrasound signals from Kīlauea Volcano, Hawaii have been associated with the primary degassing locations and produced near continuous, broadband infrasonic tremor lasting from minutes to years [*Fee and Garces*, 2007; *Garces et al.*, 2003; *Matoza et al.*, in review]. The source of this tremor has been postulated as collective oscillations of bubbles in the shallow volcanic conduit [*Matoza et al.*, in review]. The theory of a single resonating bubble can be extended to "bubble clouds" oscillating as a group. For a bubble cloud of length-scale L_b the resonant frequencies are described by:

$$f_n = \frac{nc_{eff}}{2L_b} \qquad (1.3)$$

where n = 1, 2, 3, . . ., and c_{eff} is the effective sound speed of the liquid-bubble mixture. The critical parameter for Eq. 1.3 is the effective sound speed, as this can be complex due to the viscosity and void fraction within magma-gas mixture [*Garces*, 2000]. Seismic

tremor at Pu‘u ‘Ō‘ō may similarly be related to collective bubble oscillations coupling into the earth [*Chouet*, 1996].

Open conduits and cavities confining the degassing locations at Kīlauea are also potential acoustics sources. Harmonic tremor at Pu‘u ‘Ō‘ō Crater, Kīlauea may be related to flow-induced oscillations related to the unique cavity configuration there. Chapter 3 discusses the acoustic excitation of the gas-filled cavity at Halema’uma’u crater, Kīlauea. The acoustic excitation of lava tubes also appears plausible [*Garces et al.*, 2003; *Matoza et al.*, in review].

Episodic tremor at Kīlauea has been detected at numerous locations. *Patrick et al.* [in review] detail how the cavity at Halema’uma’u Crater experiences cyclical ~2-10 minute filling and draining episodes. The rise and lowering of the lava surface is correlated with variations in degassing and tremor amplitude. The cyclic process begins with gas accumulation beneath a relatively impermeable lava surface, raising the lava surface within the cavity. The “capped” surface and lack of degassing produces little tremor. Eventually a threshold is reached and vigorous degassing ensues, producing elevated seismic and infrasonic tremor. As the gas is released the lava surface drops, and eventually the cycle repeats itself. This process also produces significant seismic VLP signals.

Lava fountaining is a more vigorous type of Hawaiian activity characterized by sustained jetting of gas and molten clots. Fountaining occurs when the gas content within the magma rises above ~70%, creating annular flow within the conduit and subsequent gas jetting at the surface [*Vergniolle and Mangan*, 2000]. Although relatively common, only distant, relatively low signal-to-noise ratio (S/N) infrasound recordings of high level (e.g. >100 m) lava fountains have been made [*Liszka and Garces*, 2002]. Recent recordings of fissure eruptions with low level fountaining (<8 m height) have been made (Chapter 2). Other non-magmatic sources of infrasound have been detected at Kīlauea, including lava bench collapses and rockfalls.

1.2.3.2 Strombolian and Vulcanian

Strombolian and Vulcanian activity are both characterized by similar acoustic signals, but differ in energy and time scales. Strombolian eruptions primarily involve

relatively low energy, recurring explosions and have slightly higher viscosity magma than Hawaiian systems. Bubbles within the magma coalesce to form large pockets of gas (slugs) that fill the width of the conduit. Degassing at the surface is then characterized by the episodic release of these discrete gas accumulations [*Vergniolle and Mangan*, 2000]. If the slug arrives with a low overpressure, relatively passive "puffing" events occur, while higher overpressured slugs may result in explosive bubble bursting at the surface. *Jaupart and Vergniolle* [1988] used laboratory models to show that a slug may form when accumulation of many small bubbles reaches a critical threshold, causing the bubble accumulation to collapse into a foam, creating a gas slug. Seismoacoustic sources within the conduit, rather than at the top, have also been proposed. *Buckingham and Garces* [1996] postulated that if a bubble rises within the magma column and passes into a region of much lower density, the bubble will undergo rapid, violent expansion and produce an "explosion" signal. The bubble then overshoots its equilibrium radius and collapses, only to overshoot its equilibrium radius again and begin a new expansion/contraction cycle. The acoustic signal would then radiate into the earth (seismic) and assuming an open-vent system, into the atmosphere (infrasound).

Acoustic observations of Strombolian eruptions typically consist of short duration compressional onsets, followed by a slightly longer duration rarefaction and coda of a few to tens of seconds. At Stromboli Volcano, Italy, the type locale for Strombolian eruptions, two main types of explosions have been observed: high amplitude (20-80 Pa at 350 m) with short durations (3-5 s) and lower amplitude (10-30 Pa at 350 m) with longer (5-15 s), more complex codas [*Harris and Ripepe*, 2007; *Ripepe and Marchetti*, 2002]. *Johnson et al.* [2008a] used high resolution video and acoustic data to model the source of Strombolian eruptions at Mt. Erebus, Antarctica as overpressured gas slugs reaching the surface and bursting, followed by short duration jetting. The acoustic waveforms at Erebus displayed the typical Strombolian explosion features. Infrasonic tremor is also common in Strombolian systems [e.g. *Garces et al.*, 1998b], and may be due to gas release at the lava/air interface [*Ripepe et al.*, 1996].

Vulcanian eruptions also typically have discrete degassing episodes, although they involve a higher overpressure and degree of magma fragmentation. Ballistic ejecta accompany the explosions, and ash plumes may reach heights of up to 20 km. Ejecta

have been found over 5 km from the source for some of the largest Vulcanian explosions, necessitating ejection velocities up to 400 m/s. Due to the higher energy and degree of fragmentation, Vulcanian eruptions pose a higher risk to aviation and local communities than Strombolian eruptions [*Morrissey and Mastin*, 2000].

Numerous acoustic studies have detailed Vulcanian eruptions with short duration, impulsive onsets followed by long codas lasting minutes [*Johnson et al.*, 2004; *Petersen et al.*, 2006], indicating continued degassing. The coda often resembles, or could be considered a form of, infrasonic tremor. Interestingly, the spectral peaks of the tremor following the explosions often exhibit gliding, or a change in frequency with time while keeping their spacing. This may be due to changes in the sound speed within the magma [*Garces et al.*, 1998b]. *Marchetti* [2009] demonstrates how using infrasound and thermal infrared data can help discriminate between Strombolian and Vulcanian explosion style and give insight into plume dynamics.

Vulcanian explosions have been postulated to result from two main processes: the explosive failure of a "capped" conduit (lava plug) and the interaction of magma and external water [*Morrissey and Mastin*, 2000]. At Sakurajima Volcano, Japan, a precursory compression just before the explosion of a lava plug is detected in the infrasound. *Yokoo et al.* [2009] used high resolution video imagery alongside infrasound to explain the precursory compression as the expansion of a gas volume beneath the lava plug causing the surface to swell. Vulcanian explosions may also result from similar processes as Strombolian explosions, although a greater amount of energy is necessary.

1.2.3.3 Subplinian and Plinian

Subplinian and Plinian eruptions are high-energy, sustained eruptions producing massive eruption clouds that may extend well into the stratosphere and cause extensive ashfall. The high viscosity in the magma hinders bubble decompression and growth, resulting in a high degree of magma fragmentation. A Plinian eruption column consists of a high-velocity (100-400 m/s), momentum-driven, multiphase jet extending above the vent. As the hot jet entrains air and loses momentum, the eruption column becomes buoyancy driven and rises into the atmosphere until it obtains neutral buoyancy and spreads laterally [*Sparks et al.*, 1997].

The relative infrequency and hazard associated with Subplinian and Plinian eruptions make high-resolution infrasound recordings of them difficult. Low resolution barometers detected the global acoustic propagation from large Plinian eruptions, enabling basic insight into the location, source, and propagation path [e.g. *Goerke et al.*, 1965; *Tahira et al.*, 1996; *Wilson et al.*, 1966]. The advent and deployment of more sensitive and calibrated sensors, along with a better understanding of the atmosphere, has provided higher resolution records of Subplian-Plinian eruptions. Recently, *Matoza et al.* [2009a] and *Garces et al.* [2008] compiled acoustic records from large eruptions at Mount St. Helens, USA and Tungurahua Volcano, Ecuador. *Garces et al.* [2008] show how infrasound can be used to detect and identify hazardous eruptions. *Matoza et al.* [2009a] found the spectrum from these eruptions resembles the spectrum of man-made jet noise recordings. The acoustic spectrum from man-made jets has a characteristic shape consisting of a single broad peak, with the roll-off determined by the type of turbulence producing the noise [*Tam et al.*, 1996]. Further, it exhibits self-similarity, meaning its characteristic shape scales with the size and velocity of the source processes. Volcanic jets exhibit the same characteristic spectrum and self-similarity. This topic will be covered in more detail in Chapters 4 and 5.

1.2.3.4 Other Volcano Acoustic Signals

As mentioned before, volumetric VLP and LP events have been a major research area in volcano seismology [*Chouet*, 1996]. Recent work has shown that these events often have acoustic counterparts. *Yamasato* [1998] was the first to record infrasonic LP (ILP) events. *Matoza et al.* [2009b] recorded repetitive, impulsive ILP events from Mount St. Helens between 2004-2008. Interestingly, the acoustic signal characteristics were much different than the seismic. Finite difference modeling of these sources showed that the ILPs likely represent the broadband pressure excitation function of the collapse of a shallow hydrothermal crack. The pressure oscillation propagates through the shallow subsurface and then into the atmosphere. Infrasonic VLP (IVLP) events are rare and require large-scale atmospheric accelerations. *Moran et al.* [2008] recorded an IVLP event from a large rockfall at Mount St. Helens. Sustained IVLP signals have been shown to be indicative of large-scale jetting [*Matoza et al.*, 2009a] and stratospheric ash

emissions [*Garces et al.*, 2008]. Chapter 3 details transient IVLP signals at Kīlauea, while Chapters 4-5 present further evidence of sustained IVLP signals indicating significant ash emissions.

Pyroclastic Density Currents (PDCs) are dangerous lateral flows of hot gas and particles. They are commonly produced by Vulcanian, Subplinian, and Plinian eruptions and pose a grave threat to communities near volcanoes. The first acoustic recordings of a PDC were made at Mt. Unzen, Japan and were used in conjunction with seismicity to track their movement [*Yamasato*, 1997]. *Ripepe et al.* [2009] report higher resolution recordings of PDCs at Soufriere Hills Volcano, Montserrat. Collapses of remnant lava domes may also produce seismoacoustic signals [*Green and Neuberg*, 2005].

1.2.4 Resonance

Resonance is a natural consequence of unsteady fluid oscillations in bounded volcanic systems. Numerous types of resonance can occur, based on the ratio of the acoustic wavelength to the resonator dimensions, as well as the shape of the resonator and style of flow. Thus multiple types of resonance may occur within a single volcanic system at different frequencies [*Garces et al.*, in review; *Morse and Ingard*, 1968].

Volume resonance may occur when the acoustic wavelength is at least three times greater than the wavelength of the resonator [*Morse and Ingard*, 1968]. If the resonating volume has a relatively thin "neck" extending into the atmosphere, Helmholtz volume oscillations with wavelengths larger than the cavity may occur at a single frequency. The dominant Helmholtz oscillation frequency can be estimated by [*Kinsler et al.*, 1982]:

$$f_h = \frac{c}{2\pi}\sqrt{\frac{S}{Vk'}} \qquad (1.4)$$

where c is the sound speed, S is the area of the neck, k' is the effective length of the neck, and V is the cavity volume. This type of oscillation is analogous to an oscillating mass attached to a spring. Chapter 3 examines how degassing at Halema`uma`u Crater, Kīlauea excites the overlying cavity into Helmholtz resonance. At Halema'uma'u, the gas is

visibly pushed out of and sucked into the vent at frequencies consistent with the peak infrasonic tremor frequency.

When the acoustic wavelength is ~1/3-3 times the dimension of interest, standing acoustic waves may set up within the cavity and produce acoustic resonance [*Morse and Ingard*, 1968]. These waves are analogous to standing waves on a string, and can be viewed physically as constructively interfering echoes within the cavity. The eigenfrequencies, or natural cavity oscillation frequencies, of a narrow pipe are:

$$f_m = \frac{\left(m - \frac{1}{2}\right)c}{2L}, \qquad \text{where m = 1, 2, 3…} \qquad (1.5)$$

and

$$f_m = \frac{mc}{2L}, \qquad \text{where m = 1, 2, 3 …} \qquad (1.6)$$

where m is the mode number c is the sound speed, L is the length of the pipe, and m is the mode number. The first mode (m=1) is the dominant mode (fundamental), while higher order modes are termed overtones. Assuming the bottom of the pipe is closed, the boundary condition of the top of the pipe, either closed or open, determines whether eq. 1.5 (closed) or eq. 1.6 (open) applies. These two equations describe the longitudinal resonant modes parallel to the direction of propagation. However, the transverse modes (perpendicular to the direction of propagation) must also be considered for a volume. If the volume is circular, radial modes also need to be considered [*Buckingham and Garces*, 1996; *Pierce*, 1981]. In volcanic environments, acoustic resonance may occur both within a liquid-filled conduit or gas-filled cavity. Longitudinal and transverse resonance at Kīlauea is detailed in Chapter 3.

Geometrical acoustics occurs when the acoustic wavelength is less than 1/3 the resonator dimension [*Morse and Ingard*, 1968]. Due to the predominance of low frequency sound radiated by volcanoes, geometrical acoustics is usually not used.

1.2.5 Aeroacoustics

A new area of study in volcano acoustics is aeroacoustics, or the sound produced by turbulent fluid motion or aerodynamic forces interacting with solid surfaces [*Lighthill*, 1978]. As mentioned in Section 1.2.3.3, volcanic jetting (hence turbulence) can produce a prodigious amount of sound from fluid instabilities within the jet.

Although flow induced resonance has been studied extensively in acoustics, its application to volcanoes has been limited. *Matoza et al.* [in review] recognized that the harmonic tremor from Pu‘u ‘Ō‘ō Crater, Kīlauea Volcano may be related to persistent degassing and the unique crater geometry. They postulated that “hole tones” may result from a low velocity gaseous jet impinging on a boundary with a hole in it. The boundary acts to disrupt the gas flow and may create self-sustaining vortices.

The frequencies associated with aeroacoustic sources are often nondimensionalized using the Strouhal number (S_t):

$$S_t = \frac{fL}{U} \tag{1.7}$$

where f is the frequency, L is the length-scale of the process, and U is the flow velocity. *Rossiter* [1964] found that for the hole tone, the aeroacoustic loop frequency (f_a) can be estimated by [*Howe*, 1998]:

$$\frac{L}{U} + \frac{L}{c} = \frac{1}{f_a} \tag{1.8}$$

where L is the distance between the jet nozzle and solid boundary, U is the jet velocity, and c is the sound speed. Putting in realistic values for degassing at Pu‘u ‘Ō‘ō crater in early 2007 gives frequencies consistent with those recorded (~0.2-1 Hz) [*Matoza et al.*, in review]. Figure 1.2 shows the typical frequency spectrum from Pu‘u ‘Ō‘ō in April 2007 and a cartoon drawing of the bubble cloud oscillation and hole tone production. Numerous other types of flow induced resonances are well-known in acoustics [*Rockwell and Naudascher*, 1979] and may be applicable to volcanoes.

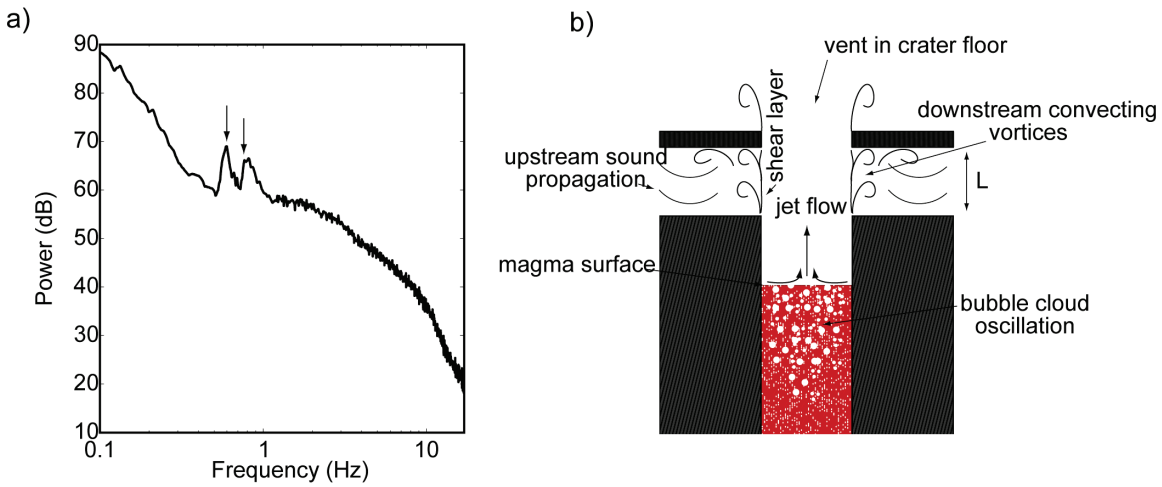

Figure 1.2 Spectrum and Hole Tone Production at Pu‘u ‘Ō‘ō. a) Typical spectrum from Pu‘u ‘Ō‘ō in April 2007, with two spectral peaks below 1 Hz and broadband tremor above 1 Hz. b) Cartoon drawing of a vent at Pu‘u ‘Ō‘ō. Oscillations of bubble clouds are potential sources for the broadband tremor in a). The spectral peaks in a) (black arrows) may be hole tones produced by interactions of the gaseous jet with the cavity walls and crater floor creating self-sustaining oscillations. Image modified with permission from Matoza et al. [in review].

1.3. Array Detection and Signal Identification

Groups of infrasound microphones are often placed in systematic configurations, termed arrays, to detect coherent acoustic waves. Once the signal is recorded, numerous techniques can be employed to detect coherent waves traveling across the array and determine their propagation speed and bearing (azimuth). A plane wave approximation is made for many array processing techniques. This assumes the acoustic field quantities change with time and with one spatial dimension, but do not change with position normal to the propagation direction [*Pierce*, 1981]. The two most commonly used detection methods in infrasound are the Progressive Multi-Channel Correlation Method (PMCC) [*Cansi*, 1995] and the Fisher Ratio [*Melton and Bailey*, 1957]. These methods determine

the back azimuth (bearing from north to the source) and apparent horizontal phase velocity (trace velocity), among other parameters. When an array is close to the source and in the near-field, the commonly used plane wave approximation is no longer valid and other methods should be used, possibly based on wavefront curvature [*Szuberla et al.*, 2006].

1.3.1 Array Processing

Noise, particularly wind-induced noise, often masks the infrasonic signal. Various techniques exist to increase the S/N of the signal, with the most common being time-delay beamforming. Plane-waves traveling across the array will arrive at the sensors at different times. Assuming the back azimuth and trace velocity of the plane-wave crossing the array is known, the time delay of the waveform arrival at the *i*th element is $d_i = r_i * u$, where r_i is the position vector from the center of the array and u is the slowness vector, defined as the inverse of the trace velocity. For an array of M sensors we can represent the pressure record as composed of the signal, $s(t)$, minus the delay time plus noise $n_i(t)$:

$$x_i(t) = s(t - d_i) + n_i(t) \qquad (1.9)$$

We can then remove the delay time from each sensor to get the time-delayed beamformed signal [*Thomas*, 2008]:

$$b(t) = s(t) + \frac{1}{M}\sum_{i=1}^{M} n_i(t + d_i) \qquad (1.10)$$

Other more advanced beamforming techniques also exist, such as adaptive beamforming [*Johnson and Dudgeon*, 1992]

The Pure State Filter (PSF) is a frequency-based technique that has been developed to increase the S/N of acoustic signals. The PSF provides a measure of the incoherent signal at each frequency by examining the spectral matrices, and then corrects the spectrum accordingly. It has been shown to increase the S/N by 10-15 dB [*Olson and Szuberla*, 2008].

Azimuth and trace velocity estimation are a crucial part of array processing. Beamforming over individual azimuths and velocities to determine the maximum beam power can be used, but is computationally intensive. Frequency-wavenumber (FK) analysis is an alternate, more efficient approach that processes the data in the frequency domain. A matrix of possible trace velocities and back azimuths is constructed. The energy is then computed at each wavenumber by integrating over the frequency range. The wavenumber is defined as $k=2\pi/\lambda$, where λ is the wavelength. The back azimuth (Θ) and trace velocity are then determined from the wavenumber with the maximum energy by:

$$|k| = \sqrt{(k_x^2 - k_y^2)} = 2\pi f u \qquad (1.11)$$

$$\Theta = \tan^{-1}(\frac{k_x}{k_y}) \qquad (1.12)$$

where f is frequency. The trace velocity can then be deduced from the inverse of the slowness (u) [*Thomas*, 2008]. The FK method has proven effective in both seismic [e.g. *Almendros et al.*, 2002] and acoustic studies [e. g. *Evers and Haak*, 2007].

1.3.2 Signal Detection and Identification Techniques

Numerous techniques can be employed to detect coherent acoustic waves propagating across an array and provide wave parameters. PMCC [*Cansi*, 1995] is a widely used detection algorithm in infrasound array analysis. This method relies on waveform cross-correlation, which applies a time-correction between sensors to obtain the highest degree of similarity. PMCC defines subsets of three sensors (sub-arrays) from within the main array. Time delays between all sensor pairs are then computed from waveform cross-correlation to determine the lag closure relationship:

$$r_{ijk} = \Delta t_{ij} + \Delta t_{jk} + \Delta t_{ki} \qquad (1.13)$$

where Δt_{ij} is the time delay between sensors *i* and *j*. The consistency of the delay times is then computed:

$$c_n = \sqrt{\frac{6}{n(n-1)(n-2)} \sum_{i>j>k} r_{ijk}^2} \qquad (1.14)$$

where *n* is the number of sensors. If the consistency for the sub-array is below a threshold, a "detection" is assigned for the sub-array. Consistency values are then progressively computed for the remaining sub-arrays. As long as the consistency values lie below the threshold, the iterative procedure refines detection parameters. This process is performed over a specified time window and multiple frequency bands and yields the following detection parameters: number of sensors in final sub-network, consistency, trace velocity, and azimuth. Detections are then assigned to "families" based on similar waveform properties [*Cansi and Le Pichon*, 2008].

The Fisher ratio (F-ratio, or F-statistic) [*Melton and Bailey*, 1957] is another common array signal processing detector based on comparison of the variances of both signal and noise. The F-ratio examines whether the arithmetic means of the recordings are consistent with each other. For infrasound array data, FK analysis is first performed to determine the dominant azimuth. The F-ratio is then found by computing the variances within each sensor record and between the array sensors using the following relationship:

$$F = \frac{V_b /(M-1)}{V_w /(M(n-1))} \qquad (1.15)$$

where V_b is the variation between the sensor recordings, V_w is the variation within a single sensor recording, *M* is the number of samples, and *n* is the number of sensors [*Olson and Szuberla*, 2008]. Melton and Bailey [1957] show how the S/N power ratio ($P_{S/N}$) can then be derived from the F-ratio:

$$P_{S/N} = \frac{F-1}{M} \qquad (1.16)$$

The F-ratio can also be estimated in the frequency domain. Time segments with an F-ratio above a threshold are then counted as detections [*Olson and Szuberla*, 2008].

After array processing techniques detect coherent acoustic arrivals, other signal processing techniques are applied. Fourier analysis is often used to examine the frequency content of the signal. For volcanic signals, the frequency spectrum is often indicative of the source process (e.g. harmonic tremor and resonance). Neural networks have also been used to identify volcano infrasound signatures [*Ham et al.*, 1999]. Due to the uncertainties involved in volcano acoustics, other geophysical and geological data are often combined with infrasound. For example, seismoacoustic studies are common and often complementary [e.g. *Garces et al.*, 2000; *Johnson et al.*, 2008b; *Matoza et al.*, 2009b]. Remote sensing has also been shown complementary to infrasound, and may aid in infrasonic detection of volcanic emissions (Chapters 4-5).

1.4. Acoustic Propagation: From Source to Receiver

1.4.1 Atmospheric Structure

Before infrasonic propagation can be discussed, a proper knowledge of the atmospheric structure is necessary. The atmosphere can be divided into five primary layers based upon temperature gradients: troposphere (ground to ~7-17 km height), stratosphere (~7-17 to ~50 km), mesosphere (~50 to ~85 km), thermosphere (~85 to 350–800 km), and exosphere (350-800 to 10,000 km). Figure 1.3 shows the temperature and horizontal winds above Kona, Hawaii on 12 July 2008 0000 UTC. Temperatures generally decrease with increasing height in the troposphere, increase in the stratosphere, decrease in the mesosphere, and then increase again in the thermosphere. Dividing the bottom four layers are the tropopause, stratopause, and mesopause, which are regions of relatively constant temperature [*Drob et al.*, 2003]. For infrasound studies we are only interested in the lowermost ~140 km due to the large amount of attenuation above this height, so the upper thermosphere and exosphere are ignored here.

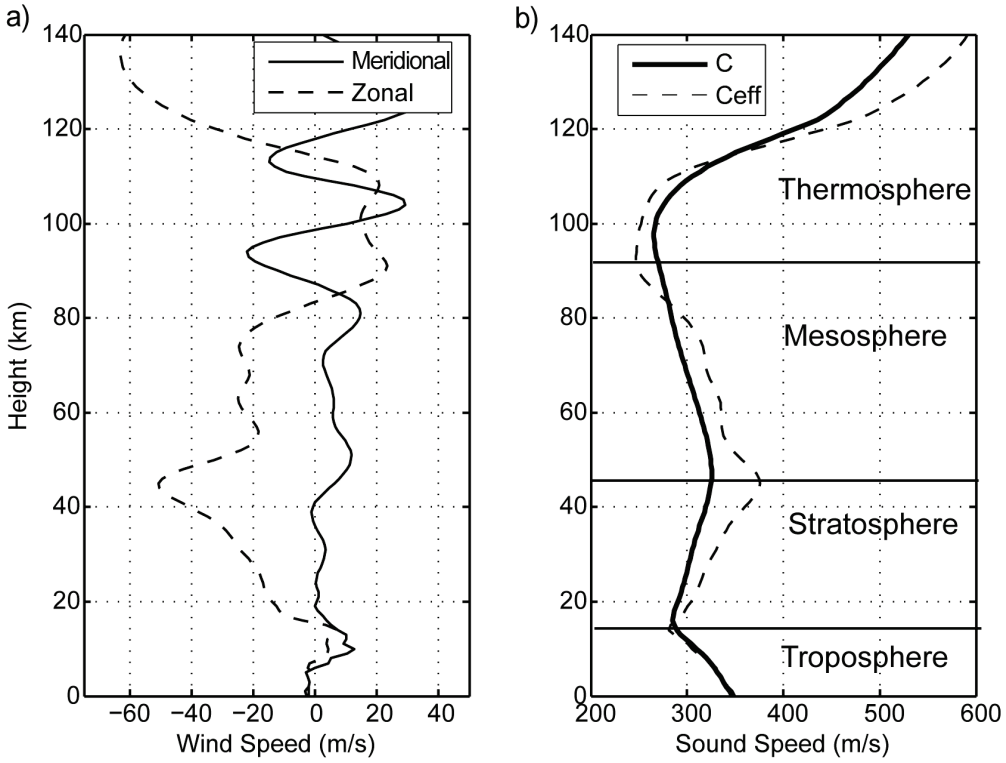

Figure 1.3 NRL-G2S a) wind and b) sound speed profiles above Kona, Hawaii on 12 July 2008 0000 UTC. a) Zonal winds (east-west, positive easterly) are dominated by a westerly jet around 45 km in the stratosphere. Meridional winds (north-south, positive northerly) are relatively light until the thermosphere. b) Sound speed (c, black line) follows a typical profile. Effective sound speed for westerly propagating sound (c_{eff}, dotted black line) shows the effect of the westerly stratospheric wind jet.

Atmospheric winds vary spatially, seasonally, and diurnally. Horizontal winds are divided into zonal (east-west, positive propagating easterly) and meridional (north-south, positive northerly) components [*Brown and Garces*, 2008]. In the troposphere, ducting (waveguide propagation) often occurs in the middle and polar latitudes from the jet stream, as well as small-scale ducts near the surface. Zonal stratospheric wind jets are common at mid-high latitudes and occur predominantly during the solstice periods. These

jets may exceed 100 m/s, causing significant ducting of infrasound [*Drob et al.*, 2003]. It has been postulated that the stratospheric jets are the primary factor in the global detection of infrasonic events [*Le Pichon et al.*, 2009]. Vertical winds have much lower average velocities and are routinely ignored.

Two empirical models were developed to quantify the atmosphere: Mass Spectrometer and Incoherent Scatter Radar (MSISE) and the Horizontal Wind Model (HWM). HWM gives horizontal wind specifications while MSISE provides temperature, density, and pressure. Recently the Naval Research Laboratory Ground to Space (NRL-G2S) semi-empirical model was developed to integrate near-real-time data into the lowermost ~50 km of the atmosphere with the upper atmosphere empirical models [*Drob et al.*, 2003]. The NRL-G2S files thus provide atmospheric specifications necessary for quantifying acoustic propagation every 4-6 hours. The atmospheric profiles in Figure 1.3 use the NRL-G2S files, and the effective sound speed in Figure 1.3b is for westerly propagating sound.

1.4.2 Propagation Theory and Models

Three primary types of models have been used to model the long range propagation of infrasound: geometric, continuous wave, and broadband. Ray theory, a type of geometric model, uses a high frequency approximation and represents propagation paths as rays. This method is useful for identifying propagation paths and estimating travel times. However, it does not account for diffraction and scattering and thus often predicts "shadow zones" where no sound should propagate. In the infrasound community, popular ray theory models are the 3-D Hamiltonian Ray Tracing Program for Acoustic Waves in the Atmosphere (HARPA) modified from [*Jones et al.*, 1986] and Tau-P [*Garces et al.*, 1998a]. Continuous wave models, such as the Parabolic Equation (PE), are used to predict the attenuation for a given vertical slice of the atmosphere. The PE is run at a single frequency and includes diffraction and scattering effects, thus it may help explain the sound propagating into ray theoretical shadow zones. However, the PE is not able to provide travel times and only operates at a single frequency. Broadband models are also able to estimate the attenuation and waveform. The Time Domain Parabolic Equation (TDPE) runs the PE at multiple frequencies and then synthesizes the

output. Broadband models generally require a source waveform and may be computationally expensive [*Whitaker and Norris*, 2008]

The propagation of acoustic waves largely depends on the temperature and winds. Winds in the atmosphere can represent a significant portion of the sound speed (up to 1/2), and thus alter the propagation of acoustic energy. Eq. 1.1 must then be modified to give an effective sound speed:

$$c_{eff} = c + \vec{v} \bullet \vec{n} \qquad (1.17)$$

where v is the horizontal wind vector and n is the ray normal [*Whitaker and Norris*, 2008]. Following Snell's Law, sound waves propagating from the ground will generally be refracted up as the temperature (and thus sound speed) often decreases with height (Fig. 1.3b). However, strong winds and/or temperature gradients may cause the sound speed at altitude to exceed that at the source, causing the sound to refract downwards. In the atmosphere this often occurs in the stratosphere around 50 km and thermosphere around 100 km (Fig. 1.3). Thus the two most common long-range atmospheric returns are stratospheric and thermospheric. Propagation up to ~200 km may consist primarily of direct tropospheric arrivals [*Drob et al.*, 2003], although diffracted tropospheric arrivals may start well before this distance [*Brown and Garces*, 2008].

To illustrate the effect of wind on acoustic propagation, ray tracing is performed for propagation east and west of Kona, Hawaii on 12 July 2008 0000 UTC. Figure 1.4 shows the ray tracing results for the atmospheric profiles displayed in Figure 1.3. The static sound speed (Fig. 1.3b) shows that in the absence of wind, the first ray should be turned in the thermosphere around 115 km height (Fig. 1.4). However, the westerly zonal wind jet around 45 km (Fig. 1.3a) causes c_{eff} for westerly propagating sound in the stratosphere to exceed that at the source (Fig. 1.3b). Thus for westerly propagating sound in these profiles, there is both a stratospheric and thermospheric duct (Fig. 1.4). This is typical for propagation scenarios in mid-high latitudes during the solstice periods.

Due to the inherent limitations of each of the propagation models, combining the results of multiple model outputs is often useful. For example, ray theory may be used to

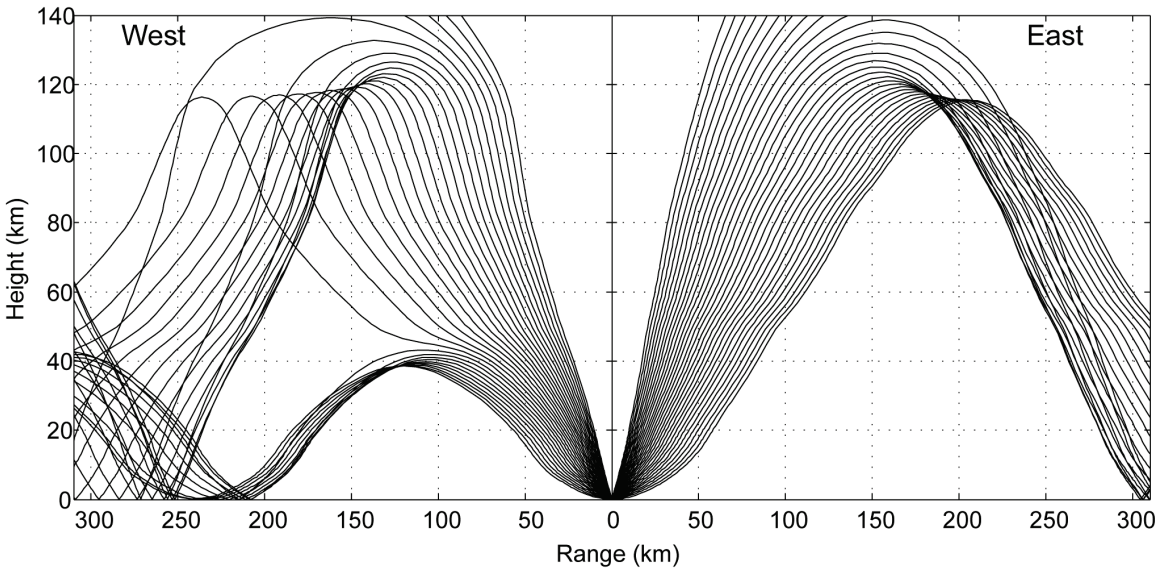

Figure 1.4 Ray tracing for easterly and westerly propagating sound from Kona, Hawaii on 12 July 2008 0000 UTC. The westerly stratospheric jet in Figure 1.3a causes both stratospheric and thermospheric ducting to the west, while only thermospheric ducting is predicted for easterly propagating sound.

estimate the acoustic travel time, azimuth correction, and propagation path, while the PE model then predicts the attenuation. Further, recent work has shown the need to integrate smaller-scale variability into the atmospheric models, such as scattering and gravity wave perturbations [*de Groot-Hedlin et al.*, 2010; *Gibson et al.*, 2008].

1.4.3 Volcano Acoustic Propagation

The high level of sound produced by volcanoes and their known, static location make them prime sources for atmospheric studies. Detailed acoustic studies of volcanoes can lend insight into propagation on multiple scales and validate atmospheric models. In volcanic environments, near source deployments (less than a few km) offer potentially high amplitudes and shorter propagation distances. However, complications from source effects, such as anisotropy (directional dependence), and high noise levels often make

near-source deployments undesirable [*Garces et al.*, in review]. For this reason many infrasound sensors have been placed at regional (a few to tens of km) distances from volcanoes [e.g. *Garces et al.*, 2008; *Matoza et al.*, 2007]. Although this region is often termed the "shadow" or "diffraction" zone due to ray theoretical predictions of no acoustic energy propagating into these regions, numerous studies have shown otherwise. *Fee et al.* [2007] deployed an array ~12 km from an the active infrasonic source at Kīlauea Volcano, Hawaii and found that although the source was constant, recorded amplitudes showed clear diurnal variations. They attributed the variations to enhanced propagation at night due to an enhanced waveguide, commonly seen in theoretical and experimental work [e.g. *Waxler et al.*, 2006]. These types of propagation effects must be considered for regional deployments. Chapters 2-4 focus on regional volcano infrasound recordings.

The importance of providing constraints on hazardous, remote, and/or difficult to monitor volcanoes underscores the utility of telesonic (hundreds to thousands of km range) volcano acoustic signals. Telesonic infrasound recordings of Vulcanian-Plinian eruptions are possible due to the high acoustic energy produced and the low amount of attenuation at the frequencies radiated. However, previous telesonic volcano infrasound studies have primarily used primitive microphones [e.g. *Goerke et al.*, 1965; *Tahira et al.*, 1996; *Wilson et al.*, 1966] or have been used as a means of validating atmospheric models [*Evers and Haak*, 2005; *Le Pichon et al.*, 2005b]. Due to the complex and dynamic nature of acoustic propagation, a clear understanding of long-range acoustic propagation is necessary before source constraints on large eruptions can be made. Chapter 5 explores this idea further.

1.5. Dissertation Overview

1.5.1 Dissertation aims and motivation

Although extensive progress in volcano acoustics has recently been made, numerous questions remain. This dissertation characterizes the infrasound records from Kīlauea Volcano, Hawaii; Tungurahua Volcano, Ecuador; and Kasatochi and Okmok Volcanoes, Alaska. These volcanoes produced a wide variety of acoustic signals, from low-level background tremor detected at 7 km to powerful jet noise recorded thousands

of kilometers away. Here we study the source processes, propagation, and detectable signals from these volcanoes in hopes of providing valuable constraints for hazard mitigation. In particular, the relationship between infrasound and volcanic emissions is investigated by comparing acoustic data with ash plumes imaged by remote sensing imagery. Further, we incorporate relevant seismic, thermal, and visual data to assist with modeling of these processes, particularly the unsteady dynamics of degassing believed to be producing the signals.

1.5.2 Dissertation Organization

Chapter 2 details the infrasound records from the mid-2007 activity of Kīlauea Volcano's East Rift Zone. Dramatic changes in the volcano's activity were all clearly recorded by a single infrasound array, demonstrating the utility of using infrasound in volcano monitoring. Two separate fissures eruptions were located spatially and temporally, and this study marks the first high resolution acoustic records of fissure eruptions. Azimuthal variations from the 21 July 2007 eruption are used to uniquely determine important fissure eruption parameters, such as the fissure propagation rate and individual fissure rupture times. Multiple signals from the collapse of Pu‘u ‘Ō‘ō crater show distinctive characteristics and have possible analogs to other locations. Chapter 2 will soon be submitted to *Geophysical Research Letters*.

Chapter 3 focuses on the 2008-2009 activity at Halema`uma`u Crater, Kīlauea Volcano, Hawaii. An infrasound array 7 km from the crater recorded the vent-clearing degassing burst on 19 March 2008, subsequent infrasonic tremor, and numerous other degassing bursts during the following year. The source for the tremor is interpreted to be a combination of Helmholtz and acoustic resonance of the overlying cavity. Dimensions of the cavity are estimated assuming these types of resonance, and are confirmed with other geophysical observations. Further, comparison of the seismic and acoustic data lends insight into the degassing burst mechanism, upper conduit, and shallow cavity. A copy of this chapter is in peer review as: Fee, D., M. Garces, M. Patrick, B. Chouet, P. Dawson, and D. Swanson (in review), Infrasonic Harmonic Tremor and Degassing Bursts from Halema`uma`u Crater, Kilauea, *Journal of Geophysical Research-Solid Earth*.

Chapter 4 considers acoustic signals from Tungurahua Volcano, Ecuador at arrays of 37 and 251 km distance. Here we chronicle the diverse volcanic activity at Tungurahua between 2006-2008 and characterize Strombolian and Vulcanian explosions, harmonic tremor, and jet noise. Detailed correlation of infrasound data with remote sensing imagery reveals a correlation between ash cloud height and acoustic power for sustained jetting eruptions. Jetting signals from August 2006 represent the first complete high-resolution acoustic recordings of a hazardous Plinian eruption. The shift to lower frequencies during stratospheric ash emission provides a starting point for characterizing the acoustic signature of Plinian eruptions. Further, correlation of the jet noise with thermal imagery indicates multiple turbulence-related sources at Tungurahua. Finally, this chapter outlines the ASHE (Acoustic Surveillance for Hazardous Eruptions) monitoring system and its successful automatic detection and notification of a hazardous February 2008 eruption. A copy of this chapter has been published as: Fee, D., M. Garces, and A. Steffke (2010), Infrasound from Tungurahua Volcano 2006–2008: Strombolian to Plinian eruptive activity, *Journal of Volcanology and Geothermal Research*, *193*, 67-81.

Chapter 5 details the telesonic recordings of the 2008 Plinian eruptions of Kasatochi and Okmok Volcanoes, Alaska. Multiple arrays of the global IMS network clearly recorded these eruptions. For Kasatochi, the spectra for all three main eruption pulses resemble the characteristic jet noise spectra. The jet particle content changes between the eruptive pulses but the spectra remains stable. Although detection of the Okmok eruption is clear at multiple arrays, the lower S/N does not permit detailed source studies. Acoustic energy for both Kasatochi and Okmok is focused within the VLP band, consistent with studies of other eruptions producing stratospheric ash emissions. The multiple pulses of activity at Kasatochi show different propagation characteristics, with the first pulse consistent with thermospheric ducting and the next three with stratospheric ducting. A copy of this chapter is currently in press as: Fee, D., A. Steffke, and M. Garces (in press), Characterization of the 2008 Kasatochi and Okmok eruptions using remote infrasound arrays *Journal of Geophysical Research-Atmospheres*.

Lastly, Chapter 6 synthesizes conclusions from the earlier chapters and postulates further research directions relevant to this body of work.

CHAPTER 2: INFRASOUND FROM THE 2007 FISSURE ERUPTIONS OF KĪLAUEA VOLCANO, HAWAI‘I

Abstract

Varied acoustic signals were recorded at Kīlauea Volcano in mid-2007, coincident with dramatic changes in the volcano's activity. Prior to this time period, Pu‘u ‘Ō‘ō crater produced near-continuous infrasonic tremor and was the primary source of degassing and lava effusion at Kīlauea. Collapse and draining of Pu‘u ‘Ō‘ō crater in mid-June produced impulsive infrasonic signals and fluctuations in infrasonic tremor. Fissure eruptions on 19 June and 21 July were clearly located spatially and temporally using infrasound arrays. The 19 June eruption from a fissure approximately mid-way between Kīlauea's summit and Pu‘u ‘Ō‘ō produced infrasound for ~30 minutes—the only observed geophysical signal associated with the fissure opening. The infrasound signal from the 21 July eruption shows a clear azimuthal progression over time, indicative of fissure propagation over 12.75 hours. The total fissure propagation rate is relatively slow at 164 m/hr, although the fissure system ruptured discontinuously. Individual fissure ruptures times are estimated using the acoustic data combined with visual observations.

2.1. Introduction

During the first half of 2007, the Pu‘u ‘Ō‘ō crater complex (Fig. 2.1) was the primary source of degassing and lava effusion at Kīlauea Volcano, Hawai‘i . In mid-2007, however, dramatic changes occurred at Kīlauea, with an intrusion of magma along the volcano’s upper east rift zone (ERZ) during 17–19 June causing deflation at the summit and draining and collapse of the Pu‘u ‘Ō‘ō magma system. A minor fissure eruption between the summit and Pu‘u ‘Ō‘ō accompanied the intrusion. Activity returned to Pu‘u ‘Ō‘ō on 1 July as lava began to refill the crater. Lava lake growth terminated on 21 July when an eruptive fissure opened on the east rim of Pu’u ’Ō’ō crater and extended east for ~2 km. The fissure eruption accompanied renewed collapse of Pu‘u ‘Ō‘ō crater and resulted in the formation of a new long-lived eruptive vent on the ERZ [*Poland et al.*, 2008].

Previous infrasound studies of Kīlauea Volcano detected a wide variety of eruptive activity. *Garces et al.* [2003] were the first to record infrasound from Kīlauea and detected signals from Pu‘u ‘Ō‘ō and the active lava tube system. *Fee and Garces* [2007] detected diurnal variations in infrasonic tremor amplitude and attributed this to propagation effects related to diurnal atmospheric variability. Recent work by *Matoza et al.* [in review] verified the diurnal variations of *Fee and Garces* [2007], and postulated that oscillations of bubble clouds within the conduit produce the broadband component of infrasonic tremor at Pu‘u ‘Ō‘ō, while the sharply peaked infrasonic tremor spectra may result from low velocity gas jets interacting with solid boundaries. *Fee et al.* [in review] detail infrasonic tremor and transient degassing bursts associated with summit eruptive activity at Kīlauea during 2008–2009. They show how both signal types are explained by degassing exciting the steam-filled cavity into Helmholtz and acoustic resonance. The mid-2007 activity discussed in this manuscript adds fissure eruptions and collapse-related signals to the multitude of infrasound results from Kīlauea. The collapse events presented here show similarities to some of the degassing bursts of *Fee et al.* [in review]. Further, this study documents, for the first time anywhere, infrasonic signals associated with fissure formation and eruptions.

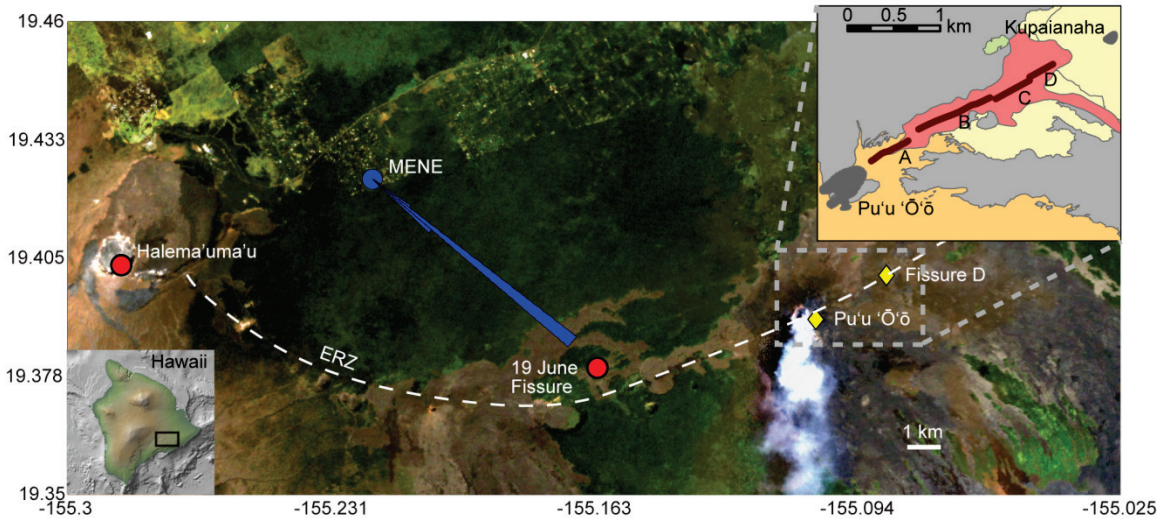

Figure 2.1 Map of the MENE Infrasound Array, mid-2007 Fissure Eruptions Locations, and 19 June 2007 Fissure Detections. The blue circle represents the MENE infrasound array, and the blue beams are the detection azimuths between 19 June 10:15–10:45. The majority of the detections point to 132°, consistent with the 19 June fissure location (red circle). Pu‘u ‘Ō‘ō and Fissure D are indicated by gold diamonds. The inset image shows the locations of the 21 July 2007 fissure system (Fissures A-D).

Our work illustrates the importance of infrasound in volcano monitoring and research. The 19 June fissure eruption was located spatially and temporally using infrasound, but was not detected by any other geophysical monitoring. Detailed constraints on the 21 July fissure eruption, such as timing, location, and propagation rates, were also obtained from infrasound. The wealth of data from Kīlauea during mid-2007 allows us to speculate on the potential source of infrasound from fissure eruptions.

2.2. Data and methods

Data from a four element infrasound array (MENE), located 12.6 km northwest of Pu‘u ‘Ō‘ō crater, is used for this study (Fig. 2.1). The array is the same as that used to study the 2008–2009 eruption at Halema’uma’u Crater [*Fee et al.*, in review] and the April 2007 Pu‘u ‘Ō‘ō crater activity [*Matoza et al.*, in review]. The Chaparral model 2.2 sensors used here have a flat frequency response between ~0.1 and 50 Hz and the array aperture is ~70 m. Data were recorded locally and forwarded in near-real time to the University of Hawai‘i Infrasound Lab. All times listed in the manuscript are in UTC.

Array processing was performed using the Progressive Multi-Channel Correlation (PMCC) technique [*Cansi*, 1995]. Data were processed between 1–7 Hz in 10 frequency bands with 10-second windows and 80% overlap. The 1–7 Hz band was selected due to the predominance of fissure eruption infrasonic signals in this band. In this manuscript, we use the term “detection” to define coherent acoustic energy recorded by PMCC in a single time window and frequency band. Acoustic travel time from the respective source to the station was removed assuming a 0.34 km/s sound speed, typical for the atmospheric conditions present during the study period. Data were beamformed using a time-delay beamforming method [*Johnson and Dudgeon*, 1992] to increase the signal-to-noise ratio (S/N). Waveform filtering was performed using a 4-pole, zero-phase (acausal) Butterworth filter.

Numerous phenomena may affect the accuracy of the infrasound detection azimuth. First, the component of wind perpendicular to the propagation path will deflect the signal and bias the azimuth estimate. During the 21 July eruption, a weather station near Pu‘u ‘Ō‘ō recorded a maximum wind speed of 6.3 m/s, which corresponds to a maximum theoretical deflection from MENE to Fissure A of 1.1°. The wind speed was much less during the main eruption sequence (<4 m/s between 10:00-20:00) so the average deflection is below 0.67° and can be ignored since it is lower than the azimuthal uncertainty. Spatial aliasing, uncertainties in the relative locations of the sensors, and low S/N could also contribute error [*Johnson and Dudgeon*, 1992]. We use PMCC between 1–7 Hz to reduce spatial aliasing, and we performed a total station survey at the array site to decrease the array location errors.

The agreement between the theoretical and observed azimuths of the 19 June and 21 July fissure eruptions (<2°) provides confidence in the azimuth estimates presented here. Similarly, the mean detection azimuth from MENE-Pu‘u ‘Ō‘ō in the three days prior to 17 June is 110.1°, consistent with both *Matoza et al.* [in review] and the expected detection azimuth during winds from the northeast (the typical wind pattern). A fissure eruption is also likely to be a distributed source, since numerous fissure segments could produce infrasound at the same time, so the spread in azimuths may represent multiple sources instead of errors in the azimuth estimation.

2.3. 2007 June 17–19 Intrusion and Eruption

An earthquake swarm on Kīlauea’s upper ERZ near Mauna Ulu and rapid deflation at Kīlauea’s summit began on 17 June at 14:16 (Fig. 2.1), indicating withdrawal of magma from the summit to feed an ERZ intrusion [*Poland et al.*, 2008]. Deflation at Pu‘u ‘Ō‘ō began soon after, accompanied by a series of collapses over the next several days. The first collapse noticeable in a U.S. Geological Survey Hawaiian Volcano Observatory (HVO) Webcam on the north rim of Pu‘u ‘Ō‘ō crater occurred at 19:35, and was accompanied by a minor high frequency (>1 Hz) infrasound signal.

Over the next 57 hours, the earthquake swarm continued and the Pu‘u ‘Ō‘ō crater floor dropped ~80 m. Infrasound signals accompanied collapse events at Pu‘u ‘Ō‘ō crater, including two especially significant events on 18 June. The first event occurs at 09:12:14, lasts for ~18 s, and has an amplitude of 0.094 Pa (Fig. 2.2a,b). The second event begins with a small high frequency signal at 09:16:19 (part 1), followed by increased infrasonic tremor and then a higher amplitude signal at 09:16:32 (part 2), peaking at 0.194 Pa (Fig. 2.2c,d). Part 2 begins with a clear rarefactional (decompressional) onset in the 0.1–1 Hz band, and the polarity has been confirmed by applying both a causal and acausal filter to the data. Infrasonic tremor followed both of these events, with the tremor lasting for >15 minutes after the 09:16 event. Both events were recorded by the Webcam as bright flashes from a vent within Pu’u O’o crater. On 19 June, the intrusion breached the surface in two short fissures with a total span of 165 m, located 6 km west of Pu‘u ‘Ō‘ō along the northeast flank of the Kane Nui o Hamo shield (Fig. 2.1), ~132° from MENE. A clear infrasonic signal, focused between 2–10

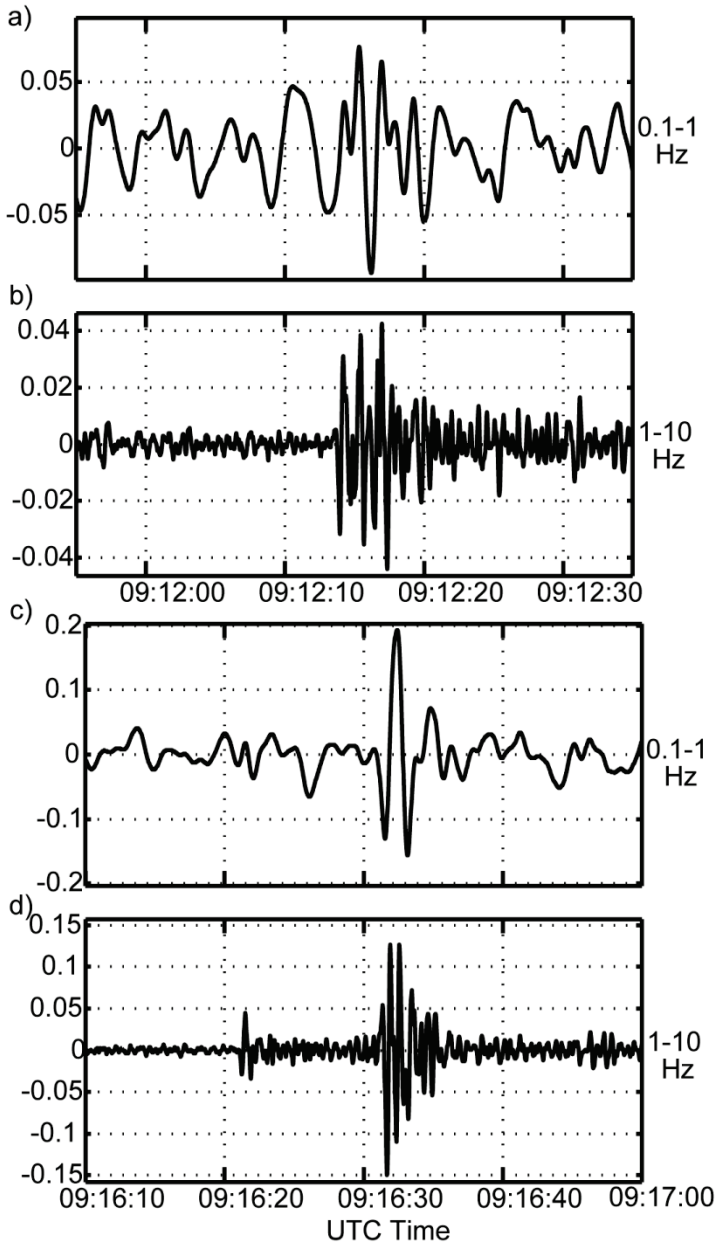

Figure 2.2 18 June 2007 Puʻu ʻŌʻō Collapse Events. The first event occurs at ~09:12 and is divided into two bands a) 0.1–1 Hz and b) 1–10 Hz. This event begins with a sharp onset at 09:12:14 and last for ~18 s. The larger second event at 09:16 is also split into the c) 0.1–1 Hz and d) 1–10 Hz band and begins with a small 1–10 Hz onset at 09:16:19, followed by elevated infrasonic tremor and a large rarefactional onset in the 0.1–1 Hz band at 09:16:32. The rarefactional onset in d) has been confirmed using both a causal and acausal filter. Both events are followed by increased infrasonic tremor. Acoustic travel time from the source to receiver has been removed.

Hz, was recorded between 10:15–10:45 from 132–133° (Fig. 2.1), the same azimuth as the Kane Nui o Hamo fissure. No other significant infrasound was detected during the presumed fissure opening time period. No visual, seismic, deformation, or other geophysical evidence of the eruption onset was recorded. HVO field crews visiting the eruption site at ~17:00 estimated that lava had breached the surface at the fissure a few hours before, consistent with the acoustically derived onset. After the fissure opening, no infrasound from Kīlauea was detected by the MENE array until 1 July, when lava returned to Puʻu ʻŌʻō, establishing a direct connection between magma and the atmosphere.

2.4. 21 July 2007 Fissure Eruption

Puʻu ʻŌʻō crater slowly filled with lava during 1-21 July, accompanied by minor infrasonic tremor. At about 09:00 on 21 July, tilt measurements from an instrument on the north flank of Puʻu ʻŌʻō indicated rapid tilt to the east. HVO Webcam imagery revealed crater floor subsidence and rapid draining of the lava lake starting at approximately 09:55. The Webcam recorded glow to the east at 10:39, indicating that an eruption, out of sight of the Webcam, was in progress. Field observations starting at about 17:40 documented lava erupting along a series of four fissure segments (designated A–D) extending from just below the east rim of Puʻu ʻŌʻō crater for ~2 km to the east (Fig. 2.1.) [*Poland et al.*, 2008].

Although no significant seismicity was noted during the formation of the 21 July fissure [*Poland et al.*, 2008], strong infrasound signals were recorded. Figure 2.3 shows the a) 1–7 Hz beamed waveforms, b) spectrogram, and c) number of detections per 5 minutes between 95–110°. The up-rift end of the 21 July fissure system (westernmost point of Fissure A) is 107.7° and 12.7 km from MENE, while the down-rift end (Fissure D) is 102.0° and 14.1 km (Fig. 2.1). The acoustic onset of the eruption consists of a minor detection at 10:06 from ~108°. An emergent and higher-amplitude signal follows at 10:13 and continues for more than 6 hours (Fig. 2.3a, b). The majority of the PMCC detections occur between 10:06–11:30, coincident with peak infrasonic amplitudes between 1–7 Hz (Fig. 2.3b,c).

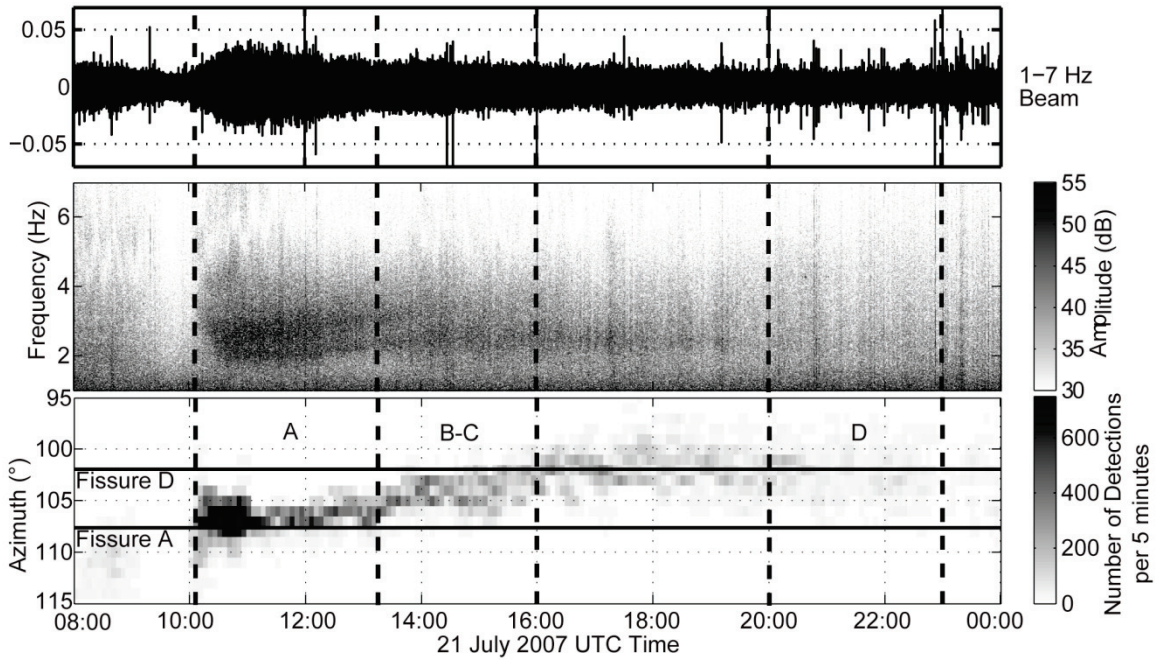

Figure 2.3 21 July 2007 Fissure Eruption a) 1–7 Hz beamformed waveforms, b) spectrogram, and c) PMCC detections between 08:00-24:00 UTC. Solid lines in c) represent the approximate azimuth from the array to Fissures A and D, the start and end points of the fissure eruption. The dashed vertical black line at 10:06 represents the acoustic onset of the fissure eruption. A clear progression in the signal azimuth in c) represents the rupture of new fissure segments and the subsequent dotted black lines indicate approximate fissure rupture intervals inferred from the azimuthal progression and visual observations (see text for more details). The maximum number of detections between 10:15–11:00 correlates well with the peak acoustic a) and spectral amplitudes b) and Fissure A (Fig. 1), suggesting this is where and when the most vigorous degassing occurred. Spectrogram units are in dB relative to $(20\times10^{-6}$ Pa$)^2$/Hz.

The infrasonic signal shows a clear change in azimuth as the fissure propagated downrift (Fig. 2.3c). The detection azimuths begin at ~108° at 10:06, and the majority of detections lie between 106–108° until 13:15 (Fig. 2.3c). These azimuths correlate well with the azimuths to Fissure A (Fig. 2.1, 106.3°–107.7°); thus, the higher amplitude infrasound and detections during this period suggest that the most vigorous degassing from the 21 July 2007 eruption occurred from Fissure A between ~10:06 and 13:15 (Fig. 2.3). The detection azimuths begin to migrate at about 13:15, suggesting that new fissure segments were opening. During 13:15–16:00, the detections indicate a steady azimuthal progression to ~102° (Fig. 2.3c), possibly corresponding to the rupture of Fissures B (104.1°-105.6°) and C (102.3°-103.4°) (Fig. 2.1). The gradual nature of the azimuth progression and the limited azimuthal resolution do not allow for differentiation between the rupture of Fissures B and C. Detection azimuths stabilize after 16:00, suggesting that the majority of fissure propagation had ceased (Fig. 2.3c). A helicopter overflight around 17:40 confirmed that Fissures A-C had all ruptured and that Fissure C hosted a 6-8 m lava fountain. Field crews arrived at the site by 20:00 and observed Fissure D opening in sections between 20:00 and 23:00. Infrasound data cannot distinguish this activity, since the total length of Fissure D is small and not resolvable in azimuth (101.8-102.0°). Further, the azimuth to Fissure D is difficult to differentiate from Fissure C.

Infrasound related to fissure activity gradually died out around 22 July 00:00 (Fig. 2.3), indicating the end of vigorous degassing and fountaining, consistent with visual observations. The decrease in acoustic signals is not due to diurnal propagation effects, like those documented by *Fee and Garces* [2007]. The detections die out around 00:00 (14:00 local time), well after the nocturnal tropospheric ducting would have ended. The vigorous portion of the 21 July 2007 fissure eruption is therefore assumed to have lasted for 13.9 hours (10:06–00:00).

We estimate fissure propagation characteristics using the acoustic and visual observations. The entire fissure system took 12.75 hours (10:06-23:00) to rupture a distance of 2.12 km, for an average propagation rate of 164 m/hr. The observed starting and ending infrasound azimuths (Fig. 2.3c, 108° and 102°) are consistent with the azimuths of the entire fissure system (Fig. 2.1, 107.7°–101.8°); however, the system appears to have ruptured discontinuously. Fissures A-C took ~5.9 hours (10:06-16:00) to

rupture 1.81 km, giving a propagation rate of 307 m/hr. Fissure A erupted first at 10:06 and continued as the primary source of degassing until ~13:15 UTC. Fissures B-C then ruptured 1.24 km over 3.75 hrs for a rate of 331 m/hr. The rupture then paused for up to 4 hours, upon which Fissure D ruptured at a much slower rate of ~69 m/hr (based on visual observations).

The 21 July fissure propagation rates are slower than those reported for other eruptive fissures. At Kīlauea, *Duffield et al.* [1982] estimated the propagation of the September 1971 fissure at 600 m/hr based on migration of lava fountains. Okamura et al. [1988] used both tilt and seismic data to determine a dike propagation rate of 550-700 m/hr during the onset of the 1983 Pu‘u ‘Ō‘ō eruption. The 1984 Mauna Loa eruption had a large fissure system that ruptured at a rate of 1200 m/hr [*Lockwood et al.*, 1987]. A fissure eruption on Kīlauea's ERZ in 1991, in nearly the same location as the 21 July fissure, ruptured at ~1000 m/hr [*Mangan et al.*, 1995]. The relatively low fissure propagation rate and weak eruptive vigor of the 21 July eruption may be indicative of a relatively low-energy eruption, perhaps because the erupting lava had already degassed. Much of the erupted lava was probably derived from the pre-21 July Pu‘u ‘Ō‘ō lava lake, as suggested by lava lake draining associated with fissure opening and low gas emissions measured prior to the 21 July eruption [*Poland et al.*, 2008].

Within three weeks of the 21 July fissure opening, effusion focused on a single portion of Fissure D, which developed into a new long-term eruptive vent (still active as of June 2010). Pu‘u ‘Ō‘ō crater continued to act as the primary source of degassing, despite the lack of eruptive activity. Infrasonic tremor from Pu‘u ‘Ō‘ō resumed on 25 July, and the crater has remained the dominant acoustic source in this region, although occasional tremor bursts were detected from Fissure D over the remainder of 2007.

2.5. Acoustic Source

The 18 June collapse signals from Pu‘u ‘Ō‘ō represent the first two impulsive, transient infrasound events recorded at Kīlauea. Previous studies have reported only emergent, long duration tremor signals from Pu‘u ‘Ō‘ō and its associated lava tube system [*Fee and Garces*, 2007; *Garces et al.*, 2003; *Matoza et al.*, in review]. The 18 June events are probably related to gas release that resulted from disruption of the ponded

lava surface that existed within a vent within Pu‘u ‘Ō‘ō crater prior to its collapse. Bright flashes observed in HVO Webcam imagery, coincident with the infrasound signals, support this hypothesis, and the process is similar to that associated with some degassing bursts during 2008–2009 summit eruptive activity at Kīlauea [*Orr et al.*, 2008]. The rarefactional onset of part 2 of the 18 June 09:16 event (Fig. 2.2c,d) may be explained by downward motion of collapsing material. The infrasonic tremor which followed that event was likely related to degassing of the disturbed lava surface.

We also detail the first infrasound data clearly associated with a fissure eruption at Kilauea (*Liszka and Garces* [2002] recorded long-range infrasound from the 2000 fissure eruption of Hekla Volcano, Iceland). Although the 19 June fissure is clearly detected in the infrasound, the signal-to-noise ratio is too low to determine a source process. The 21 July 2007 fissure eruption, in contrast, had a much clearer signal and visual observations confirmed small-scale lava fountains (<8 m in height) that extended over numerous fissure segments. Low-level gas jetting from these fountains may be producing a form of jet noise. Recent studies have focused on jet noise from large, high velocity jets from Vulcanian to Plinian eruptions [*Fee et al.*, 2010; *Matoza et al.*, 2009]. The infrasonic source of these eruptions has been postulated to be related to large-scale turbulent eddies along the edge of the flow, primarily from the characteristic frequency spectrum. The 21 July fissure eruption produced relatively low velocity, small scale jetting. The acoustic spectrum here is relatively broadband and detections continued for ~14 hours (Fig. 2.3b), but at much lower amplitude, higher frequency, and with a sharper roll-off than Vulcanian-Plinian jet noise. Thus the acoustic source here may be a form of jet noise, but because this is a basaltic system the jetting is characterized by fountains with large clasts [*Sparks et al.*, 1997] and may produce different acoustics. The interactions of turbulent structures with the large clasts [*Woulff and McGetchin*, 1975] may play a dominant role in producing sound during fissure eruptions and fountaining.

2.6. Conclusions

Results from Kīlauea reiterate the utility of infrasound at volcanoes for monitoring and research. A series of dramatic changes at Kīlauea in mid-2007 produced infrasonic signals associated with the collapse of Pu‘u ‘Ō‘ō crater and two fissure

eruptions. The collapse and subsidence of Pu‘u ‘Ō‘ō crater on 17-19 June produced multiple infrasonic signals. Two events had impulsive onsets—the first such signals recorded at Kīlauea. An event on 18 June 09:16 had a rarefactional onset between 0.1–1 Hz, indicative of a rare decompressional source. The collapse of the crater floor may have created this rarefaction and then disrupted the lava surface and released a large amount of accumulated gas, similar to some of the 2008-2009 activity at Halema’uma’u Crater. For the 19 June fissure eruption, infrasound constrains the timing when no other evidence of the onset of fissure opening exists. Infrasound recordings from the 21 July eruption resulted in insight into the timing, fissure propagation rate, and time period of principal degassing. Future research employing infrasound will lead to better understanding of eruptive processes, while also providing an additional tool for monitoring volcanic activity.

Acknowledgements

A version of this chapter will soon be submitted to *Geophysical Research Letters*. The authors wish to thank HVO for their continued support, particularly Frank Trusdell for hosting the array. Field work assistance was provided by James Robertson. Funding support was provided by NSF Grant EAR-0609669.

CHAPTER 3. INFRASONIC HARMONIC TREMOR AND DEGASSING BURSTS FROM HALEMA`UMA`U CRATER, KĪLAUEA VOLCANO, HAWAII

Abstract

The formation, evolution, collapse, and subsequent resurrection of a vent within Halema`uma`u Crater, Kilauea Volcano produced energetic and varied degassing signals recorded by a nearby infrasound array between 2008 to early 2009. After 25 years of quiescence, a vent-clearing explosive burst on 19 March 2008 produced a clear, complex acoustic signal. Near-continuous harmonic infrasonic tremor followed this burst until 4 December 2008, when a period of decreased degassing occurred. The tremor spectra suggest volume oscillation and reverberation of a shallow gas-filled cavity beneath the vent. The dominant tremor peak can be sustained through Helmholtz oscillations of the cavity, while the secondary tremor peak and overtones are interpreted assuming acoustic resonance. The dominant tremor frequency matches the oscillation frequency of the gas emanating from the vent observed by video. Tremor spectra and power are also correlated with cavity geometry and dynamics, with the cavity depth estimated at ~219 m and volume ~3×10^6 m^3 in November 2008. Over 21 varied degassing bursts were observed with extended burst durations and frequency content consistent with a transient release of gas exciting the cavity into resonance. Correlation of infrasound with seismicity suggests an open system connecting the atmosphere to the seismic excitation process at depth. Numerous degassing bursts produced VLP (0.03-0.1 Hz) infrasound, the first recorded at Kilauea, indicative of long duration atmospheric accelerations. Kilauea infrasound appears controlled by the exsolution of gas from the magma, and the interaction of this gas with the conduits and cavities confining it.

3.1. Introduction

Eruptive activity returned to Kilauea Caldera in early 2008 after over 25 years of inactivity. Gas emissions within Halema`uma`u crater increased substantially in late 2007 and early 2008 and were punctuated by a vent-clearing explosive burst on 19 March 2008 [*Wilson et al.*, 2008]. This burst damaged the nearby scenic overlook and opened a 35 m wide vent. Near-continuous degassing and tremor from a shallow source immediately followed the explosive burst and continues at the time of writing (with some interruptions) [*Patrick et al.*, in review]. Numerous other long-duration degassing bursts occurred at the vent during this period as well, erupting both lithic and juvenile material [*Houghton et al.*, 2008].

The release of pressurized gas at volcanoes perturbs the atmosphere and creates infrasound, or pressure oscillations with frequencies below 20 Hz, that are able to propagate long distances with little attenuation. Early work at Kilauea suggested Hawaiian eruptions, with the exception of the large phreatic explosions of 1924, were acoustically quiet, primarily producing white noise [*Richards*, 1963]. However, recent studies have shown that even effusive activity at Kilauea produces considerable infrasound. *Garces et al.* [2003] were the first to detect infrasound from allegedly steady, quiescent activity at Kilauea, suggesting that flow-induced sound may be prevalent during open-vent Hawaiian eruptions. Analysis of their infrasound data, recorded ~2 km from the Pu`u `O`o crater complex, revealed substantial energy emanating from Pu`u `O`o, the primary source of degassing, and along the lava tube system. *Fee and Garces* [2007] recorded diurnal variations in the Pu`u `O`o infrasonic tremor amplitude recorded at a range of 13 km, and explained the variations as being caused by atmospheric propagation effects due to diurnal ground cooling and warming. In later work, *Matoza et al.* [in review] deployed an array ~2.5 km from Pu`u `O`o and verified the propagation effects of *Fee and Garces* [2007], identified the acoustic excitation of a lava skylight, and postulated a flow-induced acoustic source model for the Pu`u `O`o infrasonic tremor. Since this time, recordings from Pu`u `O`o and recent fissure eruptions show that near-constant infrasound emanated from multiple sources and correlates well with the primary degassing sources at Kilauea [*Fee et al.*, 2007]. This research demonstrates that explosive volcanism is not necessary to produce substantial low frequency sound with energies on

the order of kW. Due to the relative stability of the source processes and the wealth of knowledge and resources at the Hawaiian Volcano Observatory (HVO), the ongoing effusive eruption at Kilauea has permitted comprehensive research on the acoustics of low-intensity magma-gas interactions, and the possible extension of this knowledge to more explosive eruptive regimes.

Although Kilauea is considered to be a somewhat benign volcano, it still poses a hazard to the numerous visitors, residents, scientists, and aircraft in the vicinity. The recent activity at Halema`uma`u has produced numerous potentially dangerous degassing bursts and a significant amounts of noxious gas (such as SO_2). The use of infrasound for hazard mitigation has seen recent progress, as arrays at Mount. St. Helens [*Matoza et al.*, 2007] and Ecuador [*Fee et al.*, 2010; *Garces et al.*, 2008] have identified energetic eruptions at silicic volcanoes and set up an automatic system notifying civil defense authorities of acoustic signals associated with substantial volcanic ash emissions. Infrasonic monitoring of Stromboli volcano [e.g. *Ripepe et al.*, 2009] has also shown recent progress in hazard mitigation.

Analysis of Kilauea infrasound provides insight into the timing, dynamics, and source of degassing, as well as the propagation path of the acoustic waves. The impressive diversity and energetics of infrasound from Halema`uma`u suggest degassing at Kilauea is an inherently unsteady process with the shallow degassing and resonating source well-connected to the atmosphere. An infrasound station ~7 km from Halema`uma`u recorded high signal-to-noise ratio pressure oscillations from both the degassing bursts and tremor. The continuous record of infrasonic activity reported here between March 2008-February 2009 outlines the formation, evolution, collapse, and subsequent reactivation of the vent at Halema`uma`u (Section 3.4). The source of the infrasound from Halema`uma`u is attributed to unsteady degassing of magma into a gas-filled volume that is excited into resonance. Consequently the infrasound recorded from Halema`uma`u provides insight into its degassing history, while the approximate size and spatial characteristics of the gas-filled cavity below the vent can be inferred from the peaks in the infrasonic tremor spectra using the eigenfrequency analysis (Section 3.5). Correlation of the infrasound with visual, audible, and seismic data provides further insight into the dynamics of the volcano (Section 3.6).

In addition to the harmonic tremor and 19 March 2008 explosive burst recorded at Kilauea, numerous other transient degassing events have been detected. Explosions are defined as transient signals with a rapid rise to a positive peak sound pressure and followed by a negative pressure excursion (rarefaction). Although often containing an explosive component, the Halema'uma'u events exhibit a wide variety of features, including relatively long durations and often emergent or rarefactional onsets. Further, the frequency content of the bursts is similar to that of the tremor (Section 3.4.4). Thus we follow the terminology of *Chouet et al.* [in review], and use the more general term degassing burst rather than explosion. Further, we follow volcano seismology nomenclature [*Chouet*, 1996] to facilitate comparisons and classify degassing burst features in three separate bands based on their period: Very Long Period (VLP) signals between ~10-33 s (0.3-.1 Hz), Long Period (LP) between ~1-10 s (0.1-1 Hz), and Short Period (SP) ~0.1-1 s (1-10 Hz). Nearly all of the degassing bursts at Halema`uma`u have infrasound focused in the LP band, while only a few have VLP components. Volcano infrasound signals in the VLP band (IVLP) are infrequently reported and require an energetic source that slowly accelerates a large volume of the atmosphere. IVLPs are associated with rock falls [*Moran et al.*, 2008], Plinian jetting [*Matoza et al.*, 2008], and very large explosions [*Mikumo and Bolt*, 1985]. The scarcity of these types of signals can likely be attributed to limitations in recording technology and processing methodology. Recent progress in sensor and detection capabilities has increased the identification of these events. Potential source models for the degassing bursts are presented in Section 3.7.

3.2. Kilauea Volcano

The Kilauea summit region encompasses Kilauea caldera, including Halema`uma`u Crater, and some nearby volcanic features (Fig. 3.1). The last major explosive activity at the summit was in 1924, when vigorous phreatic explosions at Halema`uma`u resulted from the lowering lava lake's interaction with the water table [*Stearns*, 1925]. Since 1924, activity at the summit has been sporadic and short-lived compared to the more active and sustained effusive eruptions along the East Rift Zone (ERZ). The last sustained Halema'uma'u eruption was in 1968 [*Holcomb*, 1987]. Activity

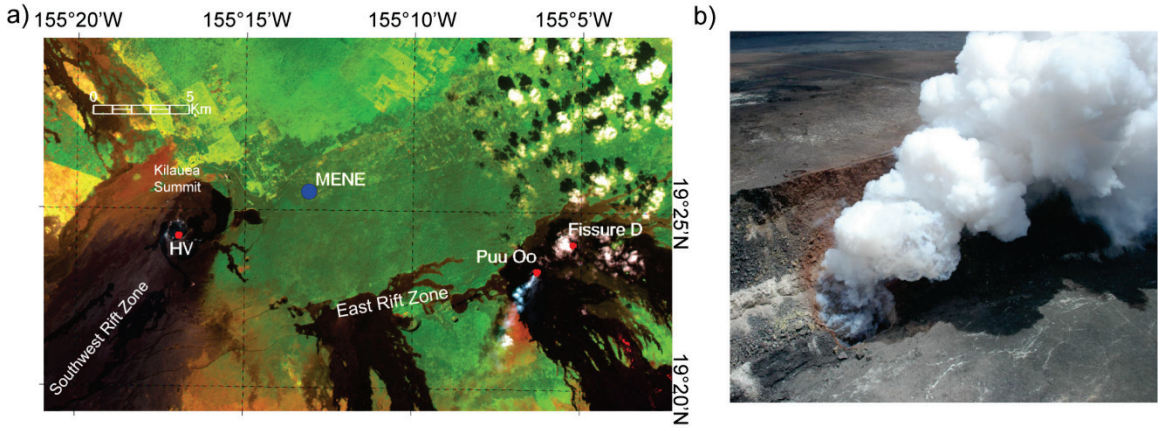

Figure 3.1 Overview map of study area a) and photo of the Halema`uma`u Vent b). a) The blue dot denotes the MENE infrasound array, located ~7 km NE of Halema`uma`u. Pu`u `O`o and Fissure D, the other two primary sources of infrasound, are labeled as red dots. b) Photo of Halema`uma`u taken on 1 August 2008 when the vent was ~50 m in diameter. Photo courtesy of USGS

at the summit between 1983 and 2003 was characterized by magma storage and deflation. After ~4 years of inflation beginning in 2003, rapid deflation at the summit in June 2007 coincided with an intrusion and eruption along the ERZ [*Poland et al.*, 2009].

In November 2007 seismic tremor levels began to rise at the summit, reaching 5 times background levels by early March 2008. The increased seismic tremor was coincident with activity of a ~30-m wide fumarolic region visible within Halema`uma`u crater. This fumarolic activity was responsible for substantially increased SO_2 emissions [*Wilson et al.*, 2008]. On 19 March 2008 at 12:59 UTC, a degassing burst within Halema`uma`u crater was associated with the opening of a ~35 m wide vent where the fumarolic region previously existed, hereafter referred to as the Halema`uma`u vent (HV). Because no juvenile material was found after the burst [*Houghton et al.*, 2008] it is presumed to be either gas-driven or occur at a depth where the lava did not reach the free surface due to geometrical constrictions or its depth within the cavity. The volume of ejecta from the degassing burst is much less than the presumed cavity size, providing

evidence that a gas-filled cavity existed below the vent prior to the explosive burst. It is likely that the hot, magmatic source at depth slowly eroded the rocks above it, creating a void space and an unstable overhanging roof [*Swanson et al.*, 2009].

3.3. Data Acquisition and Processing

3.3.1 Data Acquisition

The infrasound station used in this study consists of a 4-element, ~70 m aperture array, and is termed MENE. This array is similar to that of *Fee and Garces* [2007], as the site was reoccupied in late 2006 and recording continues at the time of writing (Fig. 3.1a). Four Chaparral Physics 2.2 microphones are deployed in a centered triangle configuration 6.81 km from HV and 12.65 km from Pu`u `O`o. The azimuth from the array to HV is ~250° and 109° to Pu`u `O`o, providing a clear difference in azimuth and thus reducing ambiguity between the two primary source locations. The microphones have a flat frequency response from 0.1-200 Hz, and the instrument response has been removed. Most of the infrasound recorded at Kilauea (and other volcanoes) is concentrated between 0.1 and 10 Hz. Data was sampled at 40 Hz and digitized using a 6-channel, 24-bit Reftek 130-01 DAS. After being written to disk locally the data is then sent over the internet to the University of Hawaii Infrasound Lab, where it is archived and processed in near real-time. Dense jungle surrounding the array provides an ideal array setting, as the thick vegetation reduces the effect of wind on the sensors. All times listed in this manuscript are in UTC.

A Sony HDR-HC3 high definition digital video recorder was used to record the vent oscillations. For the degassing bursts, video was taken from an autonomous standard-definition camera in place at HVO recording at 8 frames per second. The video was time stamped using a local computer and routinely time synced using network time protocol.

3.3.2 Array Processing

The Progressive Multi-Channel Correlation method (PMCC) [*Cansi*, 1995] is used to determine the velocity and azimuth of the coherent infrasonic arrivals at the array. This method is effective at distinguishing acoustic sources of interest from unwanted

signals, termed clutter. Two separate processing runs were employed. The first is between 0.5 and 10 Hz with 20 frequency bands. This run concentrates on the higher frequency acoustic arrivals. After the opening of the HV, lower frequency band-limited signals were discovered and a second run was performed between 0.3 and 1 Hz with 10 frequency bands. Both runs used window lengths of 30 seconds with 83% overlap. The PMCC results were also checked with frequency-wavenumber (F-K) array processing methods.

To increase the signal-to-noise ratio much of the data presented in this study were beamformed using time-delay beamforming [*DeFatta et al.*, 1998; *Matoza et al.*, 2007]. This technique removes the travel time differences between the sensors in the array from an assumed acoustic plane wave arriving from a specified azimuth and then stacks the traces, effectively increasing the signal from the specified azimuth. Assuming a typical temperature of ~20°C, the sound speed in the vicinity of HV during the experiment is roughly 0.34 km/s. Thus it would take an acoustic wave ~19.85 s to travel from HV to MENE.

3.3.3 Signal Processing

Various spectral analysis methods are utilized to examine the frequency content of the infrasound records. A probability density function of the power spectral density [*McNamara and Buland*, 2004] was constructed to investigate the stability of the resonance peaks. Thirty-minute segments from 48 hours of data were first beamformed assuming an acoustic wave arriving from 250° at 0.34 km/s. A power spectral density (PSD) estimate was calculated for each segment using 3000 sample (75 s) windows with 75% overlap. The probability that the power level will be at a particular value was then calculated for each frequency/power bin between 0.05-10 Hz and 15-100 dB relative to $(20\times10^{-6}\ \text{Pa})^2/\text{Hz}$. This method has previously been used to study site background noise levels [*McNamara and Buland*, 2004], and provides a statistical means of assessing the signal levels and stability of the individual spectra. Power spectra for the degassing bursts were calculated using a multi-taper method [*Riedel and Sidorenko*, 1995]. This method was used due to the relatively short durations. If not otherwise noted, Welch's modified

periodogram method is used to calculate power spectra. Filtering is performed using a 2-pole, zero-phase Butterworth filter.

3.3.4 Acoustic energy calculation

To calculate how energetic the degassing bursts and tremor are at HV, the acoustic energy is calculated for the entire study period. For a compact acoustic source radiating into a half space from the surface, the acoustic energy (in J) produced at the source may be estimated from [*Pierce*, 1981]:

$$E_a = \frac{2\pi r^2}{\rho c} \int_0^T \Delta p^2(t) dt \qquad (3.1)$$

where r is the source-receiver distance, ρ the air density, c the atmospheric sound speed (~340 m/s in this study), and Δp the acoustic fluctuation from ambient pressure as a function of time, t, which is integrated over the signal duration T. For HV, this is the energy at the vent, not the actual source of degassing.

Use of Eq. (3.1) allows comparison of the relative acoustic energies between transient signals (bursts). It also permits quantitative comparison of acoustic energies between volcanoes [*Johnson*, 2003; *Marchetti et al.*, 2009; *Vergniolle et al.*, 1996] in overlapping frequency bands. For sustained sources (tremor), it is more useful to use acoustic power estimated by dividing the energy by the time interval. In this study we use 1-hour-long segments. Our approach follows that of *Fee et al. [2010]* and only considers the energy during periods during which a coherent acoustic signal propagating from the direction of Halema`uma`u is detected at the array by the PMCC algorithm and has a correlation value above 0.5. For the tremor and degassing bursts, acoustic energy was calculated over the 0.1-10 Hz band.

3.4. Observations

3.4.1 Visual Observations

During the study period HV had an overhanging rim above a dominantly fume-filled cavity (Fig. 3.1b). The size of the vent was measured daily by visual observations compiled by HVO. The vent increased in diameter from ~35 m on 19 March 2008 to

~110 m in February 2009. Major rockfalls associated with the degassing bursts and collapse events increased the vent diameter abruptly [*Orr et al.*, 2008]. FLIR (Forward looking infrared) imagery in late 2008/early 2009 revealed a narrow conduit with a diameter of ~10 m at the bottom of a ~200 m deep cavity. The horizontal shape and dimensions of the cavity are not well constrained due to heavy fume. LIDAR measurements taken in June 2009 by the University of Hawaii and HVO provided a glimpse of the cavity shape and dimensions (T. Ericksen, personal communication). The depth of the cavity was found to be ~207 m, with a roughly elliptical ~120×190 m cross section at the top. The lateral dimensions appeared greatest in the center of the cavity.

On 20 March 2008, scientists at the HVO noticed a conspicuous oscillation of the gas exhalation at HV. Rather than a sustained rising plume, the lowermost portion of the plume would begin to rise above the vent and then be drawn or "sucked" back down into the vent. After being drawn in, the plume would rise again, beginning the cycle once more. These "breathing" oscillations were visible for long periods of time, and were restricted to portions of the plume within the first 10-20 m above HV. Numerous audible observations made near the vent correlate the breathing oscillations with gas rushing sounds.

To better constrain the oscillations, a video camera was set up at the HVO Halema`uma`u lookout. A 9 s video of the oscillations from March 20th is included as Supplementary Video 3.1. Ten measurements of the oscillation period and plume velocities were made from the video. The period of the oscillations ranged between 1.77 and 2.93 s (0.57-0.34 Hz), with an average of 2.13 s (0.47 Hz). Near the vent, plume velocities range between 5.8 and 16.6 m/s, with an average of 9.5 m/s. These velocities are typical of buoyant plumes at basaltic volcanoes [*Patrick et al.*, 2007], and despite the oscillations, suggest there is no gas-thrust phase at the vent surface and thus low gas overpressure.

3.4.2 19 March 2008 Degassing Burst

Infrasound activity preceding the 19 March degassing burst consists of low level, background tremor originating from the direction of Pu`u `O`o (~109°) (Fig. 3.1a). Figure 3.2 shows the 0.1-10 Hz beamformed waveform and spectrogram for the burst,

with travel time reduced to an origin time assuming that the source is at the vent. The acoustic onset of the degassing is at 12:59:00 (Fig. 3.2a). This onset is broadband with energy extending above 5 Hz (Fig. 3.2b). No precursory infrasonic anomalies were detected. The signal has a peak amplitude of ~0.94 Pa and duration of ~53 seconds. This infrasound-derived burst duration is considerably longer than most of those reported in volcano acoustic studies [*Harris and Ripepe*, 2007; *Johnson*, 2007; *Jones et al.*, 2008; *Petersen et al.*, 2006]. Assuming spherical spreading, the peak pressure amplitude one meter from the vent is 6.5 kPa and the estimated acoustic energy for the degassing burst is 8.48×10^5 J. Most of the acoustic energy after the initial broadband onset is within the LP band (Fig. 3.2b).

3.4.3 Harmonic Infrasonic Tremor

Sustained harmonic infrasonic tremor ensued immediately after the vent-clearing degassing burst of 19 March (Fig. 3.2c,d) and continued nearly unabated for 9 months until 4 December 2008. The average peak-to-peak tremor amplitude is 0.8 Pa at the array, similar to that of the peak for the 19 March degassing burst, and well above the background noise of ~0.1 Pa. The average acoustic power of the background tremor is 7×10^3 W, comparable to ambient tremor level at Tungurahua Volcano [*Fee et al.*, 2010] and over twice as energetic as that of Pu`u `O`o (~2.5×10^3 W) [*Fee et al.*, 2007]. Visual observations and gas measurements by HVO confirm sustained degassing coincided with the infrasonic tremor [*Patrick et al.*, in review; *Wilson et al.*, 2008], as well as continuous audible "gas-rushing" sounds at the vent.

The frequency content of the tremor during the experiment features two principal peaks. The dominant peak, f_1, resides between 0.3-0.6 Hz. A subdominant peak, f_2 is also observed in the band 1-3 Hz. At times during the experiment this secondary peak was not distinguishable as it was accompanied by spectral peaks of similar power at similar frequencies. Figure 3.3 is a probability density function (PDF) of 30-min beamformed PSD estimates obtained between 1300 on 19 March and 1300 on 21 March 2008. The dotted

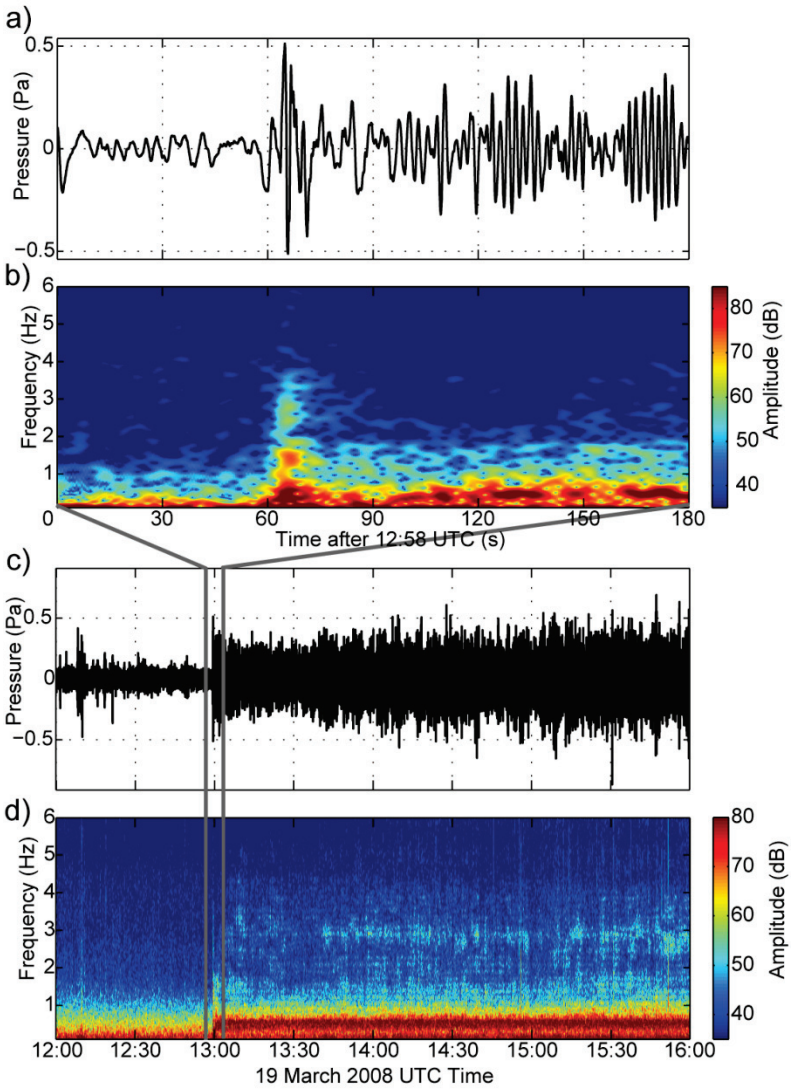

Figure 3.2 19 March 2008 waveforms and spectrograms. a) 0.1-10 Hz beamed waveform and b) 0.1-6 Hz beamed spectrogram for the 19 March degassing burst. The red arrow indicates the decompressional onset, followed by a broadband compression, and then tremor concentrated in the LP band. c) 0.1-10 Hz beamed waveform and d) 0.1-6 Hz beamed spectrogram for the 4 hours encompassing the burst. Continuous tremor follows burst.

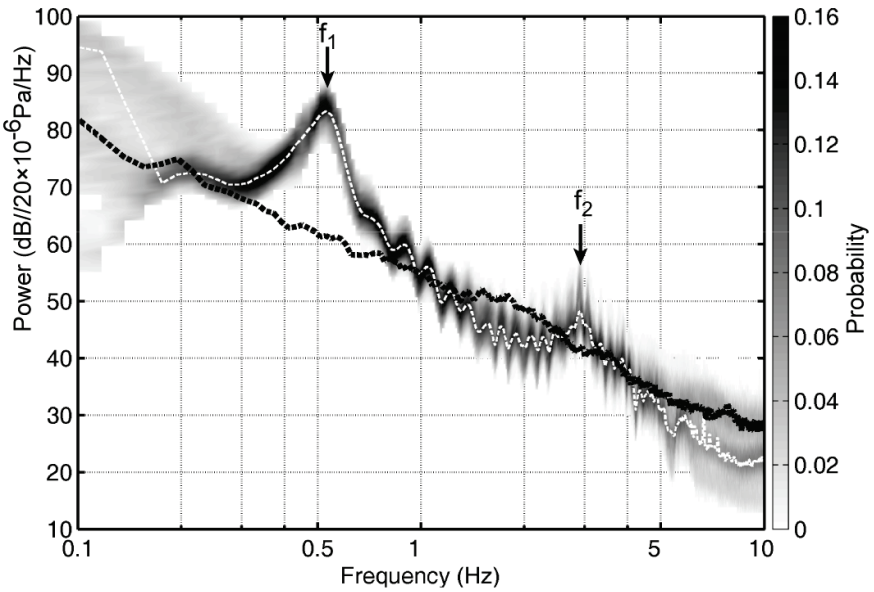

Figure 3.3 Probability Density Function of the PSD between 1300 UTC on 19 March and 1300 UTC on 21 March. The dotted white line displays the peak probability. Note the dominant peak around 0.55 Hz, and the secondary peak at ~3 Hz. The spectral peaks show a high degree of stability in both frequency and power. The dotted black line is the PSD between 1100 and 1130 UTC on 19 March and represents background noise level. The white line represents the maximum probability. Amplitude here and for all PSDs is in dB relative to 20×10^{-6} Pa, the standard acoustics reference.

black line shows a PSD obtained 1 hour before the burst and represents the reference. All of the energy between 0.3-5 Hz originates from Halema`uma`u, while the energy above 5 Hz originates from both Pu`u `O`o and Halema`uma`u. This is typical of spectra during the time period of our study. Spectral peaks for the PSD PDF of tremor are stable with time, varying neither in power nor frequency. In Figure 3.3, f_1=0.53 Hz and f_2=2.90 Hz.

Although the video observations of the vent oscillations in Section 3.4.1 and Supp. Video 3.1 are not time stamped with enough accuracy to directly compare with the infrasound data, the peak tremor frequency during the 30 minute section encompassing the video is 0.53 Hz (Fig. 3.3). Thus the dominant infrasonic tremor frequency during this time period is consistent with the "breathing" oscillation frequency at the vent (0.47 Hz).

In contrast to the Pu`u `O`o tremor recorded by *Fee and Garces* [2007], the tremor from HV does not show diurnal variations. When present, the Pu`u `O`o tremor visible at higher frequencies (>3 Hz) did show diurnal variations. HV is roughly half the distance to the MENE array compared to Pu`u `O`o, thus atmospheric propagations effects should be reduced. Further, the spectral content of the tremor is focused at lower frequencies (<5 Hz) and therefore the station range is closer in proportion to the wavelength.

3.4.4 Degassing Bursts

HV produced numerous transient degassing bursts during the study period. For this study we begin with a list of degassing bursts compiled by *Chouet et al*. [in review], which is based on eruption observation logs compiled by HVO. To this list we add other bursts with significant infrasonic signatures and tephra deposits. Figure 3.4 shows the 0.1-10 Hz beamformed infrasound of the degassing bursts between 19 March and 4 February 2009. Table 3.1 provides a list of the relevant acoustic features of the bursts, including onset time, duration, peak vent overpressure, and total acoustic source energy. Most infrasonic bursts have long durations (>20 s), vent overpressures >5 kPa, and dominant oscillations in the LP band. The acoustic energies tend to increase over time and show broad agreement with the volume changes predicted by seismic VLP modeling [*Chouet et al.*, in review]. The September and October 2008 degassing bursts have the highest overpressures and acoustic energies, and the clearest ILP oscillations. Note most of the burst onsets are not impulsive, and some even begin with a rarefaction (Fig. 3.4).

Clear identification of the degassing bursts in the infrasound records is complicated by the varied nature of infrasonic burst signals, thus traditional detection and identification of transient signals using short-term and long-term average ratios (STA/LTA) [*Fee et al.*, 2010] or cross-correlation techniques [*Jones et al.*, 2008] are unsuitable. An STA/LTA based method incorporating array processing results similar to *Fee et al.* [2010] was run for the dataset, and detected some of the degassing bursts. However, several of the bursts do not have impulsive onsets (Fig. 3.4) and thus are not explosive in nature. For this reason, infrasound burst onsets and durations were selected manually based on the signal between 0.1-10 Hz (LP and SP) rising above/below the

Table 3.1. List of 2008 and early 2009 degassing bursts and acoustic parameters. Onset is the infrasound onset at the vent. Vent overpressure is calculated at 1 m from the vent, assuming spherical spreading.

Burst	Date	Onset (UTC)	Duration (s)	Peak Pressure (Pa)	Vent Overpressure (kPa)	Acoustic Energy (J)
1	19 March	12:58:58	53	0.99	6.78	8.48×10^{5}
2	10 April	09:08:45	14.5	0.54	3.73	6.31×10^{5}
3	16 April	13:58:00	n/a	n/a	n/a	n/a
4	8 July	10:06:41	25	1.67	11.45	3.31×10^{6}
5	8 July	10:38:16	18.3	1.66	11.38	4.46×10^{6}
6	9 July	10:06:59	44	0.43	2.92	5.82×10^{5}
7	9 July	10:33:23	25.9	0.82	5.60	2.22×10^{6}
8	13 July	20:36	n/a	n/a	n/a	n/a
9	2 August	08:45:39	16	1.77	12.13	3.15×10^{6}
10	27 August	17:37:21	40	1.50	10.27	3.83×10^{6}
11	2 September	15:24:05	21	0.81	5.55	1.47×10^{6}
12	2 September	15:35:50	25.7	0.95	6.54	2.56×10^{6}
13	3 September	00:46	n/a	n/a	n/a	n/a
14	3 September	06:13:23	27	2.97	20.40	7.29×10^{6}
15	3 September	08:00:18	36	1.69	11.60	6.15×10^{6}
16	12 October	01:54:22	107.6	1.87	12.81	5.77×10^{6}
17	12 October	17:28:38	33	3.12	21.41	1.59×10^{7}
18	14 October	22:26:41	28	1.27	8.72	6.13×10^{6}
19	15 October	02:06:59	242	1.76	12.10	2.59×10^{7}
20	19 January	01:26:58		0.13	0.89	6.57×10^{3}
21	4 February	23:00:13	30.5	1.45	9.96	1.51×10^{6}

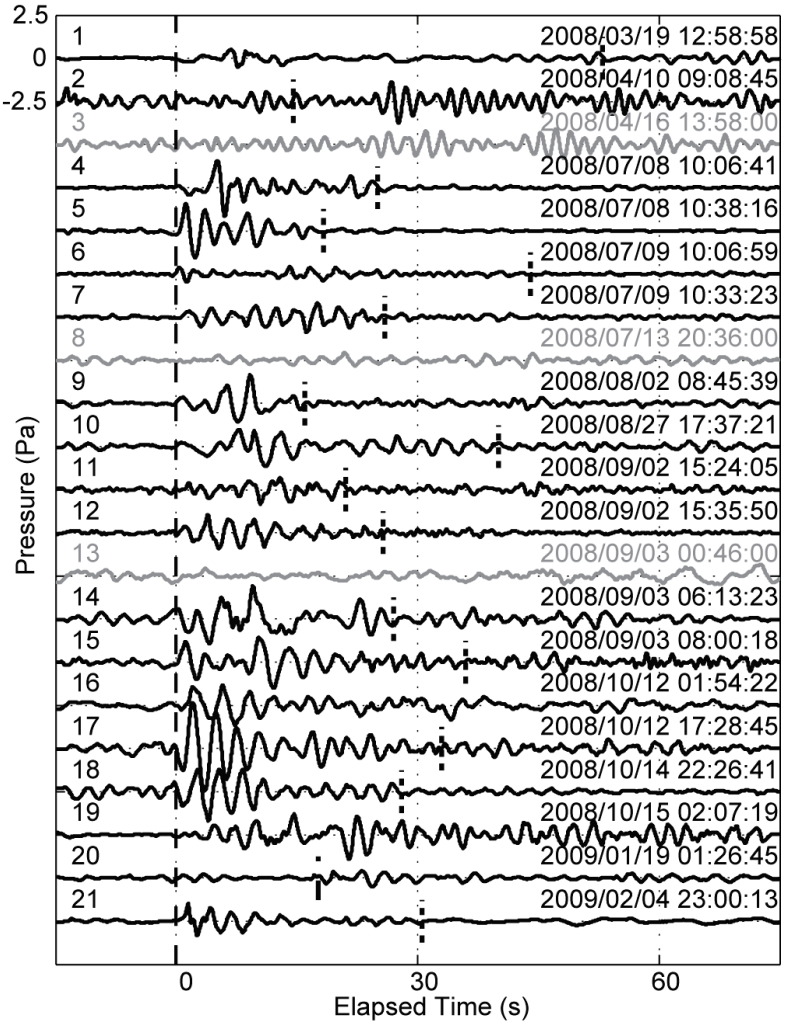

Figure 3.4 0.1-10 Hz beamed waveforms for selected degassing bursts. The bursts are displayed chronologically and number from 1-21. Black bursts have detectable infrasonic signatures, while the gray bursts have no detectable infrasound. The bursts are aligned by the approximate onset time listed above each waveform, which is indicated by the dotted black line at 0 s. The end of the burst is indicated by the dotted black line. The amplitude scale is the same for all bursts.

background levels. Note that due to the energetic tremor present during many of the degassing bursts, the end of the burst signal is difficult to determine for some of the bursts. IVLP detections and durations are considered in Section 3.6.3.

Rather than perform a thorough examination of each burst, here we focus on the 12 October 2008 1728 burst, hereafter referred to as burst 17. Burst 17 (Fig. 3.4) has the highest peak overpressure (3.12 Pa at the station, 21.41 kPa at the vent) as well as the second highest acoustic energy (1.59×10^7 J). Although the burst only lasts 33 seconds, the total acoustic energy is comparable to that of the peak hourly tremor values (~10^8 J). Figure 3.5 is the PSD for burst 17 (gray) and tremor (black) during the hour preceding. The peak tremor frequency during this period, f_1=~0.36 Hz, agrees with the peak frequency of the burst. Higher-order frequency peaks do not show an obvious correlation between the tremor and degassing burst. Video observations reveal the burst emits a dark plume ejected in defined pulses. A substantial amount of juvenile and lithic tephra from this burst was recovered by HVO [*Swanson et al.*, 2009].

Figure 3.6 shows the seismic (gray) and infrasound (black) data for burst 17 split into the VLP, LP, and SP bands. This is done to emphasize the multiple processes involved and to facilitate comparison with established seismic interpretations and source models [*Chouet*, 1996]. Travel time from the array to HV has been removed. Supp. Video 3.2 displays the waveforms from Figure 3.6 time synchronized to a video recording of the degassing burst. Figure 3.7 displays selected frames from Supp. Movie 3.2. Before the burst small oscillations between 0.1-1 Hz at the vent typical of HV tremor dominate. The onset of the IVLP is difficult to determine, as the signal is emergent and the sensor does not have a flat response in this band. However, the IVLP (Fig. 3.6a, black) energy between ~17:28:40-17:28:59 (arrow 1) is clearly detected on all 4 sensors and propagates across the array at an acoustic velocity. The first clear outgassing at the vent occurs at 17:28:42 with a gray plume just after the IVLP energy onset (Fig. 3.7b, arrow 2). The next ~30 seconds are dominated by vigorous degassing pulsations at the vent characterized by an ashy and incandescent plume being pushed violently out of the vent in pulses. Video and waveform comparison reveals these degassing pulses to be coincident in time with the 0.1-1 Hz ILP oscillations (Fig 3.6b arrows 3-4, Fig. 3.7c-f and

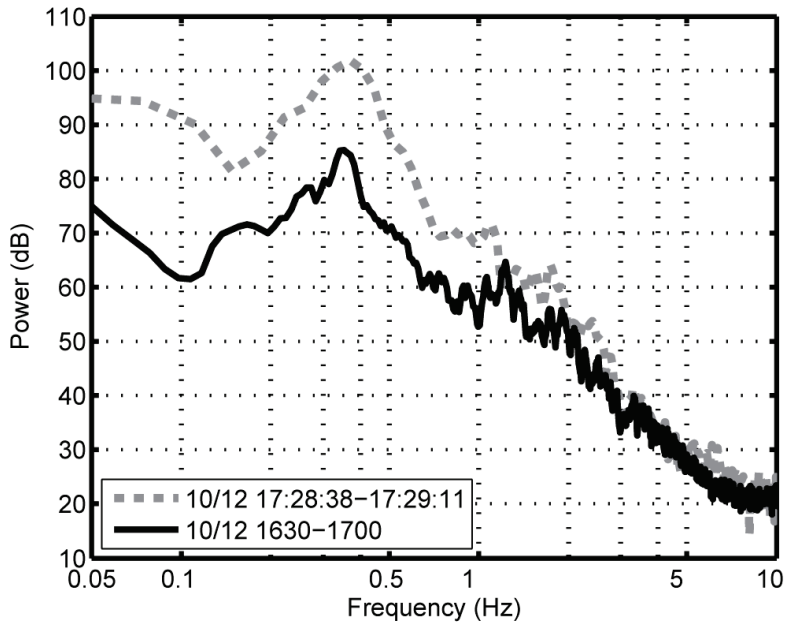

Figure 3.5 PSD comparison for the 12 October 1728 UTC degassing burst (burst 17). The burst PSD (dotted gray line) has nearly the same dominant frequency as the background tremor preceding the burst (black). Higher order harmonics vary between the burst and tremor. Significant VLP energy is also apparent for the burst.

Supp. Video 3.2). These pulsations are reminiscent of the breathing oscillations viewed during the harmonic tremor in March 2008 (Section 3.4.1, 3.4.3), but are more energetic and occur at a much higher velocity. The PSD and filtered waveforms for this burst confirm that most of the acoustic energy is concentrated in the ILP band (Figs. 3.5, 6). Infrasound short period energy (>1 Hz) does not show a clear correlation with vent activity, other than a slight increase in amplitude towards the end of the burst when ash-rich, sometimes incandescent plume oscillations continue. A short period seismic event (arrow 3 in Fig. 3.6c) occurs prior to the IVLP onset and just before the plume oscillations. Although not present in this Figure 3.7, a change in the plume color is evident ~1 minute before the first degassing pulse. The source process for this burst is discussed in detail in Section 3.7.

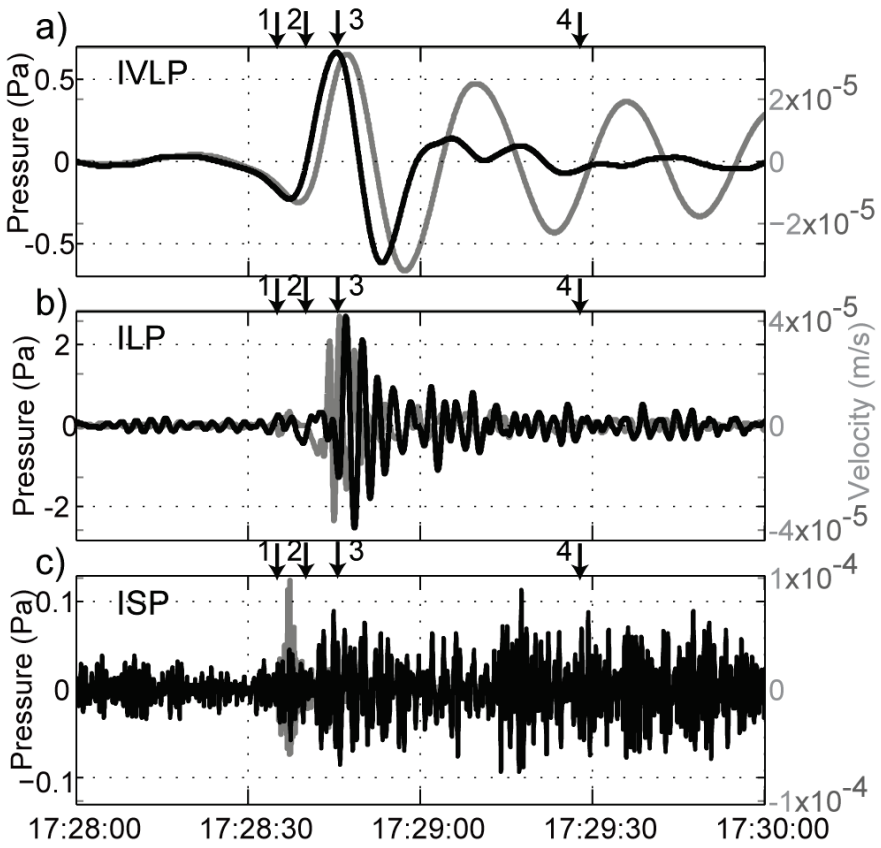

Figure 3.6 VLP a), LP b), and SP c) comparison for burst 17 (12 October 1728 UTC). The waveforms are filtered into three bands: 0.03-0.1 a), 0.1-1 b), and 1-10 Hz c). The infrasound (black) and seismic velocity (gray) both have VLP onsets that begin before the SP rockfall (c, arrow 2). Arrow 1 denotes the VLP and rarefactional IVLP onsets, viewed as the beginning of slug activation. Arrow 2 is the compressional IVLP onset, seen as a proxy for rapid, near surface slug ascent. Arrow 3 is the maximum IVLP compression (corresponding to slug burst in video data). Arrows 4 and 5 indicate the ILP onset and end, which may be indicative of the total slug degassing duration. Energetic LP oscillations are present in both the seismic and infrasound, and both follow the VLP onset. No obvious SP infrasonic signal is apparent, although slightly higher energy signal after the burst onset may be due to small scale jetting or higher order harmonics. Travel time has been removed for all waveforms. The seismic velocity is the vertical component from station NPT. Section 3.7.2 provides further details on interpretation.

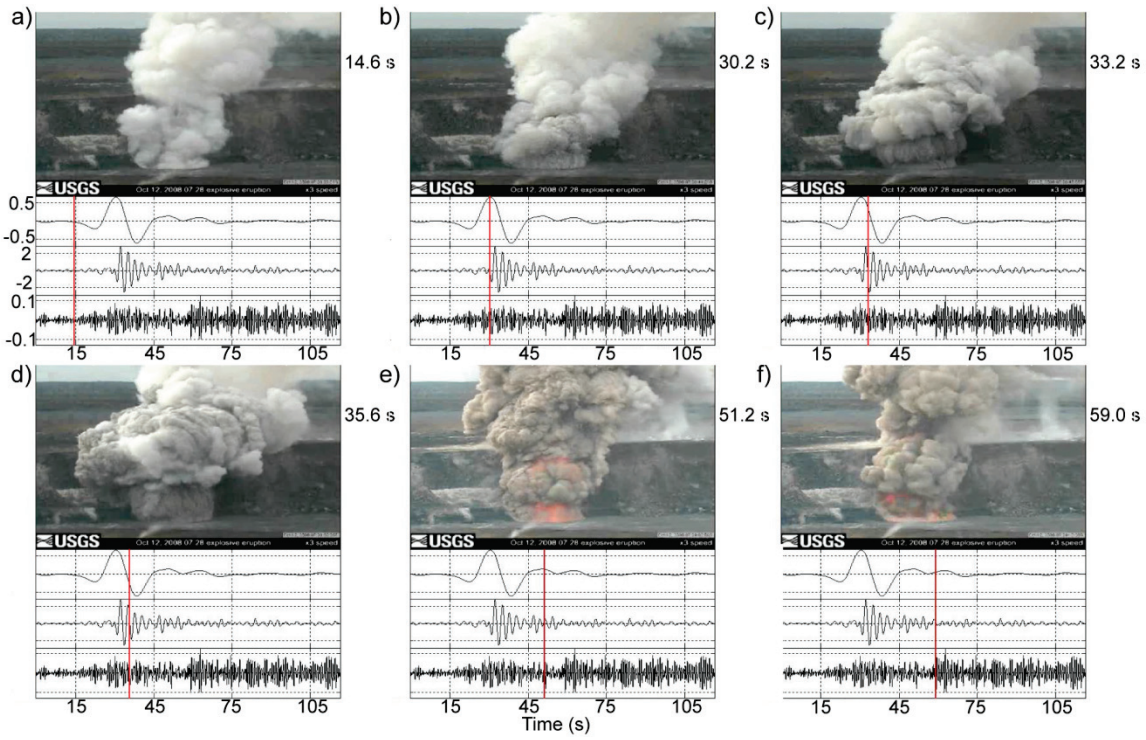

Figure 3.7 Infrasound and video frames from burst 17. The infrasound data around 12 October 2008 1728 UTC is split into the VLP, LP, and SP bands. The VLP onset in a) has no noticeable change in the plume. The VLP compression in b) is synchronous with a large, long period ash pulse from the vent. Energetic LP oscillations begin in c) and d) after the VLP onset and are synchronous with vigorous ash pulsations emitted from the vent. Smaller-scale ash pulses with some incandescent material are present in e) and f).

3.4.5 Collapse and Reactivation of Halema`uma`u

After almost 9 months of continuous tremor, infrasound from HV ceased abruptly on 4 December 2008 1915 (Fig. 3.8). After a brief pause the tremor began again around 2030 and continued intermittently until a final tremor signal at 1559 on 5 December. No explosive burst or acoustic collapse signal accompanied the decrease and cessation of tremor; thus it may be attributed to withdrawal of the magma, followed by small collapses within the cavity that acoustically sealed the conduit. After 1915 on December 4, only higher-frequency harmonics are present (Fig. 3.8).

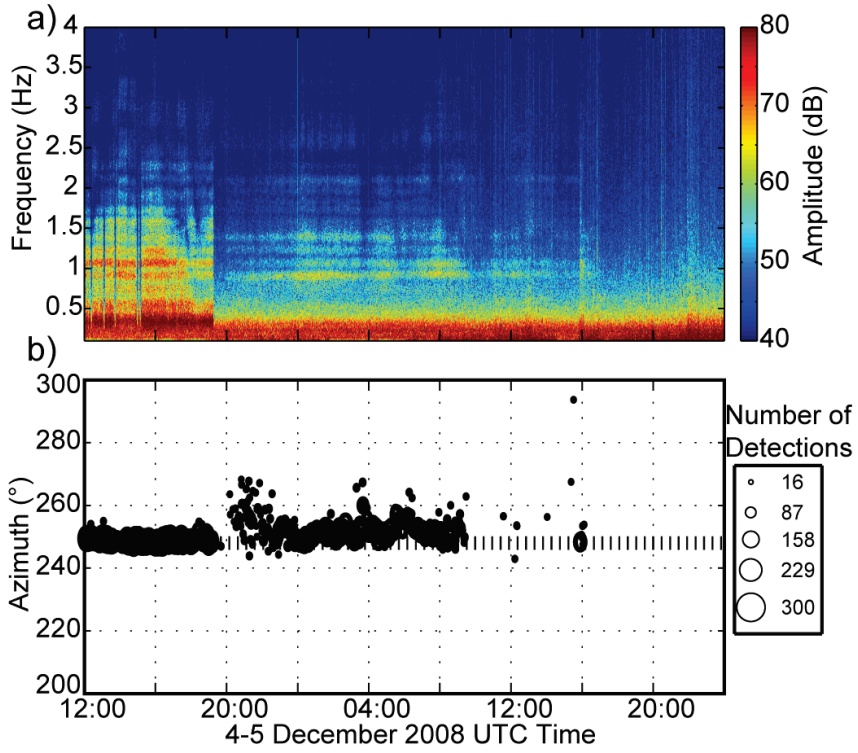

Figure 3.8. Beamformed spectrogram and PMCC plot of 4-5 December 2008 collapse. a) 0.1-4 Hz beamed spectrogram. The collapse event around 1915 UTC is clearly visible. b) Coherent detections of acoustic energy are plotted as a function of azimuth, with HV (250°) marked by the dashed line. The size of the detection is scaled by the number of detections. PMCC is run between 0.5-10 Hz with 20 bands. After the 1915 collapse, only intermittent infrasound is detected from HV. The last HV detection is around 5 December 1600 UTC.

Between 5 December 2008 and 14 January 2009, no infrasound was radiated by HV. During this period reduced degassing still produced a wispy plume, but gas emissions decreased and there was no vent glow. Infrasonic tremor returned to HV at ~1340 on 14 January 2009 and decreased ~2 hours later when signal from Pu`u `O`o began to dominate. Although the HV signal was of fairly low energy, it is clear in the power spectrum between 1 and 3 Hz. F_1 is not apparent during this time period.

Continuous infrasonic tremor resumed on 14 January 2009 until a series of collapses similar to that of 5 December 2008 occurred on 30 June 2009. These collapses were large enough to produce clear, impulsive infrasound signals and eventually acoustically sealed the conduit until 10 August 2009. Infrasound at HV appears to be a good indicator of how well-connected the lava surface is to the atmosphere.

3.5. Resonance

3.5.1. Resonance and Reverberation in a Cavity

Resonance is the natural acoustic response of a contained region, and is an inescapable feature of a sound field interacting with two or more boundaries or fluid discontinuities. To model the possible resonance modes of the tremor and explosion signals, it is necessary to consider the different types of resonance possible. Sustained oscillation within a cavity (resonance) depends on many factors, including the ratios of wavelength of the sound wave to the dimensions of the resonator. If the wavelength is less than the dimensions of the cavity, then two- and three- dimensional standing waves can be produced (acoustic resonance). However, if the wavelength of the acoustic wave is much larger than the dimensions of the resonator, then only volume resonance can occur. In this situation, propagation within the waveguide does not depend on the resonator's lateral dimensions. This type of resonator can be considered a harmonic oscillator with only one degree of freedom (volume) and is termed a lumped acoustic element [*Garces*, 1997; *Kinsler et al.*, 1982].

A Helmholtz resonator consists of a rigid walled cavity with a neck, or opening, and is a common example of a lumped acoustic element. During resonance the cavity behaves similar to a mass connected to a spring. When fluid is pushed out of (or in) the cavity, a lower (or higher) pressure is present within the cavity, which then acts to pull (or push) the air in or out. Assuming an oscillating source is active, this process can repeat itself indefinitely. Similar to the mass-spring system, the fluid in the neck moves as a unit and represents the mass of the system. The acoustic pressure within the cavity provides the stiffness of the spring, while dissipation is due to sound radiating out of the orifice [*Kinsler et al.*, 1982]. A well-know example of Helmholtz resonance is the sound made when air is blown over the orifice of a beverage bottle.

A Helmholtz resonator will reverberate at a single frequency, which can be approximated by [*Kinsler et al.*, 1982]:

$$f_h = \frac{c}{2\pi}\sqrt{\frac{S}{Vk'}} \tag{3.2}$$

where c is the sound speed, S is the area of the neck, k' is the effective length of the neck, and V is the cavity volume. The effective cavity length is $k'=k+1.45a$, where k is the neck length and a is the neck radius. The sharpness of resonance can be estimated by the quality factor, or Q. For a Helmholtz resonator, the theoretical Q is obtained as [*Kinsler et al.*, 1982]:

$$Q = 2\pi\sqrt{V\left(\frac{k'}{S}\right)^3} \tag{3.3}$$

The actual Q of an oscillator can be estimated from the width of the spectral peak, and is defined by the ratio of the center frequency to the frequency band where the energy reaches half of its value.

Although a Helmholtz resonator is predicted to oscillate at a single low frequency, resonance peaks at higher frequencies are possible within the rigid walled cavity itself in the form of standing acoustic waves analogous to waves on a string (acoustic resonance). This type of analysis is most suitable when the ratio of the wavelength to the cavity dimension is between ~1/3 and 3 [*Morse and Ingard*, 1968]. For a typical dimension of the Halema`uma`u cavity, ~200 m, this corresponds to ~0.75-7 Hz (wavelength of ~70-1400 m). Above ~7 Hz geometrical acoustics is a more suitable approach and is not covered here. The pressure amplitude as a function of time for a rigid, rectangular cavity can be defined by [*Kinsler et al.*, 1982]:

$$p(x,y,z,t) = X(x)Y(y)Z(z)e^{j\omega t} \tag{3.4}$$

where *X(x), Y(y)*, and *Z(z)* are the separation constants. We now substitute Eq. (3.4) into the acoustic wave equation and separate the variables. From this we develop a relationship between the three separation constants. Applying the rigid boundary conditions, we can now redefine *p* in terms of normal modes:

$$p_{lmn} = A_{lmn}\cos(k_{xl}x)\cos(k_{ym}y)\cos(k_{zn}z)e^{j\omega_{lmn}t} \tag{3.5}$$

where

$$k_{xl} = l\pi / L_x,\ l=0,1,2\ldots$$

$$k_{ym} = m\pi / L_y,\ m=0,1,2\ldots$$

$$k_{zn} = n\pi / L_z,\ n=0,1,2\ldots$$

and l, m, and n are the standing wave mode indices and L_x, L_y, and L_z are the dimensions of the cavity. This solution of the wave equation thus yields three dimensional standing waves within the cavity. The natural oscillation frequencies within the cavity, or eigenfrequencies, can now be defined as:

$$f_{lmn} = \frac{c}{2}\sqrt{\left(\frac{l}{L_x}\right)^2 + \left(\frac{m}{L_y}\right)^2 + \left(\frac{n}{L_z}\right)^2} \tag{3.6}$$

The eigenfrequencies in (3. 6) an be considered as traveling plane waves in their respective directions [*Kinsler et al.*, 1982]. We can rewrite (3.6), the rectangular chamber eigenfrequency equation as:

$$\left(\frac{2L_z}{c}\right)f_{lmn} = \frac{f_{lmn}}{f_{001}} = \sqrt{\left(\frac{L_z}{L_x}\right)^2 l^2 + \left(\frac{L_z}{L_y}\right)^2 m^2 + n^2} \tag{3.7}$$

If the vertical length L_z and the volume V of the chamber are constrained, we can estimate the cross-sectional area $A = L_x L_y = V/L_z$ and leave only one free variable L_x to find the normalized eigenfrequencies:

$$\frac{f_{lmn}}{f_{001}} = \sqrt{\left(\frac{L_z}{L_x}\right)^2 l^2 + \left(\frac{L_z L_x}{A}\right)^2 m^2 + n^2} \tag{3.8}$$

Now it is possible to plot the eigenfrequencies as a function of only one dimension, L_x, and mode indices l, m = 0, 1, 2, 3… and n=1,2,3….The mode number n is not needed, as these normal modes only propagate in the horizontal directions and no acoustic energy would escape out of the top of the cavity. Axial modes involve interaction with one wall and thus have two mode indices=0, tangential modes involve reflections between two walls (one index=0), and oblique modes reflect along 3 wall (all indices are nonzero). The axial modes will have higher amplitudes than the tangential modes, while the tangential modes will have higher amplitudes than the oblique modes [*Morse and Ingard*, 1968].

For Halema`uma`u, the sound speed within the cavity will be dependent on the temperature and composition of the gas within the cavity. The sound speed in an ideal gas can be found using:

$$c = \sqrt{\gamma RT} \tag{3.9}$$

where γ is the heat capacity ratio, R is the molar gas constant, and T is the temperature. In-situ Fourier transform infrared spectroscopy (FTIR) analysis showed the plume from HV to be predominantly composed of steam and SO_2 (J. Sutton, personal comm.). For simplicity, the sound speed here is calculated assuming the plume is 90% steam and 10% SO_2 and the gases are assumed to behave as ideal gases. The contribution of CO_2 to the sound speed is negligible. An estimate of the average temperature within the cavity is ~200°C from FLIR imagery. Following previously established methods in the literature

[*Kumagai and Chouet*, 2000; *Morrissey and Chouet*, 2001], the sound speed for a gas mixture at this temperature within Halema`uma`u cavity is estimated to be 468 m/s. The wavelength of a 0.3 Hz acoustic wave at Halema`uma`u would then be 1720 m. At 1.5 Hz, the wavelength is 343 m. If the average cavity temperature changes to 100° or 300°C, then the sound speed changes to 415 or 515 m/s, respectively. Note the temperature is estimated from the FLIR imagery taken ~1.8 km away, and may be affected be heating of the wall rock and air entrainment at the vent.

A rigid-walled cavity with an opening at the surface, such as that at Halema`uma`u, should be able to support both Helmholtz and acoustic resonance if the wavelengths and dimensions are appropriate. The area of the cavity neck, *S*, is ~20-30% of the estimated cavity area, *A*. Thus although the top of the cavity is open to the atmosphere, analytically we can treat the vertical dimension as "closed". The closed boundary condition would still permit acoustic energy to be released from the cavity through the neck. The modeling focused on here provides a first examination of the recorded signals.

3.5.2 Resonance at Halema`uma`u

The dominant peak of the infrasonic tremor at Halema`uma`u, f_1, can be modeled as Helmholtz resonance of the Halema`uma`u cavity, while the secondary peak, f_2, and higher-frequency peaks can be modeled as standing acoustic waves within the same cavity. On 14 November 2008 noise levels at MENE were very low, and the power spectrum between 0700-0730 displayed the clearest, most distinct infrasonic tremor peaks during the experiment and is selected for modeling (Fig. 3.9). The peak at 0.22 Hz arrives with an acoustic velocity from 300°, and is of non-volcanic origin. This peak represents the well known microbarom signal produced by the non-linear interaction of ocean surface waves [*Waxler and Gilbert*, 2006; *Willis et al.*, 2004] and is expected within this band. The most energetic peak, f_1, is at 0.35 Hz while f_2=1.07 Hz. All peaks (except at 0.22 Hz) up to 5 Hz arrive from the same azimuth (248°) and have a similar velocity, and thus are assumed to originate from HV.

Constraints on the resonator volume and dimensions are estimated. On 14 November the vent was elliptical with the major axis estimated to be 83 m and the minor

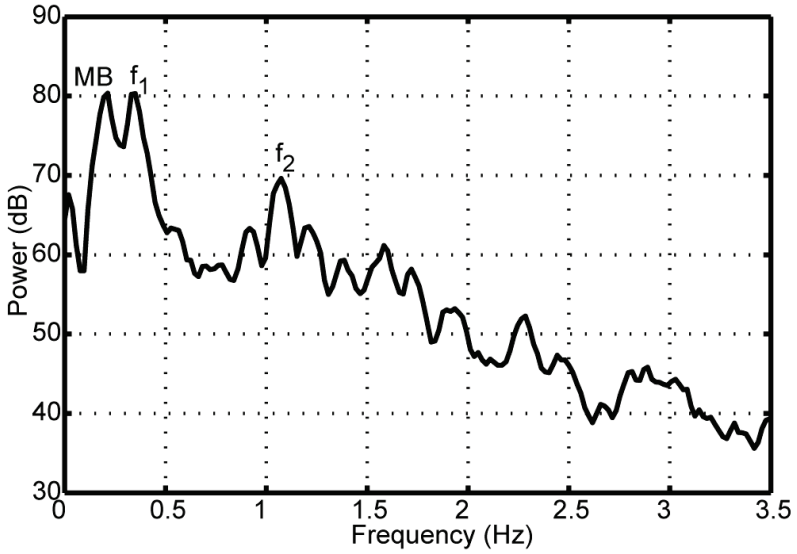

Figure 3.9. Power Spectrum from 14 November 2008 0700-0730 UTC. The first spectral peak at ~0.25 Hz (MB) is the well-known microbarom peak, and is non-volcanic. F_1 (0.35 Hz) can be modeled assuming Helmholtz resonance of HV, while f_2 (1.07 Hz) and its surrounding peaks are consistent with a large rectangular cavity. All energy above ~0.3 Hz originates from Halema`uma`u.

axis roughly 70 m, as derived from daily FLIR imagery undertaken by HVO. The area of the cavity "neck" (*S*) is then found assuming the vent is an ellipse. Visual observations show this depth of the neck (*l*) extends roughly 15 m down into a larger volume. Using the known observations and estimated sound speed, *c*=468 m/s, the volume of the Halema`uma`u cavity can be estimated from Eq. (3.2).to be 2.94×10^6 m^3 on November 14. This is the best constrained estimate available assuming a Helmholtz resonance model as it assumes no specific cavity geometry. The Q of the resonator from Eq. (3.3) is 20.6, which is roughly consistent with the measured Q of f_1 from Figure 3.9, 5.88.

Longitudinal acoustic resonance, a common model for reverberating volcanic conduits [e.g *Buckingham and Garces*, 1996], does not reasonably explain f_1. If f_1 is interpreted to be due to acoustic resonance from the first mode of the largest dimension of the cavity, this dimension on 14 November would be 670 m (3.6). This length is incompatible with visual observations. However, if f_2 and its nearby peaks are generated

from standing acoustic waves within a rectangular cavity, then reasonable cavity dimensions can be estimated from matching the spectral peaks in Fig. 3.9 to those predicted assuming resonance of a rectangular cavity. Assuming f_2 corresponds to the vertical (z-axis) axial mode (f_{001}), the predicted depth is L_z=219 m from (3.6) consistent with the LIDAR measurements from June 2009 (T. Ericksen, pers. comm.). The spectral peak at f_2 also has the highest amplitude above 0.5 Hz (Fig. 3.9), and thus it is expected to be the first axial mode in the vertical direction. If the temperature within the cavity changes from the assumed 200°C to 100° or 300°C, then the estimated depth would change to 194 or 241 m, respectively.

The complicated spectra above 1 Hz can be partially explained by irregularities in the cavity shape. If the volume is a perfect rectangular box, then the assumptions for Eq. (8) will be uniformly valid. However, if the cross-sectional area, A, varies as a function of depth, then the assumption $A = V/L_z$ is not valid for the tangential and oblique modes. To test this we varied A between *1-4A* and found that using *2A* in Eq. (3.8) provides the best fit to the observed spectra, particularly for the tangential and oblique modes. Figure 3.10 shows the normalized eigenfrequency solution space in (3.8) as a function of L_x, using *2A* and assuming L_z=219 m. For L_x≈130-150 m, numerous spectral peaks are matched by the computed eigenvalues, including the axial and two tangential modes (f_{001}, f_{011}, f_{101}). These three modes are predicted to have the highest amplitude. Three more modes also fit in this region (f_{111}, f_{102}, f_{112}). Above ~2 Hz numerous modes are expected and would create a complicated spectrum with numerous degenerate eigenfrequencies (eigenvalues with the same frequency). This is consistent with the observed spectrum (Fig. 3.9) and thus we only choose to match the modeled and observed spectrum below 3 Hz. A full evaluation of the normal modes in nonrectangular, variable dimension cavities is complex and unreliable (particularly for the tangential and oblique modes) unless the irregularities are well constrained. Although we choose *2A* for the area here, the cavity likely changes shape so the area averages out to be A (as predicted by Helmholtz oscillation analysis). A variable cross-sectional area also serves to distribute the sound energy throughout the cavity [*Morse and Ingard*, 1968]. Here we choose to assume a rectangular cavity with a variable cross-sectional area, and are able to satisfactorily fit the first vertical mode as f_2, and a few of the higher order modes.

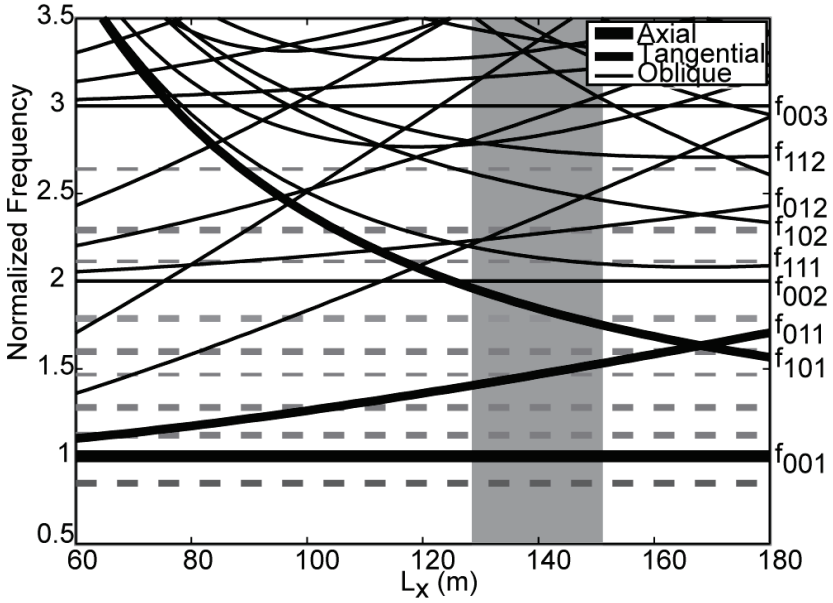

Figure 3.10. Normalized eigenfrequency solution space as a function of the lateral dimension L_x (Eq. 8). The widths of the plotted eigenfrequencies are chosen based on the type of mode, with the vertical axial mode having the highest predicted amplitude. Discernible peaks in the spectrum between 0.5-3 Hz (Fig. 9) are denoted by the dotted gray lines. The thicker lines correspond with the clear, high amplitude spectral peaks. Between L_x=130-150 m (gray box), multiple observed spectral peaks match those predicted. Above 2.5 Hz numerous modes exists and correlation with observed spectra becomes more tenuous. These higher order harmonic peaks are more dependent on source location and spectrum, and are not fit as well assuming a cavity with constant lateral dimensions.

On a more basic level, the distribution of the significant spectral peaks up to 5 Hz is consistent with the Helmholtz and acoustic resonance interpretation (Fig. 3.9,10). F_1 is usually a single peak with no prominent spectral peaks nearby, while f_2 and its nearby spectral peaks are closely spaced and more complicated, as would be expected from multi-dimensional standing waves in a cavity. Figure 3.11 is a cartoon drawing of the cavity at Halema`uma`u, with dimensions inferred from Helmholtz and eigenfunction analysis. Note the lateral dimensions are likely variable.

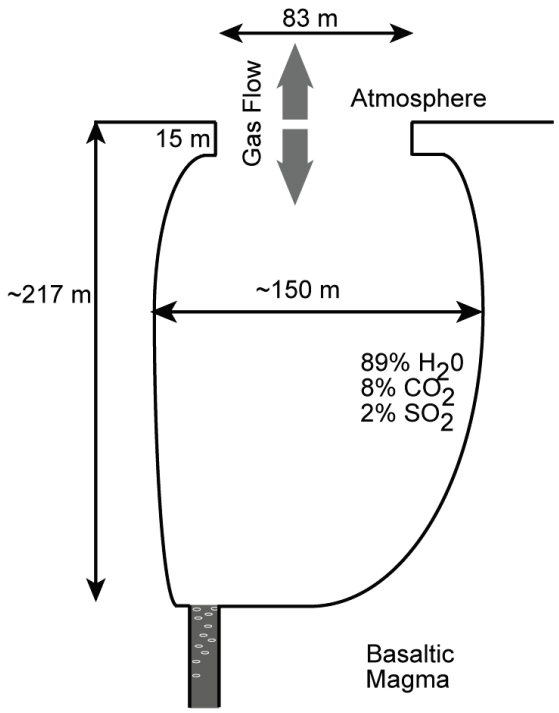

Figure 3.11. Cartoon of Halema`uma`u cavity. Assuming Helmholtz resonance and using eigenfunction analysis of a rectangular cavity, the approximate dimensions of the cavity at Halema`uma`u on 14 November 2008 can be inferred. The vertical dimension is well constrained from LIDAR and acoustic modeling. Comparison of the observed spectra with theoretical modeling suggests the width of the cavity is variable.

Some of the complexity in the spectrum at higher frequencies (Fig. 3.9) could also be explained by variability introduced by the source location or spectrum. As the acoustic source is moved within the cavity (such as varying the magma surface), different cavity modes would be excited. For example, if the source is located at a pressure antinode (corner of the cavity), then it will be able to excite all the modes in the cavity. If the source is placed near the center of the cavity, then some of the modes will only be weakly excited [*Kinsler et al.*, 1982]. A change in the source spectrum (e.g. transient vs. continuous) would also affect the normal modes. This can help explain why the tremor and burst peak frequencies do not agree for the higher order harmonics (Fig. 3.5).

Cavity and volume resonance play vital roles in controlling the infrasound produced at Kilauea. Conceptual infrasonic source models at Kilauea have thus far relied on the acoustic excitation of a contained gas (in conduit, lava tube, etc.) by compression from magma or geometrical constrictions [*Fee and Garces*, 2007; *Garces et al.*, 2003], the oscillations of ascending bubble clouds [*Chouet*, 1996; *Matoza et al.*, in review], or self-sustained jet oscillations impinging on solid boundaries (hole tones) [*Matoza et al.*, in review]. Except for hole tones, these models again appear valid for Halema`uma`u and the persistent tremor source is assumed to be passive degassing from decompression of basaltic magma exciting a cavity into resonance. Evidence for resonance lies in the stability of the tremor frequency peaks, consistency between vent oscillations and dominant tremor frequency, and modeling of spectral peaks assuming Helmholtz and acoustic resonance. The simple calculations of Helmholtz and acoustic resonance for a resonating, steam filled cavity at Halema`uma`u give dimensions which are roughly consistent with visual and LIDAR geometric observations. Lava surface displacements and overpressured bubble burst at the surface may also contribute.

3.6. Changes in Infrasonic Tremor Power and Frequency and their relation to Halema`uma`u Eruptive Activity

Assuming a conduit resonance model, the changes in the tremor frequency and power can be correlated with either changes in the resonator's dimensions or the sound speed of the medium, which is dependent on the temperature and gas composition. This type of analysis provides insight into the overall degassing dynamics. For example, an increase in the degassing (and therefore infrasonic tremor) may be related to an increase in the time derivative of the mass flux. To assess how the power and frequency of f_1 changes over time, beamformed spectra were computed at hourly intervals and the peak frequency between 0.3-0.8 Hz was selected. Figure 3.12 displays both the peak power and frequency of f_1 during the course of the experiment. The background noise levels in this frequency band range from ~70-80 dB. Power levels and peak frequencies for f_1 that were at or below the background noise were rare. Early June had multiple instances where noise was picked rather than signal from HV. After 5 December 2008, f_1 is not present and the picking process only selects background noise.

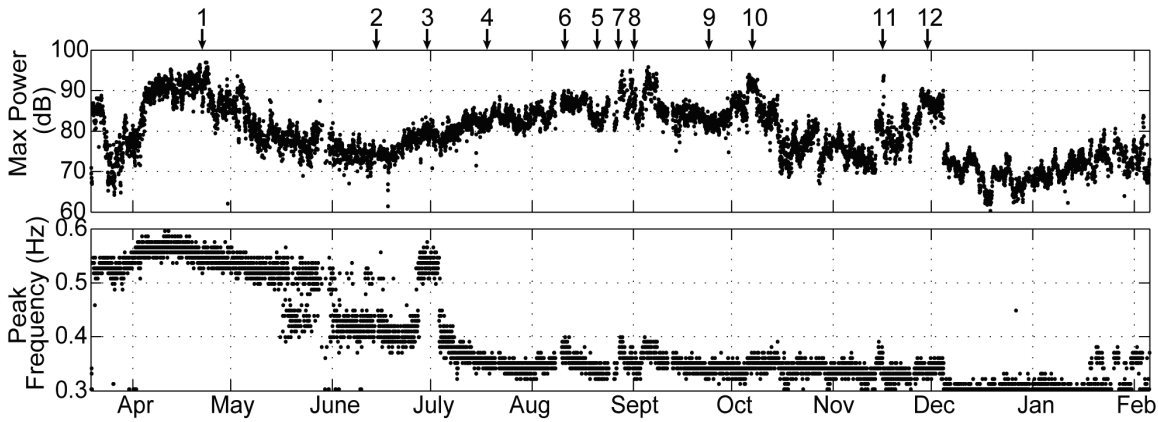

Figure 3.12. Tremor peak frequency a) and power b) during the experiment. Changes in tremor frequency and power can be correlated with changes in the degassing and cavity dynamics. Arrows indicate notable changes in observed tremor, see text for details.

A general trend of decreasing frequency can be seen from early April to December 2008. The cavity volume may increase over time by erosion and/or a drop in magma level. Collapses from the overhanging rim and melting and assimilation of wallrock are the likely erosional processes. Explosive events may also rapidly erode the cavity. The vent temperature also showed a broad decrease over time, suggesting that the plume temperature dropped as well, which could contribute to the lower frequency.

The dominant frequency peak starts at 0.54 Hz in mid-March and slowly increases until peaking at 0.61 Hz and ~97 dB in mid-April (Figure 3.12a,b arrow 1). The rise in peak frequency and infrasound power level could correspond to an increase in the lava level (smaller volume) and possibly volume flux during this period, or to an increase in temperature (and higher sound speed) and degassing.

By mid-June the power levels had dropped almost 25 dB from their peak (Fig. 3.12, arrow 2) and the spectral levels at f_1 were only slightly above the background noise. Numerous other observations suggest a decrease in activity around this time. Seismic tremor, ash production, and vent temperatures were all relatively low. Vent glow was also undetectable. In late June and early July f_1 increases in frequency from ~0.4-0.55 Hz (Fig.

3.12, arrow 3). At this point f_1 is somewhat bimodal and is not as prominent. A variable magma level and degassing regime during this period may be responsible for the change in f_1.

By mid July the tremor power had increased to ~84 dB (Fig. 3.12, arrow 4) and continued an upwards progression until mid August. On 13 July, HV was producing the most audible noise since early April, consistent with the elevated infrasonic tremor levels. In late August and early September, the distinct sound of rock clattering was heard from within HV. Although these sounds had been heard extensively since 3/19, by this date the rock clatters had become quite loud and produced strong echoes, indicative of a rock falling into a large chamber with a significant volume. This is consistent with the infrasonic tremor, as f_1 had decreased to about 0.33 Hz by late August (Fig. 3.12, arrow 5), indicating a large resonating volume. During this period there were also three intervals of increased tremor power (~10 dB increase) and frequency (Fig. 3.12, arrows 6-8), as f_1 rose to 0.4 Hz during each interval. These observations are consistent with an increase in audible noises and vent glow at HV. More vigorous degassing at the vent would raise the tremor power. An increase in the sound speed (mean gas temperature) and/or lava level could cause the increase in f_1. By mid-September the tremor intensity had decreased somewhat (Fig. 3.12, arrow 9).

Mid-October saw another increase in tremor intensity (Fig. 3.12, arrow 10), although no significant increase in frequency occurred. Surf-like sounds at the vent dominated during this period, possibly resulting from gas rushing through the narrow conduit at the base of the cavity, and thus only occurred during periods where the lava level was low. This observation is consistent with f_1's low frequency (~0.33 Hz) compared to earlier periods. It is plausible that degassing intensified during this time, but the lava level stayed low within the chamber. In mid-November (Fig. 3.12, arrow 11) both the tremor power and frequency increase (~20 dB and 0.05 Hz, respectively), but were not accompanied by increased vent glow or seismic tremor.

Intense vent glow in early December is coincident with a substantial increase in tremor power and slight increase in frequency (Fig. 3.12, arrow 12). The vent glow appeared similar to that of a lava tube skylight, indicating that the lava level had possibly risen appreciably. However, a substantial increase in tremor frequency was not detected.

This could be explained by the large volume within the cavity at this period. From March to December the cavity was eroding and increasing in volume, thus a relatively small rise in the lava level may only make a small change in the overall volume of the cavity but increase the vent glow. Surf-like sounds had ceased at the vent as well..

Over the course of the study period, the amplitude ratio of the f_1 to f_2 peaks decreases. On 19 March f_1 was almost 40 dB greater than f_2, while on 14 November f_1 is only 9 dB higher than f_2. Erosional processes removed large portions of the vent rim over time, effectively decreasing the neck portion of the cavity which could decrease the cavity's ability to function as a Helmholtz resonator (Eq. 3.2). No discernible correlation between changes in vent geometry and infrasonic tremor frequency are observed.

3.7. Degassing Burst Source

Recent inverse modeling of the VLP seismic signals from the degassing bursts at HV suggests that they are due to the ascent and burst of large gas slugs [*Chouet et al.*, in review]. Another proposed scenario assumes the viscous lava surface contains a significant quantity of accumulated gas just below the surface. Rocks from the overhanging cavity fall and disrupt the free surface, causing vigorous overturn and degassing within the upper conduit [*Orr et al.*, 2008; *Patrick et al.*, in review], exciting the conduit into resonance. Chouet et al. [in review] show the seismic VLP onset precedes the rockfall, and contend the rockfalls are likely a consequence of conduit deflation due to the rising slug, and not the trigger. However, Orr et al. [2008] have video evidence of rockfalls falling into the cavity and causing energetic degassing. Considering the diversity of infrasound from the degassing bursts, it seems possible that both processes may cause degassing bursts. Gas slugs bursting at the free surface should produce an impulsive signal followed by short duration gas jetting. Unlike Kilauea, acoustic signals from presumed slugs at Stromboli [*Vergniolle et al.*, 1996] and Erebus [*Johnson et al.*, 2008] have durations of only a few to <30 seconds, display a much more repeatable waveform, and have clear compressional onsets. The lack of a clear compressional acoustic onset for the degassing bursts at HV indicates that the source does not have a high overpressure.

Because no unambiguously detectable infrasound begins before the seismic SP and VLP signals (Fig. 3.6), we are unable to constrain whether the source of the degassing bursts are rockfalls or gas slugs. Further work is necessary to validate the source of each of the degassing bursts. However, both scenarios could produce the observed acoustic signals by energetically releasing a substantial amount of gas that excites the cavity into resonance. Cavity resonance for many of the degassing bursts is indicated by the oscillatory nature of the degassing pulsations visible in the video and their correlation with infrasound oscillations between 0.1-1 Hz (Fig. 3.4, 6, 7). Further evidence is found in the agreement between the tremor and burst peak frequencies (Fig. 3.5), suggesting that this resonance is related to Helmholtz volume oscillations. Resonance would also contribute to the long burst durations. ILP Helmholtz volume oscillations and their duration can be considered as representative of the most energetic unsteady degassing process during the degassing bursts.

Resonance is not apparent for some of the degassing bursts, which could result from differences in pre-burst conditions within the cavity. For example, if the lava level was particularly low in the cavity when a gas slug reached the surface, its pressure-release history may be affected by the complicated geometry at the base of the cavity. The slug may also break up on its ascent due to a change in the conduit's geometry [*James et al.*, 2006]. Also, some rockfall-driven events may not be explosive enough to excite the cavity into resonance. Higher frequency harmonics and/or jetting processes above the vent may contribute in the ISP band.

Prior to the 2008 HV degassing bursts, no IVLPs had been detected at Kilauea. To generate an IVLP, a long-wavelength acceleration of the atmosphere is necessary. The arrival of a large gas slug at the surface or the release of a substantial volume of accumulated gas in the upper conduit could both theoretically generate an IVLP. Figure 3.13 shows the IVLP band encompassing the degassing bursts. Only a small number of IVLPs are clearly recognizable: 19 March 2008, 2 September 2008 1524, 3 September 2008 0613, and 12 October 1728. It is possible that some of the bursts have IVLP signals that are indistinguishable from the noise. Most bursts have fairly low noise levels in this band and thus large IVLP signals can be disregarded, particularly during the first half of 2008. More comprehensive study focusing on the acoustic source, seismic-acoustic

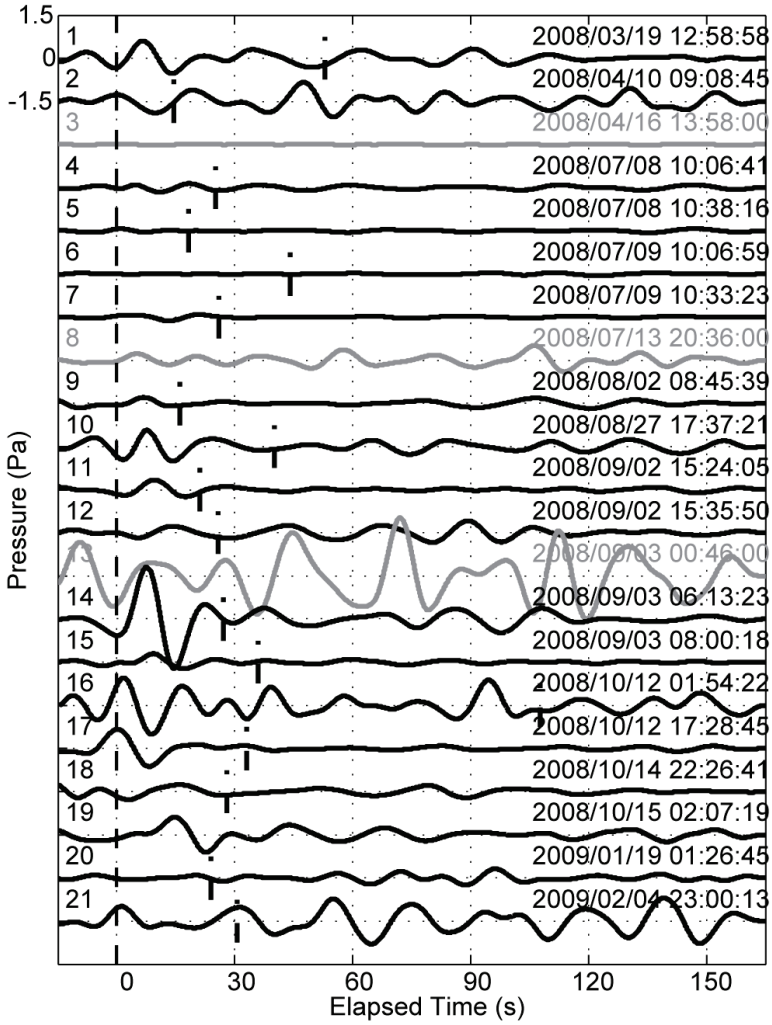

Figure 3.13. VLP infrasound waveforms for the degassing bursts. Gray waveforms indicate no detectable infrasound in the LP and SP band (Fig. 5). The bursts are aligned by the approximate onset time listed above each waveform, which is indicated by the dotted black line at 0 s. Significant VLP infrasound is present for some (e.g. burst 1,11,14, and 17), but not all of the selected bursts. Although noise levels are elevated during some of the bursts, others clearly produced little or no IVLP.

coupling, and comparison to other volcanoes is necessary for a complete understanding of the IVLP source. In mid-2009 an infrasound sensor with a flat response to 0.02 Hz (50 s) was deployed to help constrain the IVLPs at Halema'uma'u.

3.8. Conclusions

Halema`uma`u produced extensive and energetic infrasound for most of 2008, beginning with the vent clearing degassing burst of 19 March and continuing until the tremor cessation and collapse on 5 December, resuming in mid-January 2009. We postulate that persistent degassing from a shallow source within the cavity caused the gas filled cavity to resonate. Modeling the tremor source assuming both Helmholtz and acoustic resonance provides reasonable estimates of the volume and dimensions of the cavity and explains the puffing oscillations at the vent. Changes in the tremor frequency and energetics during the study period are correlated with presumed changes in cavity dimensions, degassing, magma flux, and the lava level within the cavity.

More than 21 discrete degassing bursts were interspersed throughout the study period producing substantial and varied infrasonic signals. Similarly to the tremor, many of the bursts excited the conduit into resonance. This reverberation helped dictate the pressure release history, creating extended durations and vigorous degassing pulsations at the vent. The bursting of gas slugs at the surface or the transient release of gas accumulated in the upper conduit may cause the degassing bursts. Both models could then excite the conduit into resonance and produce the recorded acoustic signals.

This study underlines the importance of the separated gas phase at Kilauea, and how an understanding of both the acoustic source and propagation path is necessary. Geometric constrictions control the type of acoustic signal emitted from the vent, as well as affecting the temperature, seismic-acoustic coupling, and style of degassing. Sources of infrasound and seismicity such as lava tubes, degassing vents, and erupting fissures at Kilauea and other volcanoes may be affected by resonating cavities and geometric constrictions. Infrasound provides a tool for constraining degassing styles and assessing changes in the vent and cavity geometries.

Supplementary Material

3.1. Video of "breathing" oscillations at HV on 20 March 2008. Gas and air are drawn in/out of the vent approximately every 2.13 s (0.47 Hz). The dominant infrasonic tremor frequency during this time period has roughly the same frequency (0.53 Hz). The width of the vent is approximately 40 m.

3.2. 12 October 2008 1728 UTC degassing burst video. The infrasound data is split into the VLP, LP, and SP bands. Travel time from the array to the vent has been removed. The video and data have been sped up by 3 times. Frames from this video are shown in Figure 3.7.

Acknowledgements

This chapter is currently in peer review as: Fee, D., M. Garces, M. Patrick, B. Chouet, P. Dawson, and D. Swanson (in review), Infrasonic Harmonic Tremor and Degassing Bursts from Halema`uma`u Crater, Kilauea, *Journal of Geophysical Research-Solid Earth*. Countless helpful conversations with Robin Matoza helped formalize some of the ideas and text. Darren Hart gratefully assisted with developing the code for deconvolving the sensor response. This work would not be possible without the invaluable help from the Hawaiian Volcano Observatory, particularly Frank Trusdell for hosting the array, Jeff Sutton for providing the gas concentrations, and helpful conversations with Tim Orr and David Wilson. James Robertson and David Whilldin helped with field work and data collection. This manuscript was thoughtfully improved by reviews by Larry Mastin, Stephanie Prejean, and Jim Kauahikaua. This project was supported by NSF Grant EAR-0609669.

CHAPTER 4: INFRASOUND FROM TUNGURAHUA VOLCANO 2006-2008: STROMBOLIAN TO PLINIAN ERUPTIVE ACTIVITY

Abstract

Strombolian to Plinian activity from Tungurahua Volcano, Ecuador has been recorded by the autonomous infrasound arrays of the Acoustic Surveillance for Hazardous Eruptions (ASHE) project since early 2006. Our studies suggest that acoustic energy release during large eruptions does appear to broadly scale with eruption intensity. This manuscript provides a detailed chronology and characterization of Tungurahua's eruptive activity between 2006-2008 and demonstrates the ability to constrain source parameters of significant eruptions, such as onset, duration, and escalation, at regional distances by combining infrasound and remote sensing techniques. The ASHE system in Ecuador automatically detected over 20,000 volcanic explosions at an array 37 km from Tungurahua and was successful at notifying the onset, escalation, and cessation of a hazardous February 2008 eruption with a latency of 5 minutes. Elevated infrasonic energy from sustained and intense Tungurahua eruptions correlates well with ash column heights and their lateral extent during the study period. The spectra of these sustained explosive eruptions appear to be recurrent, readily recognizable, and indicative of volcanic jetting and significant atmospheric ash injection. The paroxysmal Plinian phase of the August 2006 eruption produced an ash cloud that extended well into the stratosphere (>24 km), coinciding with a shift of the dominant jetting frequency from 0.25 Hz to below 0.1 Hz, and radiation of over 5×10^7 Watts of acoustic power. Transient explosions were often marked by minor or no ash release and are presumed to be more gas-rich. A change in the acoustic spectrum of volcanic jetting was also detected in the transition from a sustained to collapsed eruption column at the end of the July 14 2006 eruption. The jetting spectrum at Tungurahua during a period of sustained pyroclastic density current production changes from a typical double-peaked to a single-peaked spectrum, suggesting remote acoustic monitoring can help ascertain the stability and dynamics of an eruptive column.

4.1 Introduction

In early 2006 two infrasound arrays were deployed in Ecuador as part of the proof-of-concept Acoustic Surveillance for Hazardous Eruptions (ASHE) project [*Garces et al.*, 2008] to monitor and mitigate the significant volcanic ash hazard to aviation in this region. The initial goal of the ASHE project was to determine the feasibility of acoustically detecting significant atmospheric ash emissions and rapidly notifying civil defense authorities (ideally, within 5 minutes). The feasibility study has been successfully completed [*Garces et al.*, 2008], and this paper provides details on the methods, salient scientific results, capabilities, and vulnerabilities of this remote sensing technology.

The Washington, DC Volcanic Ash Advisory Center (VAAC) is responsible for ash monitoring for aviation in this region. Existing seismic [*Kumagai et al.*, 2007], gas [*Arellano et al.*, 2008], satellite [*Carn et al.*, 2008], and other technologies currently monitor Ecuador, but the persistently poor visibility, elevated eruptive activity, and remoteness of the region make the task of detecting ash emissions and notifying the necessary authorities challenging. Low frequency (<20 Hz) sound waves (infrasound) propagate long distances with little attenuation and are not affected by the dense cloud cover often present in the region. Further, infrasound is a direct measurement of pressure release into the atmosphere, in this case the eruption of pressurized gas, ash, and lava, and is thus a good indicator of explosive volcanic activity. Accurately differentiating and identifying the character of eruptive pressure release at the volcano is the most difficult and crucial aspect.

Between March 2006-February 2008 near constant and diverse infrasound from Tungurahua Volcano was recorded by the two ASHE arrays. This paper provides a detailed chronology and characterization of the eruptive activity using infrasound and satellite imagery. We expand on the ash monitoring results presented in Garces et al. [2008] and present a companion paper to the satellite-based ash plume observations of Steffke et. al. [2010] , from which the ash clouds heights and dimensions listed here are derived. We focus on five time periods of volcano-acoustic activity. These periods are representative of a common eruption style and/or significant eruption at Tungurahua thus far observed during the experiment: Strombolian (January 2008), Vulcanian (May 2006,

February 2008), Sub-Plinian (July 2006), and Plinian (August 2006). These recordings are noteworthy in that they are some of the highest quality and diverse infrasound measurements of explosive volcanism.

Beyond the monitoring aspect, this manuscript seeks to demonstrate the capability of correlating acoustic records with satellite-derived observations to constrain source mechanisms. For Tungurahua Volcano, we focus on three main aspects: 1) timing: onset, duration, and end of activity, 2) evolution: changes in intensity and character of the signal, in both the time and frequency domain, and 3) source: the physical generation of acoustic energy and how this relates to ash, gas, and pyroclastic density current (PDC) production. The relationship between PDCs and their associated acoustic signals is not currently understood, and this paper provides a unique opportunity to study the infrasound produced from sustained vs. collapsing columns. Further, high quality infrasonic records from energetic silicic eruptions are rare, and this project provides the first detailed, continuous, high fidelity acoustic recordings of all stages of a Plinian eruption.

4.2 Regional Setting and Previous Work

4.2.1 Tungurahua Volcano

Tungurahua is one of the most active stratovolcanoes in the Ecuadorian Andes (Fig. 4.1). At 5023 m, the steep sloped volcano has experienced infrequent but dangerous sector collapses and immense debris flows in its history. Recent activity at the andesitic-dacitic volcano has been characterized by near continuous activity from the central crater in the form of PDCs, lava flows, and ash emissions. Although not located near a major city, over 25,000 residents live in close proximity and within the path of PDCs and lahars [*Hall et al.*, 1999]. The numerous ash emissions from Tungurahua pose a threat to regional and international aviation, and during the study period the VAAC issued near daily advisories (sometimes multiple advisories per day) concerning Tungurahua emissions.

After an ~80 year lull, Tungurahua has seen a resurgence of activity since 1998. Seismic activity increased at Tungurahua between September 1998-1999, indicating

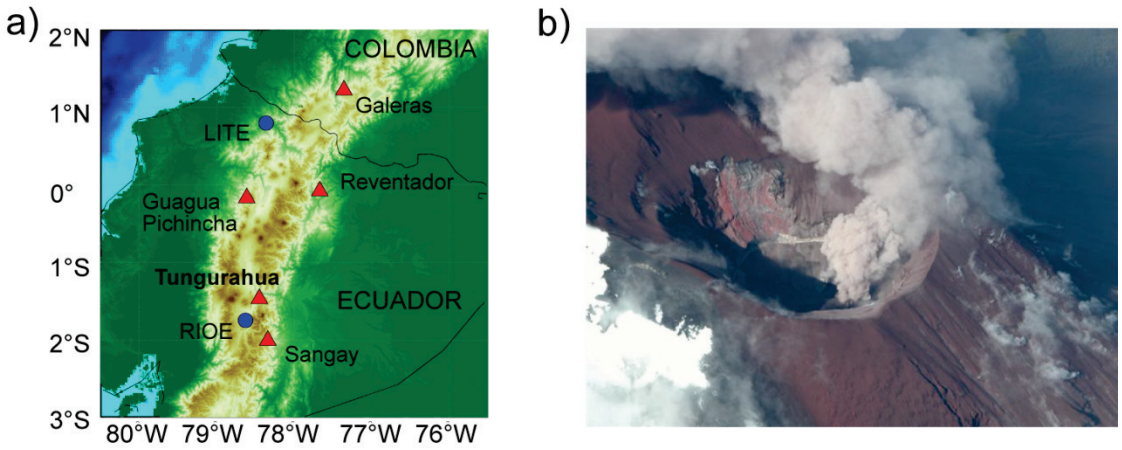

Figure 4.1. a) Map of study area. ASHE arrays are denoted as blue diamonds, while acoustically detected volcanoes are denoted by red triangles. This study focuses on the RIOE array and Tungurahua Volcano. b) Photo of the Tungurahua summit crater after the August 16 eruption. The crater width is estimated at 300-400 m and the depth to >100 m. Photo courtesy of Patricio Ramon (IG).

magma rising through the conduit. In October 1999 magma reached the surface and produced Strombolian explosions. Between October 1999-March 2006 activity alternated between episodes of Strombolian-Vulcanian explosions and lulls characterized by relatively passive degassing in the form of steam or ash emissions [*Arellano et al.*, 2008; *Ruiz et al.*, 2006].

4.2.2 Previous Infrasound Studies at Tungurahua

The Ecuadorian Instituto Geofísico de la Escuela Politécnica Nacional (IG) has operated a multiparameter network at Tungurahua since 1988. Several seismo-acoustic studies have been undertaken at Tungurahua. Johnson [2003] found difficulty correlating seismic and acoustic data because of the high level of seismic background tremor. Another deployment focusing on correlating energy release with eruptive plumes [*Johnson et al.*, 2005] found a poor correlation between total acoustic energy release and eventual plume size. The size of the eruptions described in that study are of much lower magnitude than the case studies presented here. Minor jetting signals were recorded in these studies as well. Ruiz et al. [2006] used waveform similarity to classify acoustic

explosions into distinct clusters. Seismic-acoustic travel time differences reveal the explosions originated at shallow and variable depths within the conduit. Garces et al. [2008] introduced the ASHE project, preliminary results, and its relation to international infrasonic monitoring systems. Using data from the ASHE arrays, Matoza et al. [2009] showed how the infrasound signals recording during large, sustained eruptions at Tungurahua resemble noise from man-made jets.

4.3 Materials and Methods

4.3.1 Equipment

Two four element infrasound arrays were deployed with the aim of detecting and differentiating between multiple volcanoes and other infrasonic sources at regional distances. The RIOE array (Fig. 4.1a) is located 36.75 km southwest of Tungurahua Volcano, 43 km from Sangay Volcano, 214 km from Reventador Volcano, and ~170 km south of Quito, Ecuador. This is the primary array used for this study, as it is the closest to Tungurahua, which is by far the most acoustically active volcano during the study period. The RIOE array aperture is ~150 meters. Assuming a sound speed of 340 m/s, the travel time for an acoustic pulse from Tungurahua to RIOE is ~109 seconds. Although infrasound from Tungurahua volcano dominated at RIOE, signals from Sangay, Reventador, and Galeras Volcano, Colombia (359 km) were also detected.

The LITE array (Fig. 4.1a) is located near the Colombia-Ecuador border, 121 km southwest of Galeras volcano, 124 km from Reventador volcano, and 251 km north of Tungurahua. This location was chosen due to its proximity to Galeras volcano and the predicted first thermospheric acoustic arrival from Tungurahua. The LITE array aperture is ~120 m. During the course of the experiment volcanic signals from Tungurahua, Reventador, Galeras, and Nevado del Huila Volcanoes, Colombia were recorded at LITE.

Chaparral 2.2a microphones were used at both arrays. These sensors have a flat frequency response between 0.1-200 Hz and were sampled at 40 Hz. Data were recorded using 24-bit digitizers and sent by satellite to the Geological Survey of Canada, where it was then forwarded on to the University of Hawaii Infrasound Lab. A broadband seismometer was also deployed at each array.

4.3.2 Remote volcanic monitoring using acoustic arrays

As infrasound technology becomes more widely used to monitor volcanoes, it is important to realize that site selection is crucial to successful monitoring. This project chose to place the acoustic arrays at a safe distance from the active volcanoes in Ecuador and southern Colombia. One of the main benefits of placing microphones arrays at regional distances (approximately 10-200 km) is that it permits the detection and discrimination of multiple volcanoes, one of the prime objectives of the ASHE project. Background noise levels are frequently lower at regional distances compared to the exposed, high wind locations often found near active volcanoes where infrasound sensors are often deployed. There is also less chance of instrument loss from PDCs and other volcanic hazards near the active vent. Easier access to the site can also be facilitated by placing the equipment further away, decreasing the amount of station downtime. The arrays are located in the far-field (where $kr>>1$, with $k=2\pi\times wavelength$ and r=distance to the source), where the non-linear and hydrodynamic effects associated with high source pressure signals are reduced and the monopole radiation component dominates [*Pierce*, 1981]. This project also benefits from its extended duration and consistency of atmospheric variations (primarily diurnal wind changes). Although latency issues arise for long distances, this project finds that propagation, detection, and notification under 5 minutes is still feasible for regional deployments within tens of kms of the volcano.

Regional deployments do have their vulnerabilities. Changes in the atmosphere, particularly the diurnal boundary layer and winds in the troposphere, can affect the acoustic signals at these ranges [*Fee and Garces*, 2007]. Scattering from turbulence and other phenomena may also complicate propagation [*Pierce*, 1981]. The higher frequency acoustic signals will also experience more atmospheric absorption ($\sim 10^{-3}$ dB/km at 10 Hz vs. 10^{-6} dB/km at 0.1 Hz) [*Sutherland and Bass*, 2004], thus the signals at greater distances will be slightly biased towards lower frequency. Further, lower signal levels will be recorded due to geometrical spreading, assumed to be 1/r for RIOE. These vulnerabilities can be minimized by proper site selection and a satisfactory understanding of the atmosphere. Source directionality may also complicate derivation of source parameters for both local and regional deployments [*Garces et al.*, in review].

4.4 Infrasound Detection and Notification Methods

A variety of signal processing techniques are used to detect and identify hazardous volcanic signals. By deploying arrays of sensors rather than single sensors, we can determine the azimuth of coherent acoustic waves as they propagate across the array. This also permits the differentiation between signals of interest, signals that we are not concerned with (termed clutter), and uncorrelated noise. The Progressive Multi-Channel Correlation (PMCC) method [*Cansi*, 1995] is used to detect signals arriving at each array. For RIOE, PMCC is run for the entire dataset between 0.5-4 Hz and split into 10 frequency bands. The 0.5-4 Hz band is where most of the volcanic signals are concentrated. The time segments are split up into 10 second windows with 90% overlap. After PMCC detections are made, they are assigned to "families" based on similar waveform properties. Time-delay beamforming [*DeFatta et al.*, 1998] is used to increase the signal to noise for both the explosion and sustained signal detection. All decibel levels are referenced to 20×10^{-6} Pa.

The ASHE volcanic signal detection system is divided into two main components: explosions and sustained signal (such as tremor and jetting). The acoustic source energy (or acoustic energy) is calculated both for short duration explosions and more sustained sources to determine how energetic the volcanic signal is and how it changes over time. The intensity of an acoustic wave is defined as the average rate of flow of energy through a unit area normal to the direction of propagation, $I=p^2/\rho c$, where p is the excess pressure. The total net outflow (flux) of acoustic energy through a surface is the integral of intensity over the surface. The total acoustic energy can be calculated by integrating the intensity over time and over the surface through which it passes [*Pierce*, 1981]. For a spherical source radiating sound into free space, represented by a sphere with surface area $4\pi r^2$, the acoustic energy can be estimated by:

$$E_a = \frac{4\pi r^2}{\rho c}\int_0^T \Delta p^2(t)dt \qquad (4.1)$$

where r=source-receiver distance, ρ=air density, c=sound speed, and Δp=change in pressure. If a hemispherical acoustic source is located on a flat surface, or the source is buried and radiates through an open vent, the source energy radiates into a hemispherical

volume and the surface area is reduced by 1/2 to $2\pi r^2$, reducing (4.1) by a factor of two. This assumption has been used to estimate the acoustic energy from some volcanoes [*Johnson*, 2003; *Marchetti et al.*, 2009; *Petersen et al.*, 2006; *Vergniolle et al.*, 1996]. However, if the source is just above a surface, in this case a volcanic vent floor, a portion of the source energy radiating isotropically would be reflected back to the atmosphere. For a source placed above a flat, rigid boundary, the acoustic pressure is doubled through reflection (a factor of four in energy) but the total area is halved [*Garces et al.*, in review; *Pierce*, 1981], adding a net factor of two to (4.1). In this study we calculate the acoustic energy using (4.1), the mean between a buried and subaerial source. This may underestimate the energy for sources above the vent (such as jetting), but would overestimate surface and subsurface sources (e.g. explosions) by 3 dB, which is well within measurable field accuracy.

Several caveats must be noted in the acoustic energy calculation. First, it assumes the change in pressure (Δp) is entirely produced by the source of interest, and does not account for contributions from noise or clutter. These unwanted contributors can often dominate, particularly in the far-field or during noisy periods. To minimize the effects of wind noise (the dominant noise source), the acoustic energy here is calculated above 0.5 Hz for automatic processing (also removing contamination from the microbarom signal) and above 0.1 Hz for the high signal-to-noise (S/N) case studies selected here. Note the calculation is thus band-limited as well. In addition, the acoustic energy is only calculated if the array processing results yield coherent acoustic signal arriving from within ±7° of Tungurahua (26°-40° from RIOE). Equation (4.1) also assumes that the source is isotropic and is in a homogeneous space. The complex and dynamic nature of volcanic fluids and pressure release may lead to anisotropic sources, and even relatively simple volcano-acoustic sources have been suggested to be anisotropic [*Johnson et al.*, 2008]. However, calculating the radiation patterns from volcano-acoustic sources is very difficult without proper azimuthal and range sampling. The spherical spreading assumption in (4.1) may also be inaccurate, as the RIOE station is located within the diffraction zone and nocturnal ducts and other atmospheric effects may affect transmission loss [*Fee and Garces*, 2007; *Waxler et al.*, 2008]. Due to the aforementioned uncertainties and assumptions made in acoustic energy estimates,

comparing acoustic energies between different sources and volcanoes must be taken with care. The technique is best used on a comparison basis for single stations and similar atmospheric conditions.

Using the aforementioned method the acoustic energy for Tungurahua was estimated at 5 minute increments for the preceding hour. As an example, Figure 4.2 shows the hourly acoustic energy for on May 12, 2006 0900-1000 UTC. If a high level of hourly acoustic energy is detected, then a notification email is sent to the VAAC and other interested parties. An acoustic source energy of 1×10^{8} J over 1 hour is the selected notification threshold. If the energy level doubles during the next 5 minute iteration, another notification is sent out. Once the energy level drops below the threshold value, a final email notification is sent.

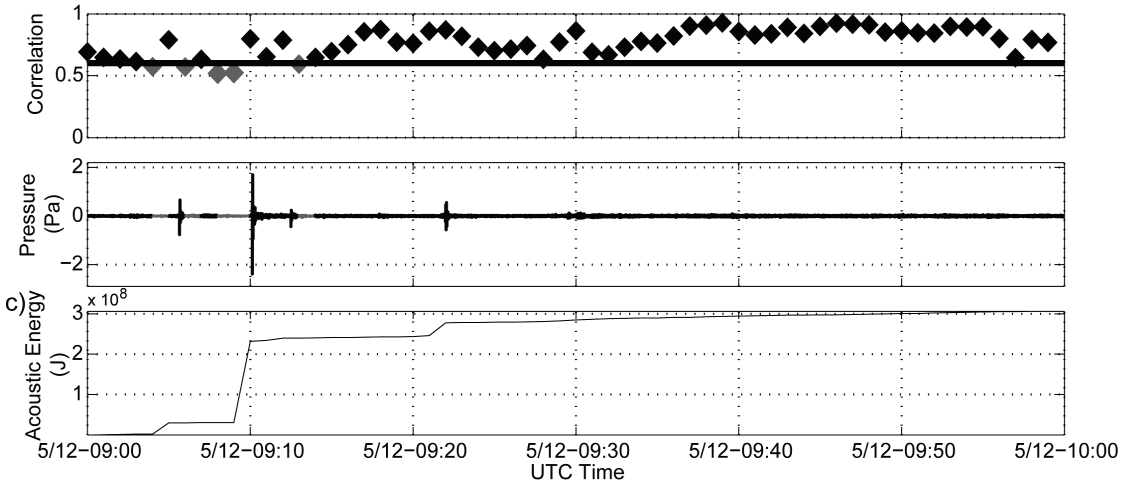

Figure 4.2 Typical hourly acoustic energy calculation. RIOE infrasound array data is band-pass filtered between 0.5-4 Hz and split into 10 sec windows. a) Waveform cross-correlation between the sensors for the time window. Values above 0.6 (black) with azimuths within ±7° from Tungurahua are selected, while grey segments are either unwanted signal or noise. b) Filtered waveforms, with coherent segments colored black. c) Cumulative acoustic source energy for each coherent segment.

Many of the signals recorded during the experiment are sustained over an extended period of time. In order to provide a time-relative measure of the volcano's activity, the acoustic energy is converted to acoustic power by dividing the energy value by the time interval. This is most appropriate for continuous processes, such as tremor and jetting [*Garces et al.*, in review]. If not otherwise noted, the acoustic power levels quoted here are calculated over 15 minute time intervals. The units of acoustic power are watts (W), and are often denoted as megawatts (MW) or 10^6 W in this manuscript. Unless otherwise stated, all energy values are estimated in the frequency band between 0.1-4 Hz.

The explosion detection algorithm for Tungurahua initially high-pass filters the data above 0.5 Hz and runs a STA/LTA (Short term average/Long term average) to determine the onset and end time of any impulsive signal. Two STA/LTA ratios are used, 2/5 and 3/40 seconds, to ensure both impulsive and somewhat more emergent explosions are detected. Next the explosion must be recorded on all four channels, from which it is then associated with the PMCC detections to ensure the signal is arriving from an azimuth within **±7°** of Tungurahua. The coinciding PMCC family must have a minimum RMS amplitude >0.02 Pa and family size >15 frequency/time bins. If these conditions are met, then an explosion is registered and the time, duration, maximum pressure (P_p), and acoustic source energy are recorded. The acoustic source energy is calculated for the explosion duration, and is then normalized by the energy of a reference event to produce the energy ratio (E_r). The reference event is selected from the beginning of the experiment, Feb. 14, 2006, and has a peak-to-peak amplitude of ~1 Pa and source energy of 1.19×10^7 J. The reference event represents a moderate explosion that is unambiguously detected at RIOE. The explosive acoustic energy is normalized to minimize source geometry, propagation, and topographical effects. Once the algorithms were operational, all explosions with E_r>5 triggered a notification email to the VAAC.

4.4.1 Infrasound Monitoring Limitations

During periods of low activity or high noise, the infrasound S/N levels are such that the employed algorithms are not as effective in detecting volcanic activity. Since the arrays have insufficient wind noise shelter, the recordings during the middle of the day (~5 hours corresponding to ~1700-2200 UTC) are often overwhelmed with wind noise

and are not useful for detecting low-level signals. However, during moderate-large explosions (>3 Pa at RIOE) and the three large eruptions (July ’06, August ’06, and Feb. 08), signal levels were high enough to overcome the ambient wind noise during the middle of the day. More regular maintenance of the arrays would also help raise the detection thresholds by assuring sensor and site responses did not vary.

False detection and classification of volcanic signals is fairly minimal, as the algorithms employed were correlated extensively with volcanological observations in case studies before notification services were initiated. Thunder is one potential source of false detection and notification. A thunderstorm between RIOE and Tungurahua was misidentified as a group of explosions from Tungurahua due to the shared impulsive and transitory nature of both processes. No obvious tremor misidentifications were made, but the possibility cannot be completely ruled out. The low number of false detections can be partially attributed to the exhaustive and detailed monitoring of Tungurahua Volcano by the IG.

At greater distances (e.g. 200 km or more) seasonal changes in wind conditions, particularly at higher latitudes, may affect the detectability of infrasonic signals [*Le Pichon et al.*, 2009]. Preliminary analysis shows that acoustic signals from Tungurahua recorded at LITE likely propagate through the thermosphere, and because of the low latitude and north-south propagation path, are not substantially affected by the seasonal variations in stratospheric winds. For stations at higher latitudes, such as the ASHE arrays at Mount St. Helens, USA (~45°N) [*Matoza et al.*, 2007], longer range detection will be influenced more by stratospheric east-west wind variations.

Large explosions can bias the acoustic energy/power calculations, and a more effective way of separating explosions and tremor levels would be helpful. However, the relationship between explosions, tremor, and ash production is complex and not fully understood. For example, large explosions followed by harmonic, gliding tremor may be representative of gas-rich, ash-poor eruptions (e.g. Section 4.5.2 and Section 4.5.5), and multiple episodes of jetting are preceded (and possibly initiated) by large explosions (e.g. towards the end of the February 6, 2008 eruption, onset of July 14, 2006 eruption, and around 0435 on August 17, 2006).

4.5. Results

4.5.1 Experiment Results

Between March 2006-February 2008, 19,865 explosions were detected at RIOE, with over 3500 of those detected at LITE as well. The peak pressures of these explosions at RIOE range from 0.03-24.43 Pa (Fig. 3a). The largest explosion saturated the sensors (>25 Pa) on July 17, 2006, and thus is even more energetic. Assuming spherical spreading, this correlates to a peak pressure of over 900 kPa at the vent and is comparable to some of the largest explosions recorded to date by infrasound microphones at near or regional distances Figure 4.3 shows both the raw amplitude of each explosion and number of explosions detected per day. Approximately 99% of the explosions are less than 5 Pa. The number of explosions per day ranged from 0 to a peak of 443 on January 25, 2008, which was characterized by energetic Strombolian activity [*Vergniolle and Mangan*, 2000].

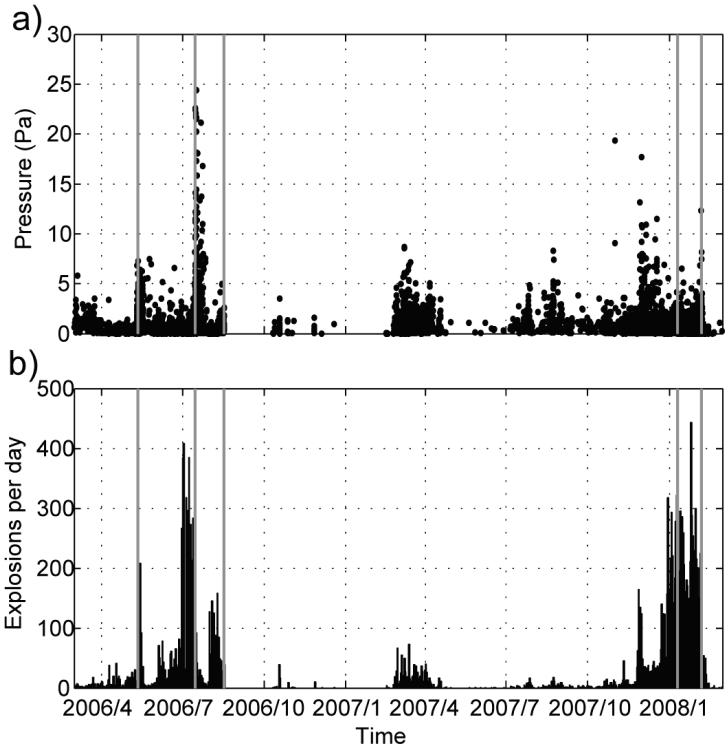

Figure 4.3 Tungurahua explosions detected at RIOE. a) Raw pressure amplitude (P_p) and b) numbers of explosions per day. The gray lines indicate times of the case studies selected here.

For much of the period, background volcanic activity is characterized by minor ash emissions and a dominant tremor frequency of 1.4 Hz [*Garces et al.*, 2008]. The 1.4 Hz tremor is characteristic of relatively passive degassing and minor ash emissions. Explosions are interspersed with the 1.4 Hz tremor and show no obvious correlation. Numerous instances of energetic volcanic jet noise are recorded as well [*Matoza et al.*, 2009], and they all occur during the three large eruption sequences (Feb. 2008, July and August 2006) that will be covered in subsequent sections.

Coherent acoustic energy from Tungurahua is detected at RIOE during most of the experiment. Figure 4.4 shows the hourly coherent acoustic source energy at RIOE divided into three categories: low (10^5-10^7 J), moderate (10^7-10^9 J) and high (>10^9 J). The July 2006, August 2006, and Feb. 2008 eruptions all have sustained acoustic energy above 10^9 J/hr (~2.8 MW). Other instances of high acoustic energy are from numerous or large explosions within the hour. Lower level activity is characterized by minor ash emissions associated with the 1.4 Hz tremor and intermittent Strombolian explosions.

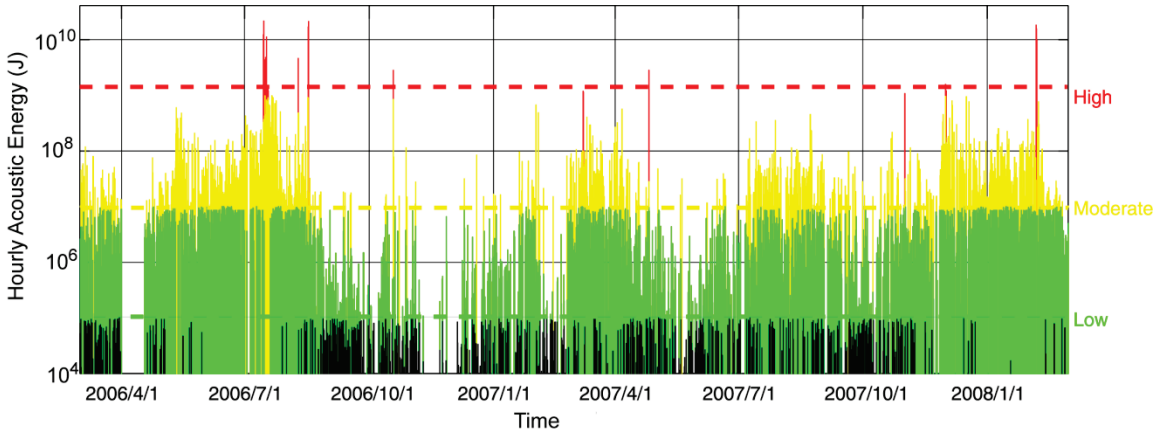

Figure 4.4 Hourly acoustic source energy for the experiment. The energy values are split into three levels: low (green) between 10^5-10^7 J; moderate (yellow) between 10^7-10^9; and high (red) above 10^9 J. Dashed, colored horizontal lines indicate the three threshold energy levels.

Five case studies are now presented in detail, with an emphasis on the acoustic recordings at station RIOE. Each period represents either a large eruption or is typical of a common eruption style at Tungurahua volcano during the study period. All of the ash plume observations here are derived in Steffke et. al. [2010] and are only briefly mentioned here. All times listed are in UTC and ash heights listed are elevation above sea level.

4.5.2 May 11-15, 2006

In mid-May 2006, eruptive activity increased at Tungurahua volcano to levels not seen since October 1999. Seismic events began to focus at shallow (0-4 km) depths in April and early May. On May 11 the number of explosions and long period (LP) seismic events increased dramatically [Smithsonian Institution, 2006]. Activity remained elevated over the next 5 days and was characterized by large explosions with little ash. May 12 is selected as a case study as it has the most cloud-free satellite images for this period and contained significant acoustic activity. Activity between May 11-15 is similar to the 12th. Figure 4.5 shows the raw waveforms (a), spectrogram (b), and detected explosions and acoustic power (c) for May 12, 2006.

On May 12, 2006, ninety-seven explosions were detected at RIOE, with 37 having an $E_r>1$. Some of these explosions were heard in nearby towns almost 30 km from Tungurahua. Moderate to strong explosions occurred regularly throughout the day, with the largest explosion having a peak pressure of 7.8 Pa (Fig. 5a) at RIOE (~287 kPa at the source) and $E_r=21.5$. Time-averaged 15 minute power levels of sustained activity ranged between ~0.2-1.2 MW (Fig. 5c). Most of the acoustic power is due to explosions, not sustained tremor (Fig 5a). Despite the energetic acoustic activity, no ash plumes are detected in satellite imagery. Discrete volcanic explosions can produce instantaneous plumes, or thermals, if the explosion is short relative to the plume ascent time [*Sparks et al.*, 1997]. The IG reported nearly all of the May 12 explosions, but the associated emissions either have low ash content or are comprised primarily of steam and some gas. Some of the explosions ejected incandescent blocks. No thermals were detected by the IG either. The explosive sources for these events are clearly well-connected to the

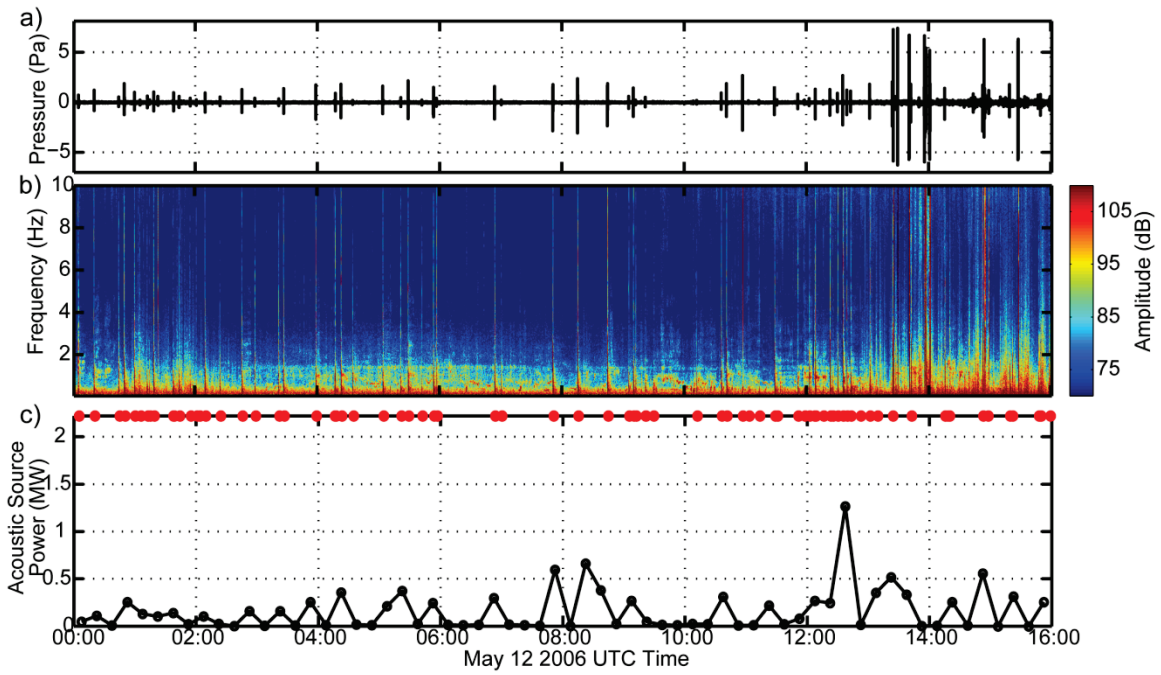

Figure 4.5 May 12, 2006 a) raw (unfiltered) beamformed waveform, b) spectrogram, and c) acoustic power (black line) and detected explosions (red dots). Numerous energetic explosions were detected through the day, but no ash plumes were detected in the satellite imagery. Decibel levels for the PSD and spectrograms are referenced to 20×10^{-6} Pa/Hz$^{1/2}$ and are not range corrected. Assuming spherical spreading, the transmission loss at 37 km is 91 dB. All spectrograms and PSD in this manuscript use the same convention.

atmosphere and have significant overpressure. Activity during this period is best described as Strombolian.

The 1.4 Hz background tremor was at low levels and fairly constant throughout the day (Fig 5b). However, the most prominent tremor has a dominant peak below 1 Hz, exhibits gliding (frequency shifting of the spectral peaks) (Fig. 6), and is frequently preceded by large explosions. The gliding tremor is relatively rare in the dataset.

The activity of May 12 was unusual in that the energetic explosions and tremor produced little ash. Examining the waveform features for the May 12 explosions shows

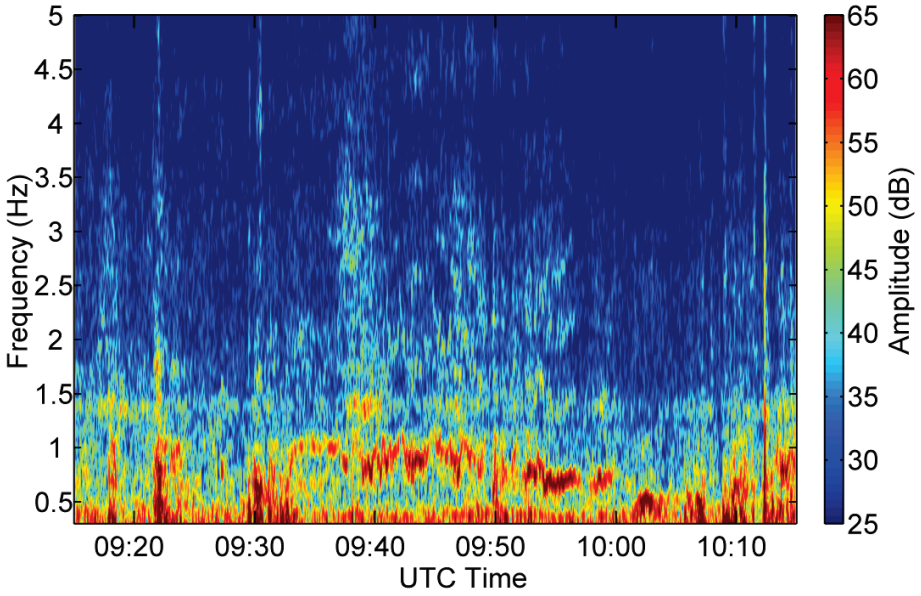

Figure 4.6 May 12, 2006 0915-1015 UTC spectrogram between 0.3-5 Hz. Explosions during this time period are followed by harmonic, gliding tremor. Background 1.4 Hz tremor is also intermittently present.

they exhibit a high degree of similarity. Most of the explosions are characterized by an impulsive compressional phase, average durations of 7 sec, and an often complex rarefaction phase (Fig 7a). To quantitatively evaluate the similarity of the explosions, basic waveform cross-correlation was performed on all 35 selected explosions for this day following methods similar to that of Green and Neuberg [2006]. Explosions with E_r>0.4 were selected, then beamformed, filtered between 0.1-10 Hz, and cross-correlated against the master waveform. Figure 4.7a shows the explosion waveforms (gray) and master (black), and stacked waveform for all the selected explosions (white), while Fig. 7b shows the cross-correlation values between each explosion relative to the master. All of the explosions have high cross-correlation values above 0.75, and most are above 0.9, indicative of similar source processes and minimal changes in propagation induced effects for the selected waveforms. Cross-correlation of the May 12, 2006 master with

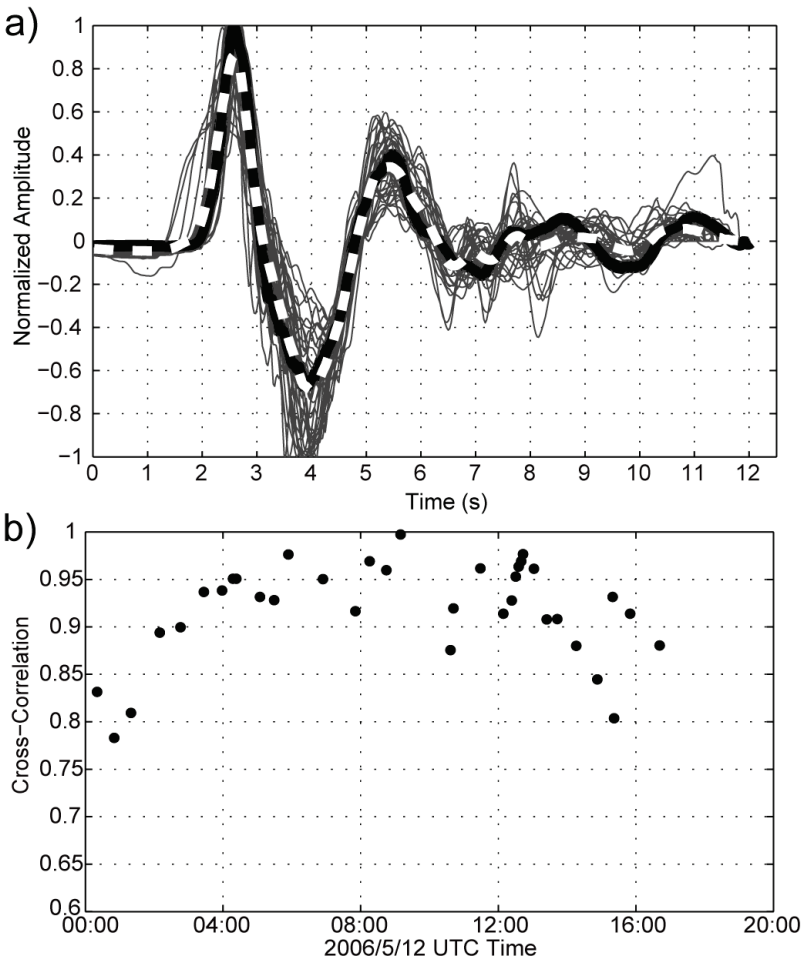

Figure 4.7 May 12, 2006 waveform a) and b) cross-correlation results. Explosions with E_r>0.4 are selected and time aligned in a). The black line denotes the master waveform, while the dotted white line indicates the stack of all the waveforms. Each waveform is cross-correlated against the master with the correlation value in b). Most waveforms are highly correlated with correlation values above 0.9.

explosions prior to the July 2006 eruption shows a decrease in the correlation value (~<0.75), as these waveforms have different features.

It is conceivable that a "master" waveform representative of this type of explosion could be constructed and used in a detection algorithm. For example, the explosion detection algorithm could cross-correlate the newly detected waveform against a "master" ash-poor explosion waveform to determine if the new explosion constituted an ash hazard. However, before this could be done a comprehensive waveform cross-correlation study would have to be performed to determine the reliability of this type of test. Neural network identifiers [e.g. *Ham et al.*, 1999] or other waveform similarity methods [*Ruiz et al.*, 2006] may also be appropriate. It is unclear whether the majority of ash-poor explosions at Tungurahua always have similar waveform characteristics to those of May 12, 2006. This question is beyond the scope of the current study.

4.5.3 July 14-15, 2006

On July 14-15, 2006 a destructive Subplinian eruption occurred at Tungurahua producing numerous pyroclastic flows and a substantial ash cloud to ~14 km. The eruption had an estimated dense rock equivalent (DRE) volume of magma of ~10^6 m^3 [*Arellano et al.*, 2008] and a total SO_2 discharge of ~12,000 tons [*Carn et al.*, 2008]. We estimate the VEI at 3 from the ash cloud heights and duration. In the days preceding the eruption only minor increases in explosive activity occurred [*Smithsonian*, 2006]. Figure 4.8 shows the filtered waveforms (a), spectrogram (b), and acoustic power and ash height (c) for the July 15 eruption.

A moderate explosion occurs on July 14 2234 and signaled the onset of the major eruption. This Vulcanian explosion most likely cleared the conduit and is coincident with the onset of magma fragmentation and ash emissions. Jetting follows the explosion and acoustic power slowly rises from 1 to 2.2 MW by 2345. This is the first instance of intense volcanic jetting recorded at Tungurahua during the experiment. The first satellite imaged ash cloud occurs at 2245 with a height of ~6 km. The plume increases laterally between 2245-2345 and rises to ~13.5 km. The first PDC was reported at 2315 [*Barba et al.*, 2006], but no distinctive PDC-related infrasound signal is obvious in our records, likely due to the energetic jetting overpowering the PDC signal. Between 2345-0045 a

large increase in the plume intensity and lateral extent is observed, and the infrasound power levels rise from ~2.2 to 4 MW. Another large explosion occurs at July 15 0011 (P_p=5.31 Pa, E_r=5.19).

Between 0045-0130 UTC the jetting energy is focused at lower frequencies (<1-2 Hz) and infrasound power levels rise rapidly to 9.3 MW. However, no major change in plume height is evident in satellite imagery. The plume reaches a height near its maximum by 0045, although the infrasonic power levels continue to rise until around 0130 and then decrease for ~30 minutes, only to rise again to a peak of 9.8 MW between 0215-0230 (Fig 8c). These unsteady oscillations in acoustic energy may be typical of sustained jets. Although there is no observable major change in the ash column height associated with the rises in acoustic power between ~0100-0230, the maximum lateral extent of buoyant ash cloud occurs around 0230-0330. A large circular plume attached to the vent is apparent in the satellite imagery at 0215 (Fig. 4 in [*Steffke et al.*, 2010]).

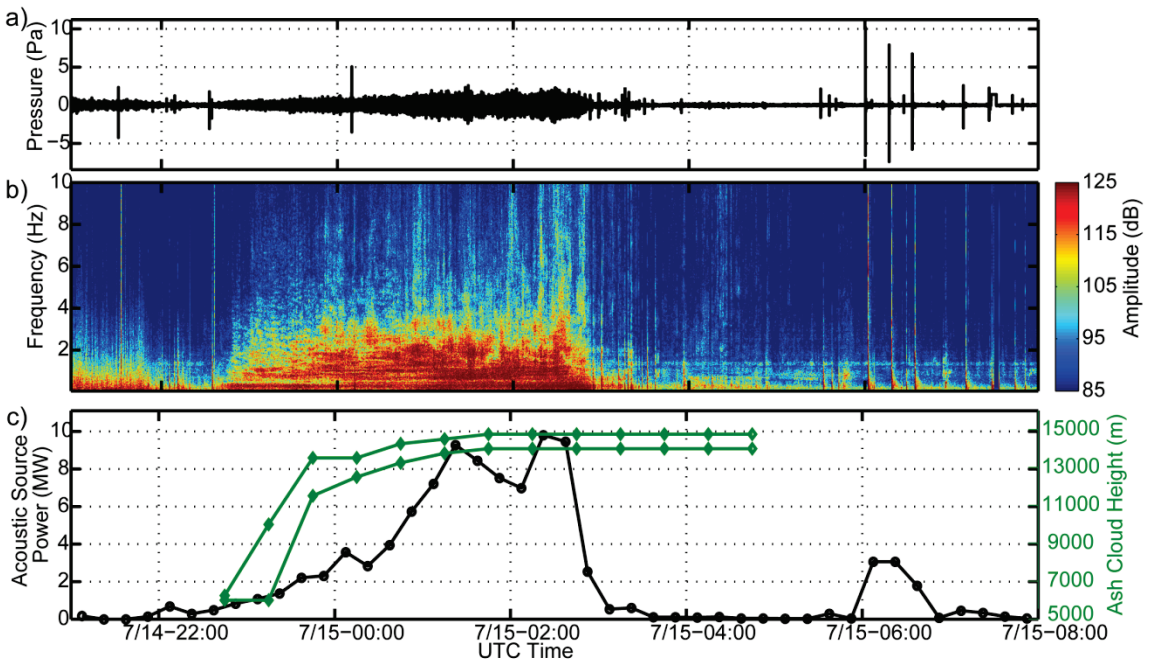

Figure 4.8 July 14, 2006 a) raw waveform, b) spectrogram, and c) acoustic power (black line) and ash cloud height (green). The two ash cloud heights given are maximum and minimum, as derived from satellite imagery. Acoustic power broadly correlates with ash cloud heights.

Because the plume has a high aspect ratio (circular), it is likely that gravitational settling, not wind, is the dominant dispersal mechanism. It is also possible that the ash height peak does not coincide with the maximum acoustic power due to atmospheric effects. The tropopause is located between 16-17 km above Tungurahua and could serve as a deterrent to the rising ash cloud due to the significant temperature inversion at that height.

An interesting and unique sequence in this dataset occurs where a large PDC was captured in FLIR imagery taken by the IG around 0250 (Fig. 9). The infrasound power levels and jetting taper off rapidly around 0245 and the main plume detaches from the vent soon after. Even though infrasonic power levels decrease after the typical jetting signal ends at 0245, significant eruptive activity continues as numerous PDCs descend into local communities [*Barba et al.*, 2006]. This is coincident with the time the

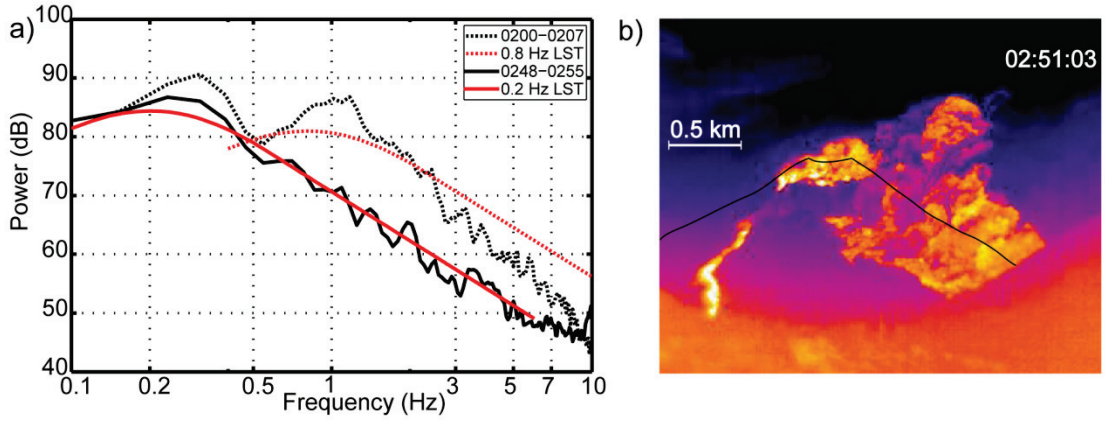

Figure 4.9 PSD comparison for sustained vs. collapsed columns. a) Selected PSDs for July 15, 2006. The dashed black line is the spectrum during a time period of sustained jetting with a vertical ash and gas column above the vent. The dark black line indicates the spectrum during a period where the column has collapsed to feed PDCs. The red lines indicate the LST spectrum centered at different frequencies. Note there is no "notch" in the spectrum for the PDC period, only a single peak centered at ~0.25 Hz. b) FLIR image from July 15 02:51:03 UTC showing a large PDC descending the volcano and no sustained vertical column. This time period coincides with the single peaked spectrum (black line) in a).

infrasound power levels decrease and a change in the frequency content occurs. Figure 4.9a shows a comparison of the power spectral density (PDF) during a period of intense jetting with a sustained lava and ash column (July 15 0200-0207) versus that during the collapsed column only portion (July 15 0248-0255). The jetting spectrum between 0200-0207 is typical of that at Tungurahua [*Matoza et al.*, 2009] and during the main jetting phase of this eruption: July 14 2245 - July 15 0230. This period also coincides with a sustained ash column. The spectrum following 0245 is roughly similar to the typical jet spectrum below 0.5 Hz, but has a sharper roll-off in the acoustic energy above 0.5 Hz (Fig. 9a). This is true of the entire spectrum between 0245-0315. Numerous PDCs were reported between 0315-0540 [*Barba et al.*, 2006] with only a minor ash plume being driven by the PDCs. Activity at the vent during this period as captured by the FLIR camera is characterized by dense PDCs starting just above the vent and occurring in pulses. No large vertical plume is visible in the FLIR or satellite imagery, thus the acoustic source is likely within or near the crater. Infrasonic power levels decrease until 0540 and the spectrum retains a similar shape with a single dominant spectral peak around 0.25 Hz. Energetic explosions occur after ~0500 UTC, coincident with the appearance of a small ash cloud below 8 km, but no obvious correlations with PDCs or other activity are apparent. Remarkably, the steady 1.4 Hz tremor resumes at ~0315 and continues unabated. These PDC signatures will be addressed in more detailed in Section 4.6.4.

4.5.4 August 16-17, 2006

On August 16-17, 2006 the most destructive and energetic eruption in Tungurahua's recent history occurred. Over 30 PDCs were observed [*Barba et al.*, 2006], and the estimated DRE for this eruption is $\sim 2 \times 10^7$ m^3 [*Arellano et al.*, 2008] and SO_2 emitted was over 35,000 tons [*Carn et al.*, 2008]. We estimate the eruption to be a VEI 4, primarily from the ash height (>24 km) and extended duration (~11 hours). After a lull in activity following the July 14 eruption, activity at Tungurahua increased in the days preceding the August 16-17 eruption. A large bulge on the N flank of the volcano grew between August 11-16, and local authorities evacuated residents. A M_b 4.7 regional earthquake occurred ~60 km southeast of Tungurahua at August 16 0516, and this may

have disrupted the volcano's plumbing system [*Barba et al.*, 2006]. Figure 4.10 shows the raw waveforms (a), spectrogram (b), and acoustic power and ash heights (c) for the eruption.

On August 16 1930 the acoustic signal emerges gradually, and its spectrum is concentrated below ~2 Hz. This continuous tremor-like activity was noted to produce a steam-rich and ash-poor plume by the IG observers [*Barba et al.*, 2006]. The first ash plume is observed in satellite imagery at 2015 at a height of ~6-7 km, and remains at this height until ~0215 on the 17th. Acoustic power between 1930-2200 is fairly steady between 0.2-0.87 MW. After 2200 the spectrum becomes more broadband and jet-like. The peak-to-peak amplitudes of the infrasound signal are continuous at ~2 Pa, with

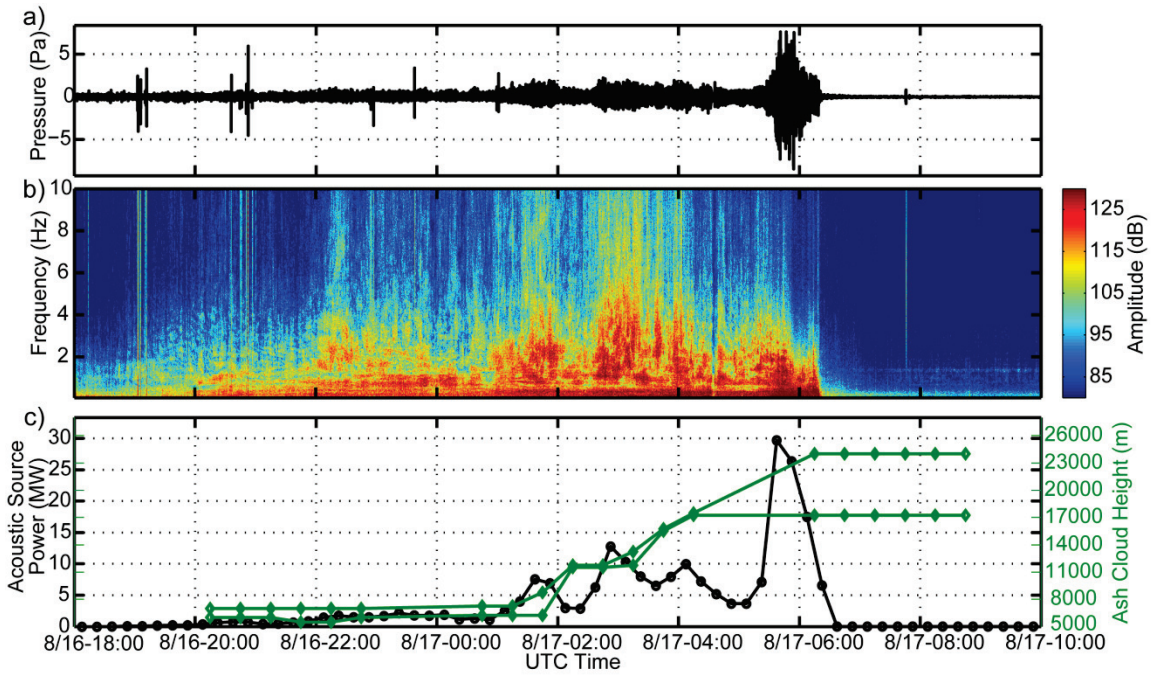

Figure 4.10 August 16, 2006 a) raw waveform, b) spectrogram, and c) acoustic power (black line) and ash cloud height (green). The paroxysmal Plinian phase of the eruption begins around August 17 0600 UTC, where the ash height goes up to ~26 km. The green lines represent the minimum and maximum estimated ash cloud heights.

power levels between ~1.1-2 MW. The IG reports the activity around 2200 resembles the onset of the July 14 eruption, with small PDCs, increased "roars" from the volcano, and a 100-200 m high lava fountain [*Barba et al.*, 2006].

The acoustic jetting decreases slightly between 0000-0100. At 0115 the plume is observed to increase in width, length, and intensity; coincident with a marked increase in acoustic power between 0100-0200 to 7.5 MW. Local reports indicated a lava fountain to 800 m above the vent and numerous pyroclastic flows during this period [*Barba et al.*, 2006]. The plume top is still roughly at the same height (7.25 km).

Between 0200-0230 the acoustic power decreases slightly, followed by a significant increase to 12.8 MW at 0300, the highest recorded power from Tungurahua at that point. Broadband jetting and some explosions are apparent, although the explosions are difficult to discern within the constant ~5 Pa peak-to-peak jetting. Note the noticeable notch in the infrasound spectrum between ~0.35-0.9 Hz typical of the jet noise at Tungurahua during the study period [*Matoza et al.*, 2009]. Incandescent blocks, the ash column, "roars", and explosions were reported in the nearby towns of Riobamba (31 km) and Ambato (32 km). The observed ashfall during this period was similar to that during the paroxysmal phase of the July 14 eruption and numerous PDCs were observed [*Barba et al.*, 2006]. The ash plume increases in length and width, and rises to a height of 13.25 km at 0315.

Between 0330-0430 elevated activity continues and acoustic power is between 7-10 MW. At 0415 a substantial increase in the lateral dimensions in the ash cloud is apparent, and the height is estimated up to 17.5 km. The acoustic power increases slightly at 0400, but the change is not substantial and the power is similar to levels observed earlier. Between 0400-0500 the lava fountain is observed to stabilize and rise to a height of ~1.5 km with continued PDCs [*Barba et al.*, 2006].

At August 17 0430 acoustic and eruptive activity declines substantially. An energetic Vulcanian explosion soon follows at 0436 UTC and signals the reactivation of the eruption. Intense acoustic activity continues for the next 1 hr (~3-7 MW), and both the power levels and spectrum are similar to those recorded earlier (broadband jetting, notch in the spectrum, etc). Unfortunately, there are no satellite observations of the ash plume during this period due to a satellite eclipse.

The paroxysmal phase of the eruption begins at ~0530 and continues until 0620. Acoustic power levels increase to their highest level (30 MW) and the jetting spectrum shifts to a lower frequency [*Garces et al.*, 2008; *Matoza et al.*, 2009] (Fig. 4.11). The dominant frequency of jetting is now below 0.1 Hz, and although the instrument response has been corrected it is not completely resolved by our sensors as it lies outside the passband. However, it is clear that there is a significant shift in the spectrum. The peak-to-peak amplitude is ~16 Pa (Fig. 4.10a), a remarkably energetic signal at 37 km from the source. At 0615, the first satellite image after the data gap reveals a large circular plume (156 x 134 km) has risen to ~24 km, indicative of a Plinian ash column penetrating the stratosphere. The lava fountain was observed to be an astounding 6 km above the vent at this time, and numerous PDCs and heavy local ashfall occurred. Over 40% of the IG

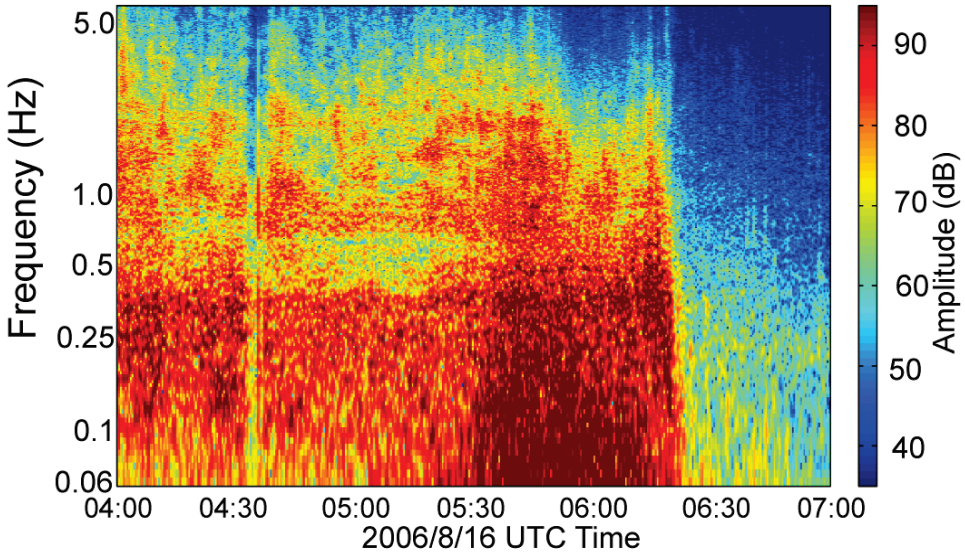

Figure 4.11 August 16, 2006 spectrogram between 0400-0700 UTC. The dominant frequency of the jetting shifts to a lower frequency after ~0530, coinciding with a Plinian ash column. The eruption ends at ~0620.

monitoring network was destroyed during this phase [*Barba et al.*, 2006]. After 0620 the infrasound power levels and eruptive activity drop off sharply to low levels. Remarkably, as after the July eruption, background 1.4 Hz tremor resumes at ~0730, seemingly unaffected by the cataclysmic eruption.

4.5.5 January 10-11, 2008

Intense Strombolian activity occurred between December 2007-early February 2008. We select January 10-11 as a case study due to the heightened activity typical of this period and relative lack of meteorological clouds necessary for identifying ash clouds. Figure 4.12 shows the raw waveforms (a), spectrogram (b), explosions, acoustic power and ash height (c) for January 10-11, 2008.

During these two days 428 Strombolian explosions are detected, and occur at a rate up to 32/hr. The detected explosions are indicated by the red dots on top of Fig. 4.12c. The explosions peak pressure ranged between ~0.06-2.91 Pa, with most of them

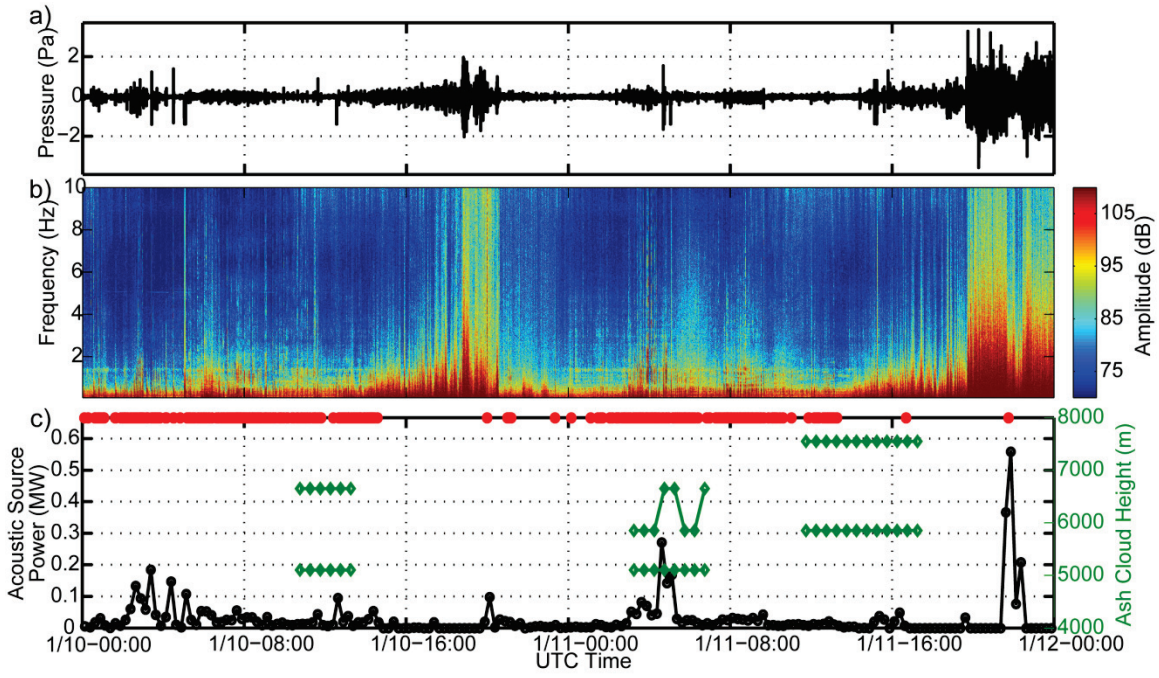

Figure 4.12 January 10-11, 2008 a) raw waveform, b) spectrogram, and c) acoustic power (black line) and detected explosions (red dots). Numerous Strombolian-type explosions were detected throughout these two days, but no significant ash plumes were detected. Wind noise dominates the spectrogram during ~1900-2300 UTC.

relatively small below ~0.35 Pa. Similarly, energy ratios range between 0.0012-3.32 with the mean at 0.06. The reduced number of detected explosions between ~1700-2200 on both days is due to the increased wind noise reducing the S/N and thus detection capability. No periods of energetic tremor or jetting occur during this period, although the background 1.4 Hz tremor was intermittently active. Despite the high number of explosions, only three low-level ash clouds were detected (Fig. 4.12c). The January 11 0315-0645 ash cloud is coincident with an increased rate of explosions and acoustic power. However, other periods of increased explosion energies and rates did not produce detectable ash clouds (e.g. January 10 0300-0600, January 11 2230). Similar to the May 2006 sequence, the explosions here are primarily gas rich and produce little ash. The IG reports incandescent blocks are again erupted by the more powerful explosions, but significant fragmentation and ash emissions does not occur. The amplitudes and energy of the explosions are smaller than the May sequence, although the rate and quantity are higher here.

4.5.6 February 6, 2008

After at least a month of escalating activity and numerous warning signs of an impending eruption, a Vulcanian-Subplinian eruption occurred at Tungurahua on February 6, 2008. This eruption was notable in that the autonomous ASHE monitoring and notification system was running and had been tuned using the July and August 2006 eruptions. Also noteworthy was the fact that rather than a sustained eruption for >4 hours (July and August 2006), the February 6, 2008 eruption had numerous pulses of activity over 10.5 hours, allowing easier correlations between changes in eruptive activity and its manifestations in the infrasound and satellite data. In the following detailed chronology of eruptive activity, we list selected detections and automatic notifications made by the ASHE project and split the eruption into four phases based on satellite and infrasound observations. Figure 4.13 shows the raw waveforms (a), spectrogram (b), and acoustic power and ash height (c). ASHE energy and explosion notifications are also indicated by red and brown lines, respectively, in Figure 4.13c.

The eruption began gradually on February 6. Numerous explosions occurred during the first part of the day, all of them with an energy ratio less than 1. This type of

activity is very similar to that of January 10-11, 2008 and the days preceding this eruption. At ~0300 acoustic tremor begins, and the spectrum resembles low-level jetting. At 0415 the jetting becomes more continuous and the power levels rise. Similar to that of the July 14, 2006 and August 17, 2006 eruptions, there is a notch in the jetting spectrum between ~0.35-0.9 Hz. Poorly constrained PDCs were also reported by the IG. The majority of the signal is concentrated between ~0.1-2 Hz. At 0430 the ASHE acoustic energy notification threshold of 1×10^8 J is exceeded. A notification of elevated acoustic energy is sent to the VAAC and IG at 0434 UTC. The notification latency includes ~4 minutes for the data to be recorded, sent to Canada via satellite, forwarded to Hawaii via internet, and processed by the autonomous ASHE algorithms. Adding the acoustic travel time of ~1.8 minutes, the notification was sent ~5.8 minutes from the actual time of

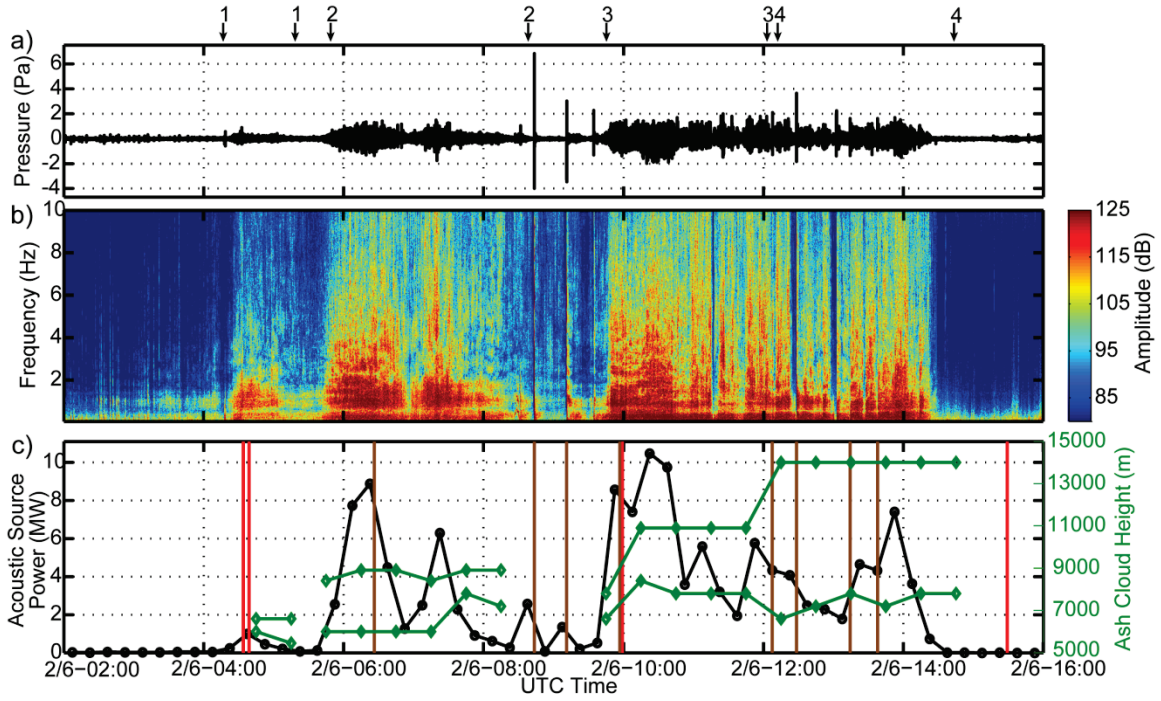

Figure 4.13 February 6, 2008 a) waveforms, b) spectrogram, and c) acoustic power (black line) and ash cloud height (green). Red lines in c) indicate the automatic ASHE acoustic energy notifications sent to the VAAC. Brown lines in c) denote ASHE explosion notifications. The ASHE system notified the onset, escalation, and cessation of the major eruption. Arrows above a) indicate four eruption pulses referred to in text.

volcanic activity onset at Tungurahua, which is close to the 5 minute latency goal of the ASHE project.

At 0435, the calculated acoustic energy for the past hour increases to 4.41×10^{8} J, and the 15 min power level is ~1 MW. Because the energy level has more than doubled, another email alert is sent out notifying of this change in eruptive activity. The first plume is observed in satellite imagery at 0445, and has a modest but still potentially hazardous height of ~6-7 km. The jetting decreases over time and lowers by 0515. This is coincident with the plume appearing detached from the summit in the 0515 satellite image. This sequence is referred to as phase 1.

After a decrease in the acoustic power, the energetic jetting returns around 0540, beginning phase 2. The jetting continues until 0655 and the maximum acoustic power is 1.27 MW. The jetting is more broadband in phase 2 than in phase 1, although both have the characteristic notch in their spectrum. The phase 2 plume is first imaged at 0545 at a height of 6-8.4 km, increasing in width and length until 0645. The plume's volumetric increase is consistent with the increased acoustic jetting during this period. A large explosion occurs at 0626 (E_r=13.83, P_p=3.85 Pa). This explosion surpasses the explosion energy threshold and causes an email notification. Although the jetting decreases temporarily between ~0655-0700, it returns between 0700-0830 until phase 2 ends. The spectral structure for this time period is different than earlier in phase 2, as the higher frequencies (>2 Hz) show more variability. Power levels peak around 6.3 MW. Although the timing is difficult to discern due to missing images, the plume has detached from the summit by 0915. The infrasound power levels drop sharply from 0745-0900, except for two large explosion recorded at 0843 (E_r=96.0, P_p=13.2 Pa) and 0911 (E_r=35.6, P_p=7.99 Pa). These explosions occurred during a quiescent period where only small tremor or jetting was occurring, and no significant discrete thermal plume was produced from the explosion. However, the large energy ratios (>5) triggered an explosion email notification. For the first time during this eruption, harmonics are present in the spectrum between ~0800-0815 in both the explosion signals, reminiscent of the May 12 explosions (Section 4.5.2).

Phase 3 begins with the most acoustically energetic portion of the eruption between 0945-1115. The infrasound signal is broadband, constant, has the typical jet

spectrum, and the peak power level is 10.5 MW. The 0945 GOES image shows a new plume up to 7 km attached to the summit which increases in width and height (10.9 km) until 1145. A 2 km high incandescent jet and numerous PDC are observed. Even though the last energy level notification was sent to the VAAC about 5.5 hours earlier (0439), the acoustic energy has stayed above the energy level of the previous notification for each 5 minute update. For this reason no updated notification was sent out. At 0955 the energy level more than doubles from its previous value to 4.69×10^9 J and a new automatic notification is sent.

Although the plume stays attached to the summit during the rest of the eruption, the jetting decreases abruptly at 1115 for the next ~5 minutes. Between 1120-1205 phase 3 continues with two somewhat less energetic jetting pulses. These pulses are still significant with power levels between 1.9-5.8 MW. The plume decreases in width and length during these jetting pulses but remains attached to the summit.

Phase 4 lies between 1215-1430 and consists of at least seven distinct jetting pulses. The duration and frequency content of the jetting pulses varies slightly from pulse to pulse, but each is fairly similar in that they are preceded by a short period of quiescence, followed by an explosion, and then the typical jet noise spectrum. Four of these explosions triggered an explosion notification email: 1207 (E_r=7.38, P_p=3.84 Pa), 1228 (E_r=30.94, P_p=8.76 Pa), 1314 (E_r=6.26, P_p=2.93 Pa), and 1337 (E_r=5.69, P_p=3.21 Pa). In total 43 explosions are clearly detected during phase 4. Infrasound power levels oscillate somewhat during this phase, reaching a peak of 7.4 MW between 1345-1400. Numerous PDCs occurred during this phase and tephra fall to 3 cm was reported [*Barba et al.*, 2006]. The plume appears attached to the summit during all of phase 4. However, the satellite image is cropped during this period and it is difficult to discern the maximum extent of plume. Further the sampling interval of the GOES data limits high temporal tracking of the plumes. Estimates from the VAAC put the top of the plume at 14 km during phase 4. The acoustic power tapers off after the last pulse and the volcano is quiet after 1430. After staying at an elevated level for ~10 hours, the volcano's hourly energy level has decreased and a notification to that effect is sent out at 1529. The DC VAAC cites decreased seismic and infrasound activity in their advisory at 1633 UTC.

4.6 Discussion

4.6.1 Constraining silicic eruptions using infrasound

Increases in acoustic power (a possible proxy for jetting intensity) during the major, sustained eruptions at Tungurahua between 2006-2008 are broadly consistent with increases in ash cloud height. Two exceptions are August 17, 2006 0300-0415 and July 15, 2006 0130-0300. Possible changes in the vent diameter, atmosphere, or multiphase eruptive mix may be responsible for these inconsistencies. Increases in acoustic power also correlate well with total ash cloud extent, which may not be as susceptible to the aforementioned factors. The acoustic power, onsets, and durations for the February 6, 2008 eruption correlate well with the observed ash plumes. Each of the 4 phases of ash emissions correspond with distinct acoustic phases (Fig. 4.12). Thus, in contrast to previous acoustic observations at Tungurahua [*Johnson et al.*, 2005], acoustic energy release during large sustained eruptions does appear to broadly scale with eruption intensity.

Ash emissions for all three major eruptions are coincident with the onset and cessation of infrasonic jet noise. For example, the jetting during the July 14 eruption (~4.75 hours, July 14 ~2245-July 15 0230) correlates well with the total duration and timing of the satellite-derived ash emissions (Fig. 8). Jet noise is attributed to small and large scale turbulence interactions within the momentum driven jet itself [*Tam*, 1998], with the infrasonic jet noise at Tungurahua most resembling large scale turbulence [*Matoza et al.*, 2009]. The relative acoustic power radiated is a function of the variations in velocity and volume flux of the ejecting gas-ash mixture. Following Lighthill's acoustic analogy [*Lighthill*, 1954], acoustic multipole radiation levels are predicted to follow velocity power laws [*Woulff and McGetchin*, 1975]. Although comparing acoustic power to jet velocity is an enticing subject [*Vergniolle and Caplan-Auerbach*, 2006; *Woulff and McGetchin*, 1975], the complex nature of multipole source radiation and propagation make this a challenging task [*Garces et al.*, in review].

Changes in the infrasonic frequency content are also likely indicators of changes in eruptive/jetting activity and are not as dependent on propagation and source directionality. Two prime examples are the paroxysmal Plinian phase of the August 17 eruption and the collapsing column at the end of the July 14 eruption (Section 4.6.3). The

addition of VLP energy on August 17 (Fig. 4.10,11) indicates a significantly large and energetic source, in this case a high velocity jet ejecting ash into the stratosphere [*Garces et al.*, 2008; *Matoza et al.*, 2009]. The peak acoustic power of ~30 MW underestimates the total acoustic power, as this calculation only considers frequencies above 0.1 Hz. To further illustrate the extent of low frequency energy, Figure 4.14 follows the aforementioned method of calculating acoustic power (Section 4.4) but divides the data into octave bands between 0.0625-16 Hz. The peak acoustic power of 17 MW in the 0.0626-0.125 octave band during the paroxysmal stage of the eruption August 17 is extraordinary, and could serve as a clear discriminator for stratospheric ash injection. Further, the total acoustic power is on the order of ~50 MW during this time period, a remarkable amount. As outlined in Section 4.4, this energy is underestimated by at least a factor of 2 for a subaerial jet source, so the total radiated acoustic power in the 0.06-16 Hz band may be closer to ~0.1 GW near the source.

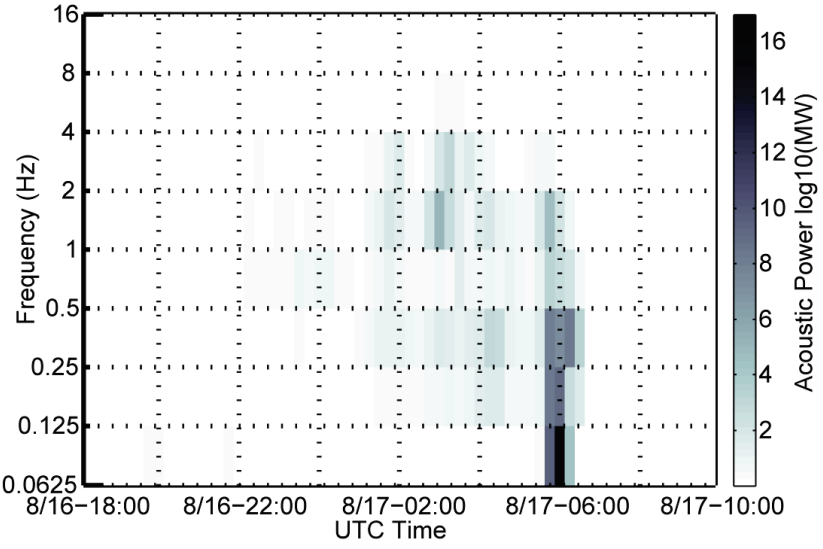

Figure 4.14 Acoustic energy for the August 16, 2006 eruption. The acoustic energy was calculated in hour-long octave bands. The Plinian phase of the eruption is characterized by a significant amount of low frequency (<.5 Hz) energy. Approximately 17 MW of power is detected in the 0.0626-0.125 octave band.

4.6.2 Generation of thermals

During the course of this experiment, large explosions were not indicative of significant ash emissions. No distinct thermals were detected in the satellite imagery or eye-witness observations from any of the May 12, 2006 explosions (Fig. 4.5). The Vulcanian explosions on February 6, 2008 were also not associated with distinct thermals, rather the sustained periods of jetting on this day were found to produce more significant ash (Fig. 4.13). The numerous Strombolian explosions from December 2007-February 2008 also only produced small to negligible ash clouds (Fig. 4.12). These assertions are broadly consistent with ground and satellite observations during other periods of the experiment as well. During the course of the experiment numerous explosion notifications were sent to the VAAC, but no clear correlation was found between energetic explosions and ash-laden thermals.

Of particular interest are the explosions that precede jetting and/or large eruptions. The July 14, 2006 2234 explosion signals the onset of jetting and ash emissions. The waveform and spectral features of this explosion are not significantly different than other explosions. The amplitude and energy are above average, but not extraordinary. The explosion preceding the jetting periods for the February 6, 2008 eruption have complicated waveforms, which could be due to complex source or propagation effects. The explosion at August 17 2006 0436 also preceded jetting, but was not substantially different from other explosions during the experiment.

In order to transport ash to a significant altitude, sufficient momentum and then buoyancy must be imparted into the flow. Peak infrasonic amplitudes for explosions are related to the maximum overpressure, which occurs over a very short time period (<1 s). Longer duration momentum transfer (tremor and jetting) appears to be more conducive to significant ash injection. Multiple closely spaced explosions would put more energy into the system and increases the likelihood of a significant thermal [*Sparks et al.*, 1997; *Wilson et al.*, 1978]. Although infrasound generating explosions at other volcanoes have produced significant thermals [e.g. *Petersen et al.*, 2006; *Vergniolle and Caplan-Auerbach*, 2006], those at Tungurahua between 2006-2008 are possibly more gas-rich and ash-poor. Another consideration for the smaller impulsive events is atmospheric stability, which could either suppress or encourage plume rise. The larger eruption

dynamics appear to be less vulnerable to local weather conditions due to their higher volume, momentum, and temperatures, which may overwhelm the ambient atmospheric state.

4.6.3 PDC generation

Volcanic column collapse occurs when the eruption column does not sufficiently entrain enough air to rise buoyantly. An increase in the degree of fragmentation or lithic material during an eruption would decrease the plume temperature and result in an increase in the time needed to transfer kinetic to thermal energy between the cooler particles and the hotter gas phase [*Wilson et al.*, 1978; *Woods*, 1995], decreasing air entrainment. As an eruption progresses, erosion and widening of the conduit and crater would add lithics to the plume [*Sparks et al.*, 1997; *Woods*, 1995]. The 2006 Tungurahua eruptions significantly eroded and widened the crater to 300-400 m (Fig. 4.1b) and presumably the conduit as well. Further, widening of the conduit decreases the jet's ability to entrain enough air to rise buoyantly, thereby increasing the likelihood of column collapse [*Sparks et al.*, 1997]. In February 2008, Tungurahua's conduit was likely wider than in 2006, thereby making it more difficult to sustain a Plinian column, decreasing the ash heights, and increasing the likelihood of column collapse. This is consistent with the shorter duration of eruption pulses in the infrasound and satellite observations (Fig. 4.13).

Overpressured jets may also create annular flow in plumes and periodic column collapse without a change in the source conditions [*Ogden et al.*, 2008]. Higher vent overpressure on February 6, 2008 could have caused the intermittent column collapse and PDC generation (Fig. 4.13). Shock cells from overpressured jets could theoretically create broadband shock noise and screech tones [*Tam*, 1998] that could be recorded by our arrays. Some of the unexplained spectral structure above the 0.25 and 1 Hz peaks in the jet structure (Fig. 4.13) during the February eruption could be attributed to broadband shock noise, but the sharp spectral peaks from screech tones often produced by man-made, highly symmetric jets are not visible or likely.

4.6.4 Acoustics of sustained vs. collapsing columns

Jet noise at Tungurahua is thought to be produced by a combination of factors. Matoza et. al [2009] postulated that large scale turbulence (LST) interactions within the jet is a likely source due to the similarity of the Tungurahua jetting spectra with those established in controlled, man-made jets [*Tam et al.*, 1996]. The generally accepted model of LST noise generation consists of large turbulence structures (greater than the jet diameter) propagating as supersonic instability waves along the jet shear layer. The turbulence structures act similar to a "wavy-wall" radiating mach waves downstream [*Tam*, 1998]. Note this mechanism requires a well-developed flow extending above the jet nozzle.

To better estimate the variability of the jet spectrum at Tungurahua, probability density functions (PDF) of the power spectral density estimates of jet noise are constructed in a manner similar to McNamara and Buland [2004]. The PSD PDFs (Fig. 4.15) are constructed using beamformed five minute time windows of the RIOE data during the time periods encompassing the jetting during the case studies: July 14, 2006 2245-0245, August 16, 2006 2200-August 17, 2006 0630, and February 6, 2008 0415-1430 (Fig. 4.15a,b,c). The peak probability during the sequences is highlighted by the white dotted line. For comparison, a typical PSD of the Tungurahua background noise (July 29, 2006 0800-0900) is shown (Fig. 4.15a), including the typical 1.4 Hz tremor, as well as a typical spectrum from the Plinian portion of the August 16-17 eruption (Fig. 4.15b, black line). All three eruptions share similar characteristics, although the August and February jetting show higher variability. The typical jet spectrum at Tungurahua has two broad peaks at ~0.25 and ~1 Hz, with a notch in between (Fig. 9,15). The two spectral peaks at 0.25 and 1 Hz are clear for the July 2006 and Feb. 2008 eruption, but not as much for August 2006. Both spectral peaks are also apparent at the LITE array, suggesting neither is due to propagation effects. The jetting signals at RIOE vary from ~10-40 dB above the background noise, depending on the frequency.

The paroxysmal phase of the July 14, 2006 eruption allows a closer inspection of the jet noise sources. Although the exact sources are unresolved due to the complex nature of multiphase volcanic jets and recording limitations, the ~0.4-0.6 Hz notch in the jetting spectrum may be the result of gas-particle interactions not tested in typical

laboratory experiments or simply the space between two separate noise sources with jet-related signatures [*Matoza et al.*, 2009]. The spectrum after the column collapses (after July 15 ~0245) shows only a single peaked spectrum centered at ~0.25 Hz that fits the large scale turbulence (LST) similarity spectrum quite well (Fig. 9). Unlike the jetting signals studied by Matoza et al. [2009] and represented in Fig. 4.15, during the selected time window there is no sustained ash column, but rather a negatively buoyant mixture feeding numerous PDCs. The "wavy-wall" analogy extending above the vent for LST does not seem to be present for this period, unless a purely gaseous jet has decoupled

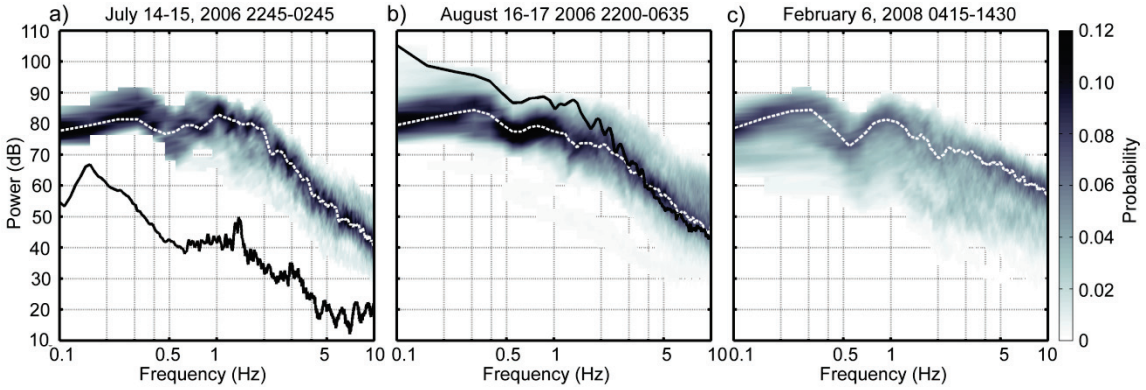

Figure 4.15 Power spectral density probability density functions comparison for the three largest eruptions. Five minute long spectra are calculated and shown for a) July 14, 2006 2245-0245 UTC (4 hr), b) August 16, 2006 2200-0630 UTC (8.5 hr), and c) February 6, 2008 0415-1430 UTC (10.25 hr). White lines indicate the peak probability. The black line in a) is typical of the background tremor at Tungurahua and is selected from July 29, 2006 0800-0900 UTC. All three eruptions have fairly typical broadband spectra with two spectral peaks at ~0.25 and 1 Hz and are well above the background noise at all frequencies. The black line in b) shows the spectrum between August 17, 2006 0545-0550 UTC, typical of the Plinian phase of the eruption. Note the Plinian spectrum has much lower frequency energy. The sensor response begins to roll-off below 0.1 Hz.

from the particle laden PDC. However, a gaseous jet above the vent would likely be visible in the FLIR imagery. Because the single 0.25 Hz peak is still present during this period, different physical processes are likely responsible for the peaks in the typical Tungurahua jet spectrum. The higher frequency (~1 Hz) peak may thus be associated with a well-developed jet (e.g. LST from a wavy-wall), while the 0.25 Hz peak may be due to a different source. The PDC itself is a turbulent noise source [*Ripepe et al.*, 2009; *Yamasato*, 1997], but is unlikely due to the persistence of the spectral peaks throughout the three large eruptions (Fig. 4.15) and the fact that PDCs were not generated during the entirety of jet noise recording.

Most jet noise models are concerned with turbulence interactions downstream of the nozzle. Turbulence is a relatively inefficient noise producer due to its quadrupole radiation [*Lighthill*, 1954], but interactions of flow with solid surfaces can produce more efficient noise [*Howe*, 1998]. The addition of solid surfaces interacting with the flow can substantially affect the noise produced by 1) promoting the conversion of flow energy to acoustic energy, 2) introducing reverberation effects that can feed back to the flow, and 3) creating sound-generating flow features such as vortex shedding and edge tones [*Wang*, 2005]. The substantial broadband noise peak at 0.25 Hz produced during the entirety of the three large eruptions of 2006-2008 and documented during the generation of a large PDC on July 15, 2006, requires a continuous broadband acoustic source. One possibility for the 0.25 Hz spectral peak may be turbulent interactions of the flow with surrounding crater walls [*Matoza et al.*, 2009; *Woulff and McGetchin*, 1975]. The deep, heavily eroded summit crater at Tungurahua extends at least 100 m down from the crater rim, and is ~300-400 m wide (Fig. 4.1b). Jets emanating from volcanic conduits with pressure greater than atmospheric will decompress rapidly and interact with volcanic crater walls. The crater can both increase the jet velocity by providing additional upward thrust and affect the stability of the column [*Woods and Bower*, 1995]. Jet interactions with the crater walls at Tungurahua are hypothesized as a possible source mechanism for the relatively steady 0.25 Hz infrasonic peak.

4.7. Conclusions

Two infrasound arrays deployed in Ecuador provide a continuous record of the activity at Tungurahua Volcano between 2006-2008. A system was set up to automatically detect significant volcanic activity and notify the VAAC of a possible aviation hazard. After two large eruptions in 2006 were used to refine the automated ASHE algorithms, the onset of the Subplinian February. 6, 2008 eruption was detected and a notification was sent ~5.8 minutes after the acoustic onset. Acoustic energy from sustained, energetic eruptive activity at Tungurahua broadly scales with ash height and has a characteristic spectrum resembling a low frequency form of jet noise. During the paroxysmal Plinian phase of the August 2006 eruption, the jet noise spectrum clearly shifts to low frequencies (below 0.1 Hz) and produces over 50 MW (5×10^7 Watts) of acoustic power. These high power levels suggest not only that the acoustic contribution to the total energy budget is not negligible, but that the acoustic efficiency of volcanic processes may be higher than anticipated. Numerous short duration Strombolian and Vulcanian explosions were primarily gas-rich and did not produce significant ash clouds. A collapsed volcanic column during the July 2006 eruption has a unique infrasonic spectrum and may suggest a relationship between jet noise and column buoyancy. The interaction of the high velocity, unsteady, energetic jet with the crater walls is hypothesized as a potential source mechanism for low-frequency sound production and spectral modulation.

The ASHE proof-of-concept project has demonstrated that acoustic array monitoring of large volcanic eruptions at regional distances is not only viable, but sufficiently mature to transition into operational volcano monitoring. In conjunction with other technologies such as remote sensing, infrasound can assist in providing low-latency notification of increased volcanic unrest and ash emissions, particularly for large eruptions. Further, it provides a remote sensing tool to study the dynamics of a variety of eruption styles. In order to validate and test the results presented here, the ASHE project is being extended to the global infrasound network of the International Monitoring System (IMS). In ongoing follow-up work, we are focusing on Subplinian to Plinian eruptions of the past decade consistently recorded by multiple IMS arrays.

Acknowledgements

A version of this chapter has been published as: Fee, D., M. Garces, and A. Steffke (2010), Infrasound from Tungurahua Volcano 2006–2008: Strombolian to Plinian eruptive activity, *Journal of Volcanology and Geothermal Research*, *193*, 67-81. The authors are grateful to the entire ASHE team for making this work possible, with special thanks to the Geological Survey of Canada for their technical and logistical support and to the dedicated staff of the Instituto Geofisico for their persistent and invaluable monitoring of Tungurahua. Patricio Ramon at the IG was exceptionally helpful in the preparation of this manuscript. Rene Servranckx at the Montreal VAAC and the helpful staff of the Washington DC VAAC provided invaluable feedback and assistance. Countless discussions with Robin Matoza help improve this work immensely. Sara McNamara helped with some of the ASHE algorithm development. Doug Drob graciously provided the atmospheric models. Helpful comments from two anonymous reviewers greatly improved the manuscript. This work was made possible by the National Oceanic and Atmospheric Administration through University of Mississippi subcontract 09-09022.

CHAPTER 5: CHARACTERIZATION OF THE 2008 KASATOCHI AND OKMOK ERUPTIONS USING REMOTE INFRASOUND ARRAYS

Abstract

The 2008 Plinian eruptions of Kasatochi and Okmok Volcanoes were recorded by six remote International Monitoring System (IMS) infrasound arrays. High amplitude infrasound at these stations, combined with remote sensing, permits insight into important volcanic source parameters, such as origin times, durations, and source characteristics. Infrasound from the August 7-8 Kasatochi eruption consists of three well-defined eruption pulses, with the first two steam-rich and the last ash-rich. Pulse 2 is the most energetic and impulsive. Okmok produced over nine hours of continuous infrasound on July 12-13. Acoustic propagation modeling for the Okmok eruption and first Kasatochi pulse predict thermospheric ducting and origin times consistent with seismic and satellite observations. However, theoretical acoustic origin times of Pulses 2-3 are predicted to occur ~15 minutes earlier than the seismic. Stratospheric ducting for these later pulses provide more consistent origin times. Although both volcanoes ejected ash into the stratosphere (>15 km), Kasatochi produced higher amplitude infrasound than Okmok. Previous studies have shown sustained infrasound with frequencies <0.5 Hz is indicative of high-altitude ash emissions. Kasatochi and Okmok recordings are consistent with this, as stratospheric emissions evident in satellite imagery are correlated with sustained 0.01-0.5 Hz infrasound. Further, the acoustic spectrum shape resembles the spectrum from man-made jets, suggesting a self-similar noise generation mechanism proposed in earlier work. Although uncertainties exist, observations and propagation modeling from Kasatochi suggest self-similarity is apparent at long distances (>2000 km) and does not seem to be appreciably affected by changes in ash content between the eruption pulses.

5.1. Introduction

Acoustic recordings of volcanic eruptions have proven effective at monitoring and characterizing a wide-variety of eruptive styles [e.g. *Garces et al.*, 2008; *Ripepe et al.*, 2009]. Low frequency acoustic waves (infrasound, with frequencies <20 Hz) are able to propagate long distances with little attenuation [*Sutherland and Bass*, 2004]. Previous work has focused on a broad range of topics and eruptive styles, although most have been concerned with local (<10 km) and regional (<250 km) deployments. Long range (telesonic, >250 km) detection of volcanic eruptions was previously limited to low signal-to-noise statistical studies [e.g. *Le Pichon et al.*, 2005] and low resolution barograph recordings of large eruptions [e.g. *Goerke et al.*, 1965; *Tahira et al.*, 1996]. Advances in networks, sensor technology, and propagation modeling now permit detailed studies of remote volcanic eruptions using infrasound arrays. The Acoustic Surveillance for Hazardous Eruptions (ASHE) project seeks to take advantage of the global coverage and state-of-the-art technology of the International Monitoring System (IMS) of the Comprehensive Nuclear-Test-Ban Treaty to expand high-resolution acoustic studies of volcanoes to telesonic distances. Remote acoustic surveillance of volcanoes may help provide important and timely (<2 hours) source parameters for hazardous eruptions.

The 2008 eruptions of Kasatochi and Okmok volcanoes provided an opportunity to test the viability of the IMS infrasound network for monitoring and characterizing large eruptions. Both eruptions were relatively unexpected due to the lack of recent activity at Kasatochi and the short duration of precursory activity at Okmok. The emissions from these remote eruptions reached the stratosphere and disrupted air travel in the north Pacific for several days. Both eruptions also interacted with nearby water, and the high steam content in much of the emissions makes it difficult for traditional remote sensing techniques to detect ash [*Prata*, 2009], the primary volcanic threat to aviation. Multiple IMS arrays detected significant acoustic signals below 0.5 Hz from both eruptions. Sustained acoustic signals in this band have been found to indicate significant atmospheric ash emissions [*Fee et al.*, 2010; *Garces et al.*, 2008; *Steffke et al.*, 2010].

Further, recent studies at Tungurahua Volcano, Ecuador and Mount St. Helens, USA have shown that sustained infrasound from large eruptions resembles a low frequency form of jet noise [*Fee et al.*, 2010; *Matoza et al.*, 2009]. Turbulence structures

within the gas-thrust (jet) region of the eruption column, as well as possible jet-crater interactions, are candidate sources for the high-amplitude, long-duration jetting signals. A proper understanding of jet noise sources may one day allow detailed characterization of the gas-thrust and buoyant plume region using remote acoustic surveillance. However, many questions on the source mechanisms, characteristics, and applicability of turbulence related noise to other volcanoes remain.

This paper aims to use the Plinian eruptions of Okmok and Kasatochi Volcanoes in July and August 2008 to: 1) assess the feasibility of acoustic monitoring and characterization of large volcanic eruptions at telesonic distances, 2) examine whether jet noise features are still apparent at these distances, 3) use these eruptions to expand our knowledge of acoustics from large eruptions. In order for these aims to be met, a proper understanding of the atmosphere and long-range propagation is needed. The validity of current propagation methods and models are thus also evaluated. This paper combines remote sensing and infrasound recordings in a manner similar to *Fee et al.* [2010] and *Steffke et al.* [2010]. A separate paper in this issue [*Arnoult et al.*, in review] focuses on eruption infrasound signal detection and location, while this paper concentrates on characterizing the eruptions and defining their source parameters.

5.2. Volcanic Background

5.2.1 Okmok Volcano

Okmok volcano (53.43°N, -168.13°E), located along the eastern end of the Aleutian Islands (Fig. 5.1), is an expansive basaltic shield volcano. Recent eruptions have emanated from cinder cones within the two overlapping ~10 km wide calderas [*Smithsonian*, 2008a] and produced ash clouds to ~5-6 km above sea level (ASL) [*Larsen et al.*, 2009]. On July 12, 2008, the largest eruption of Okmok in the past century began from a cinder cone within the caldera. The unanticipated eruption was preceded by only ~5 hours of precursory seismicity and no discernible deformation. Continuous seismic tremor began at ~1943 UTC and increased rapidly at 1948, peaking at 2200 and lasting for almost 12 hours [*McNutt et al.*, 2008]. The abundant groundwater and lake near Cone

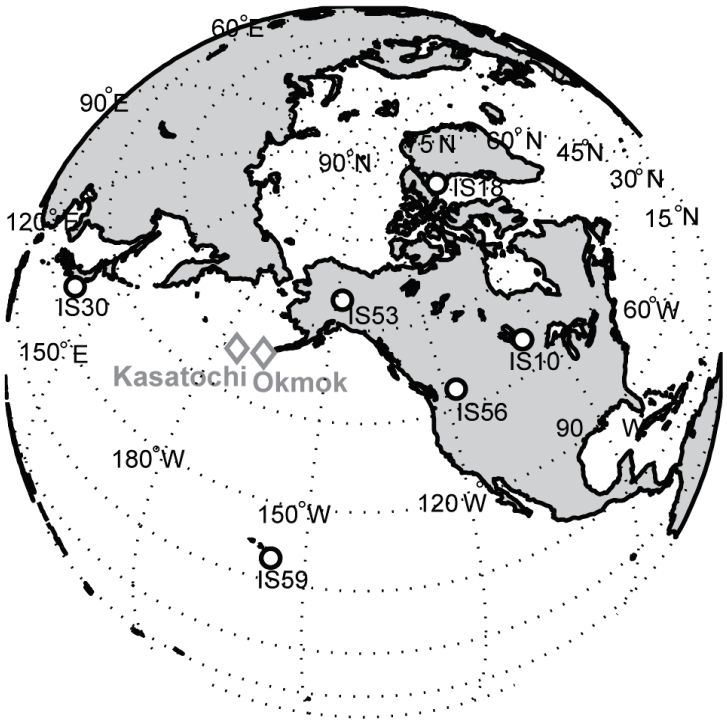

Figure 5.1 Overview Map. IMS arrays that detected at least one of the eruptions are denoted as black circles. IS53, IS59, and IS18 recorded the signal with the highest S/N. Kasatochi and Okmok Volcanoes are gray diamonds.

D interacted with the magma to produce a sustained phreatomagmatic eruption that ejected an ash cloud to ~16 km, entering well into the stratosphere and disrupting air traffic in the region for days. The high water content of the eruption plume made it difficult to discern the ash content. Ash and gas emissions continued for the next ~5 weeks after the powerful VEI 4 eruption [*Larsen et al.*, 2009]. SO_2 monitoring instruments detected ~0.1 Tg from the Okmok eruption [*Prata et al.*, submitted]. This sequence is notable as it was a rare basaltic phreatoplinian eruption.

5.2.2 Kasatochi Volcano

Kasatochi is a small (~3 km diameter), remote volcanic island in the central Aleutian Islands (Fig. 5.1) with sparse eruptive activity before 2008. Rising to only 314 m ASL, the volcano has a ~0.75 km diameter crater lake and a lava dome [*Smithsonian*,

2008b]. On August 7, 2008 a VEI 4 eruption occurred at Kasatochi with little to no warning. The nearest seismometer was on Great Sitkin Island ~40 km away, and provided poor detection and location of precursory seismicity from Kasatochi. Three main eruption pulses occurred, with seismically inferred origin times of August 7 2201, August 8 0150, and August 8 0435 UTC. The first two pulses appear to be ash-poor and steam-rich, while the third has a higher ash concentration (Section 5.5.3). The high levels of steam are likely due to the eruption passing through the crater lake. All three pulses ejected ash into the stratosphere and caused widespread aircraft delays and cancellations. Lower level, sustained activity began after the third pulse and continued for almost 14 hours. Significant pyroclastic density currents (PDCs) likely occurred during all three eruption pulses and extended the shoreline in some places up to 300 m [*Waythomas et al.*, 2008]. The eruption emitted a substantial amount of SO_2 into the atmosphere (~1.7 Tg) [*Corradini et al.*, 2010], the highest measured amount since the eruption of Hudson volcano in 1991.

5.3. Data and Methods

5.3.1 Infrasound Data

IMS infrasound array data within ~5000 km of Kasatochi and Okmok volcanoes (Fig. 5.1) were compiled. Tables 1 and 2 list the array data selected for the Kasatochi and Okmok eruptions, respectively, and the azimuth, distance, and modeled travel time to the volcano. Section 5.3.4 describes the propagation modeling and acoustic travel time calculations. IS53 (Fairbanks, Alaska), IS18 (Qaanaaq, Greenland), and IS59 (Kona, Hawaii) (Fig. 5.1) recorded the August 7-8 Kasatochi eruption with the highest signal-to-noise ratio (S/N) and will be the focus of this paper. IS30 (Tsukuba, Japan), IS56 (Newport, Washington), and IS10 (Lac du Bonnet, Canada) also clearly recorded the eruption. The July 12-13 Okmok eruption is detected at IS53, IS30, and IS59, with possible (but minor) detections at IS18 and IS56. IS53 consists of an eight-element array, with the sensor configuration consisting of an inner triangle surrounded by an outer pentagon. The array aperture is ~2 km. IS18 is an eight-element, ~1.2 km aperture array consisting of four inner elements in quadrilateral arrangement, enclosed by four elements in a centered triangle. IS59 is a four element centered triangle array with an aperture of

Table 5.1. List of IMS array that recorded the Kasatochi eruption. Kasatochi is located at 52.177° N, -175.508 W. Azimuth is the bearing from the station to the volcano, in degrees from north. Travel time is the predicted time for an acoustic ray to travel from the volcano to the station using ray tracing. Modeled celerity is the distance from the volcano to the station divided by the predicted travel time. IS53, IS59, and IS18 have the highest S/N and are discussed in more detail in this paper.

Station	Lat	Lon	Azimuth (°N)	Range (km)	Travel Time (s)	Modeled Celerity (km/s)	S/N
IS53	64.875	-147.861	241	2103	7,965.6	0.264	High
IS30	35.308	140.314	48	3926	13,211.5	0.297	Low
IS59	19.592	-155.894	340	3996	15,994.8	0.250	High
IS56	48.264	-117.126	299	4056	16,163.9	0.251	Low
IS18	77.476	-69.288	299	4746	17,062.2	0.278	High
IS10	50.201	-96.027	305	5247	20,072.8	0.262	Low

Table 5.2. List of IMS array that recorded the Okmok eruption. Okmok is located at 53.397° N, -168.166 W. Remarks on array processing detections are listed as well.

Station	Lat.	Lon.	Azimuth (°N)	Range (km)	Travel Time (s)	Modeled Celerity (km/s)	Detection Band Remarks
IS53	64.875	-147.861	231.4	1706	6,966	0.245	IVLP-yes MB-yes
IS56	48.264	-117.126	298.8	3548	14,222	0.250	IVLP-no MB-possible
IS59	19.592	-155.894	347.3	3903	14,990	0.260	IVLP-yes MB-yes
IS30	35.308	140.314	46.7	4439	15,141	0.293	IVLP-yes MB-yes
IS18	77.476	-69.288	294.1	4464	17,392	0.257	IVLP-no MB-possible

~1.9 km. Chaparral Physics Model 5 microphones are used at IS53 and IS59 and have a flat passband between 0.02-50 Hz. IS18 utilizes DASE/Tekelec MB2000 microbarometers (flat response 0.01–27 Hz). Unless otherwise noted, volcanic signals at the other arrays exhibit similar features to IS53. All times are in UTC.

5.3.2 Satellite Imagery Processing and Analysis

Visible (VIS) and thermal infrared (TIR) Geostationary Operational Environmental Satellite (GOES) and Moderate Resolution Imaging Spectroradiometer (MODIS) satellite data were processed and analyzed to develop eruption chronologies, determine eruption dynamics, and estimated ash plume ceilings. Because the GOES satellite is located at a high altitude (35,786 km) it is able to acquire images at a high temporal resolution by sweeping the entire earth disk at a high temporal frequency, thus trading spatial resolution for field of view and temporal resolution. The sensor acquires images of North America once every 30 minutes and collects data in five spectral bands. For this study GOES visible Band 1 (0.6 μm) and thermal infrared Band 4 (10.7 μm) are used with spatial resolutions of ~4.0 and 8.0 km^2 respectively at polar latitudes. The MODIS sensor is flown on NASA's polar orbiting satellites Aqua and Terra and therefore collects data at a lower temporal resolution. Each satellite makes equatorial crossings twice daily limiting the number of observations to approximately two images per sensor, providing an optimal total of four images per day for plume monitoring. The MODIS sensors collect data in 36 spectral bands, but only five are used to identify volcanic plumes in this study: bands 1 (0.62 – 0.67 μm), 3 (0.459 – 0.479 μm), and 4 (0.545 – 0.565 μm) and TIR bands 31 (10.78 – 11.28 μm) and 32 (11.77 – 12.27 μm). Bands 1 and 2 have a spatial resolution of 0.25 km^2 at nadir, while bands 3 and 4 have a spatial resolution of 0.5 km^2 at nadir. The TIR bands have a spatial resolution of 1 km^2 at nadir. GOES data is made available from the Naval Research Laboratory and MODIS data is acquired from NASA's Level 1 and Atmosphere Archive and Distribution System. The satellite data is used to calculate plume top temperatures and dispersal velocities [*Sparks et al.*, 1997]. These values are then compared to radiosonde and NRL-G2S atmospheric temperature profiles and wind fields [*Drob et al.*, 2003] to determine the maximum volcanic plume height [*Steffke et al.*, 2010].

5.3.3 Infrasound Data Processing and Detection

Three frequency bands are selected for infrasound processing: 0.01-0.1 Hz (Infrasonic Very Long Period, IVLP), 0.1-0.5 Hz (microbarom, MB), and 0.5-6 Hz (short period, SP). These bands resemble traditional volcano seismology frequency band designations [*Chouet*, 1996]. The MB band is selected, rather than Long Period (LP), due to the ubiquitous microbarom infrasound signal recorded at telesonic distances. Due to greater absorption at high frequencies, little SP energy is expected at these distances. Time-delay beamforming [e.g. *DeFatta et al.*, 1998] is performed for all the waveform and spectral calculations to increase the S/N. For large arrays with numerous sensors (such as those selected here from the IMS), beamforming reduces uncorrelated noise significantly.

A thorough detection and identification process is necessary because the primary frequency band of interest for large volcanic eruption (<0.5 Hz) is where wind noise power is significant [*Fee and Garces*, 2007]. Volcano infrasound detection methods here follow those of *Fee et al.* [2010], with an emphasis on detection of continuous jetting signals. This process is necessary to distinguish between signal of interest, unwanted signal (clutter), and noise. The Progressive Multi-Channel Correlation (PMCC) method [*Cansi*, 1995] is run in each one of these bands to detect coherent acoustic signals. IVLP processing consists of 250 s time windows with 80% overlap between windows and 10 frequency bands. MB processing consists of 90 second windows with 78% overlap and 10 frequency bands. Each time window is then examined to determine if coherent acoustic energy is present and originates from an azimuth within ±7° of the respective volcano, approximately twice the average standard deviation of the detection azimuth. If the window has greater than 5 detections with a mean cross-correlation value greater than 0.5, it is considered signal from the volcano and the root mean square (RMS) pressure is calculated for the entire window. RMS pressure displays the magnitude of the acoustic signal in each window. Acoustic energy is not presented for these eruptions, as the long propagation distances make the assumptions necessary in the calculation invalid. All spectral amplitudes are listed in dB relative to $(20\times10^{-6}\ \text{Pa})^2/\text{Hz}$.

5.3.4. Propagation Modeling

Acoustic ducting occurs when the upward propagating acoustic waves are refracted back down to the earth at the point where the effective sound speed exceeds that at the source. The sound speed can be defined as a function of temperature, *T*, by [*Pierce*, 1981]:

$$c = \sqrt{\frac{\gamma RT}{M}} \qquad (5.2)$$

where γ is t ratio of specific heats, *R* is the gas constant for air, and *M* is the molar mass. However, Eq. (5.2) is only valid when the medium is relatively static. High winds in the atmosphere can represent significant fractions of the sound speed (e.g. 1/3) and thus must be considered. The effective sound speed, c_{eff}, can be determined by adding the vector wind component, *u*, along the direction of propagation to the static sound speed *c*:

$$c_{eff} = c + \boldsymbol{u} \cdot \boldsymbol{n} \qquad (5.3)$$

Two atmospheric phenomena are primarily responsible for long-range ducting: 1) high wind speeds in the middle and upper atmosphere (commonly a significant fraction of the sound speed) and 2) sharp velocity gradients with length scales comparable to the acoustic wavelength.

Accurate acoustic propagation modeling requires a proper characterization of the atmosphere. Atmospheric variables are estimated using the NRL-G2S models [*Drob et al.*, 2003], providing temperature, wind velocity, and air composition. The NRL-G2S models provide the most up-to-date estimates of these parameters up to 140 km.

Two complimentary models are utilized to constrain the propagation of acoustic waves from Kasatochi and Okmok: ray tracing and parabolic equation (PE). These models are applied using the InfraMAP software program, developed and maintained by BBN Technologies [*Gibson and Norris*, 2002]. Here we use the 3-D Hamiltonian Ray

Tracing Program for Acoustic Waves in the Atmosphere (HARPA), modified from [*Jones et al.*, 1986]. HARPA uses ray theory to represent propagating acoustic energy through ray paths by applying a geometric, high frequency approximation to the acoustic wave equation. It is useful for calculating travel times and visualizing propagation in a refractive environment [*Brown and Garces*, 2008]. This model accounts for 3-D refraction, attenuation, absorption, and horizontal translation of the ray path from wind. However, ray path modeling does not account for scattering and diffraction [*Whitaker and Norris*, 2008], and thus can lead to unrealistic propagation estimates. Approximate travel times reported here incorporate InfraMAP's eigenray solutions that determine matching ray paths that propagate to the receiver within a given distance and height tolerance (2 km). Ray paths that are not projected to reach the receiver are not shown. Note the travel time used in this study assumes 1) the propagation paths are modeled correctly and 2) the first observed arrival is associated with the first modeled arrival. Although these two assumptions are at times not met, it provides a first-order estimate of the travel times.

PE models offer a continuous wave solution at a single frequency, outputting the transmission loss for a given vertical slice of the atmosphere. Diffraction is accounted for, which is important for shadow zones between predicted eigenrays, near the surface, and long wavelength (infrasonic) propagation. It is important to note that the PE has inherent phase errors above ~35° elevation from the source, so acoustic transmission loss at high launch angles is not as well constrained [*Whitaker and Norris*, 2008]. The combination of PE and ray theory used here provides estimates of travel times, propagation paths, and transmission loss for remote sources. Since the PE predicts transmission loss at a single frequency, we run PE simulations at multiple frequencies over the band of interest (0.01-1 Hz) in hope of applying the transmission loss to the recorded spectrum to estimate the source spectrum. This is an estimate of the atmospheric transfer function from source to receiver. All PE transmission losses are quoted in dB relative to the source at 1 m.

5.4. Jet Noise

Recent work has postulated that the momentum driven (gas thrust) portion of Subplinian-Plinian eruptions produce a low frequency form of jet noise [*Fee et al.*, 2010; *Matoza et al.*, 2009]. Man-made noise from jet engines (jet noise) has been studied extensively, and there is wide agreement that the dominant noise source is related to turbulence structures within the jet [*Tam et al.*, 2008]. Experimental jet noise studies have shown that two characteristic spectra are produced. *Tam et al.* [1996] present two empirically derived similarity spectra to fit the experimental studies. Researchers further postulate that since two characteristic spectra are produced from jets regardless of jet Mach number or temperature, there are two dominant jet noise sources. The first is related to small-scale turbulence (SST) structures within the jet which are dominant in subsonic jets, while the second is associated with large scale turbulence (LST). The LST structures are instability waves created at the edge of the jet due to the large velocity contrast between the jet flow and the atmosphere. These structures move downstream supersonically along the edge of the flow, generating Mach waves in a manner akin to a "wavy wall". At low Mach numbers, the effect of LST structures is greatly diminished [*Tam et al.*, 1996]. By fitting the observed volcanic spectra to the similarity spectra of *Tam et al.* [1996], *Matoza et al.* [2009] showed spectra from Mount St. Helens, USA and Tungurahua, Ecuador broadly fit the LST similarity spectra. *Fee et al.* [2010] postulate that the more complex (double-peaked), but stable Tungurahua spectra may be complicated by a combination of jet flow interactions with the heavily eroded crater walls and PDCs. They hypothesize that interaction of the flow-induced pressure field with the broad, deep crater at Tungurahua could be responsible for the first peak, while LST causes the second peak. The jet spectrum is fairly unique in volcano acoustics, as the spectra of other sources (e.g. harmonic tremor) has a different shape [*Garces et al.*, in review].

The frequency spectrum of jet noise scales according to the Strouhal number:

$$S_t = \frac{fD_j}{U_j} \tag{5.4}$$

where f=the peak jet noise frequency, D_j=expanded jet diameter, and U_j=jet velocity [*Seiner*, 1984]. Thus for a jet of constant Strouhal number, increases in jet diameter or velocity will lower the frequency. For pure-air laboratory jets, the observed peak Strouhal number lies between ~0.1-0.25, depending on the temperature and Mach number [*Tam*, 1995]. For the July and August 2006 eruptions of Tungurahua volcano, St≈0.4, while St≈0.06 for the March 2005 Mount St. Helens eruption [*Matoza et al.*, 2009]. Constraints from laboratory jets and observations of the peak jet frequency can thus lend insight into the expanded jet diameter and velocity.

5.5. Results

5.5.1 Propagation Modeling

Ray tracing and PE modeling is performed for both eruptions using the NRL-G2S models. Figure 5.2a shows sound speed, zonal (east-west, positive propagating easterly) and meridional (north-south, positive northerly) wind velocity above Kasatochi volcano on August 8, 2009 at 0000. Temperature follows a typical high-latitude profile of decreasing through the troposphere (~0-10 km), increasing in the stratosphere (~10-50 km), decreasing in the mesosphere (~50-90 km), followed by a significant increase in the troposphere (>90 km). Tropospheric winds are relatively minor. Meridional winds are small until ~100 km height where they increase rapidly to 90 m/s to the north. Zonal winds remain relatively weak throughout the entire model profile with a peak velocity of~45 m/s at ~65 km. This peak represents the prominent zonal stratospheric winds present during this time of year, which have been shown to be responsible for significant ducting of long-range infrasound [*Drob et al.*, 2003; *Le Pichon et al.*, 2009]. Winds along the great-circle path between Kasatochi and IS53 (Fig. 5.1, ~60° from N) are predicted to have little effect on ducting in the first ~60 km. The zonal wind peak around 65 km would act to refract sound up, as it is moving against the direction of propagation. Above 90 km, the winds increase substantially along the direction of propagation and enhance thermospheric ducting to IS53.

Figure 5.2b shows the predicted transmission loss at 0.1 Hz and ray tracing results from Kasatochi to IS53 on August 8, 2009 0000. PE amplitudes are given in dB relative

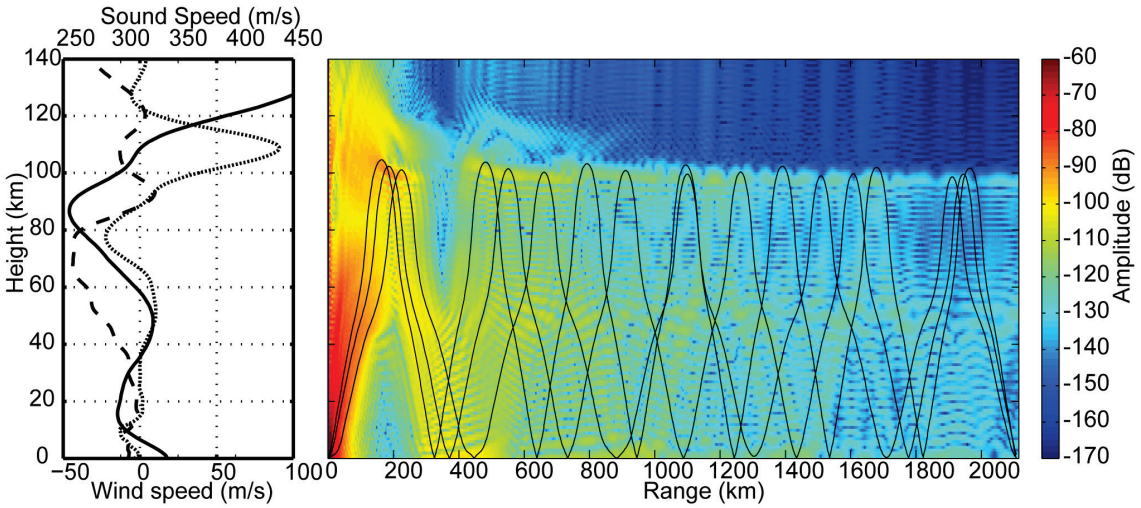

Figure 5.2. Atmospheric profiles and propagation modeling from Kasatochi to IS53 at August 8, 2009 0000 UTC. a) Sound speed (solid black) and zonal (east-west, positive to east) and meridional (north-south, positive to north) winds above Kasatochi. Sound speed and winds follow a typical high-latitude profile for this time of year. b) Ray tracing (black lines) and PE modeling at 0.1 Hz between Kasatochi and IS53. Both propagation models predict thermospheric arrivals. Strong northerly meridional winds above 90 km help to increase the effective sound speed in the thermosphere and refract sound downwards.

to 1 m from the source. There is some general agreement between the ray-tracing and PE modeling, with thermospheric ducting being the primary predicted source of acoustic transmission from the volcano to IS53. Although much of the energy dissipates into the upper atmosphere, some energy is refracted back towards the earth below 100 km height. Thermospheric arrivals are predicted to be lower in amplitude than stratospheric arrivals due to the increased attenuation present in the upper atmosphere and greater propagation distance [*Drob et al.*, 2003; *Sutherland and Bass*, 2004]. The PMCC-derived apparent horizontal phase velocities do not vary considerably during the pulses and are greater than 0.35 km/s, consistent with thermospheric arrivals with a high-angle of incidence. The first predicted ray at IS53 has travel time of ~7,965.6 s (~133 minutes) and celerity (great-circle distance divided by travel time) of 0.264 km/s. All IS53 data referenced

hereafter have the travel time removed, and thus refer to the time at the assumed source. The 0.1 Hz PE model predicts 129 dB loss at IS53. Propagation modeling to the other selected IMS arrays and for other frequencies of interest (0.01-1 Hz) also predicts thermospheric arrivals, as expected for a source at high latitudes [*Drob et al.*, 2003]. For Okmok, ray tracing predicts thermospheric arrivals as well, with travel time estimated at 6966 s to IS53. PE modeling at 0.1 Hz predicts 152 dB of loss at IS53 for Okmok, which is greater than that predicted for Kasatochi, even though it is closer to IS53. A stronger stratospheric wind jet opposing propagation along the great-circle path between Okmok and IS53 is likely responsible for the greater predicted transmission loss. Stratospheric ducting and gravity-wave perturbations [*Gibson et al.*, 2008] would affect travel times and predicted transmission loss.

5.5.2 Kasatochi Infrasound Observations

Five pulses of infrasound are detected from Kasatochi on August 7-8. Figure 5.3 shows the correlation values, beamformed IVLP waveforms, RMS pressure, and log-frequency spectrogram at IS53 encompassing the main eruption sequence (12 hours). Table 3 provides the IS53 recorded interval, inferred eruption interval, acoustic duration, and seismic origin times from the Alaska Volcano Observatory (AVO). The first IVLP acoustic signal begins at August 7 21:59:44 with a gradual onset and continues for the next ~123 minutes. This is referred to as Pulse 1. The acoustic origin time is consistent with the seismic (2201). RMS pressures are up to 0.22 Pa. Pulse 2 begins at 01:34:44 with a more impulsive onset. This pulse has a peak RMS pressure of 0.46 Pa, which is remarkably high considering the >2100 km range and the assumed thermospheric propagation path, and lasts ~59 minutes. Pulse 2 is clearly the most energetic and explosive, and the acoustic origin time would be ~15 minutes before the seismically-derived origin time if we assume the same atmospheric path as Pulse 1. Pulse 3 starts at 04:20:34 and has the shortest duration of ~33 minutes. The signal is emergent and RMS pressures are slightly higher than that of Pulse 1 but lower than Pulse 2. Similar to Pulse 2, the inferred acoustic origin time would precede the seismic by ~15 minutes under thermospheric refraction. All three pulses have high correlation values above 0.8 and mean detection azimuths of 242.8° ± 2.4° (actual is 241°). A fourth, less energetic

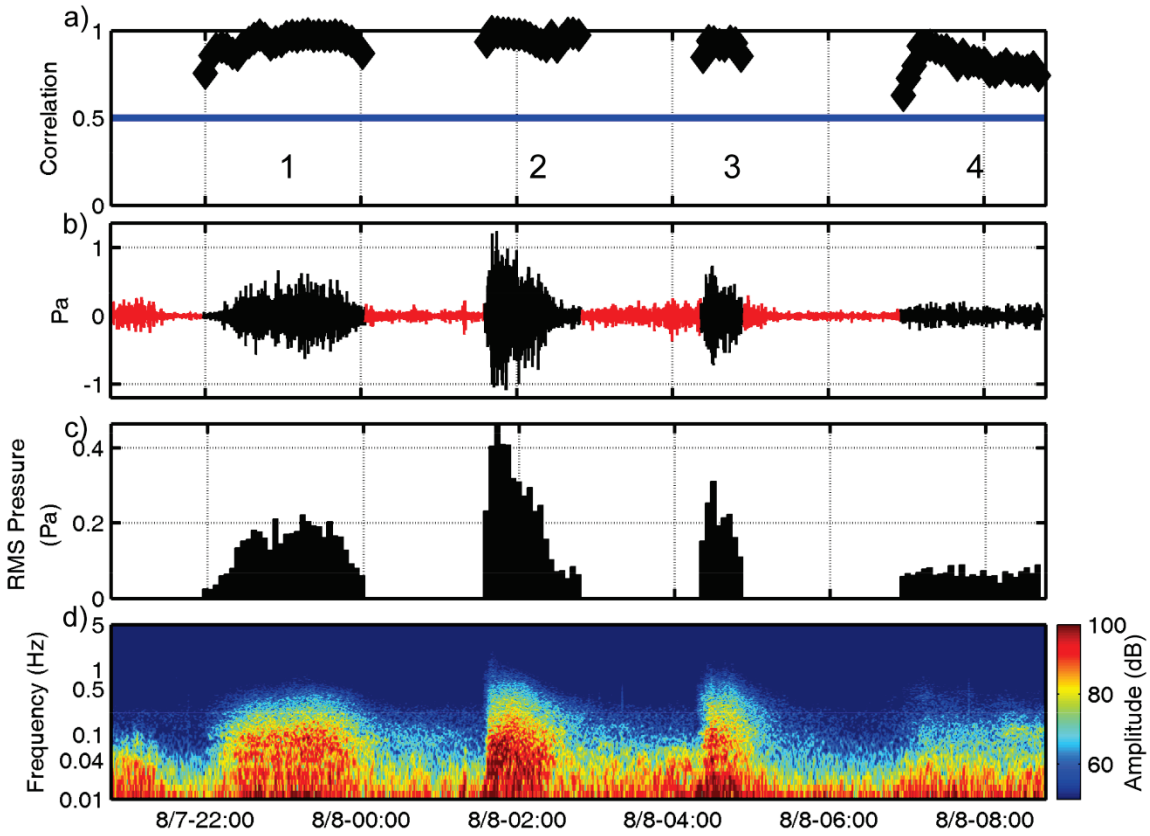

Figure 5.3. IS53 infrasound data for the Kasatochi eruption. Each data segment is split into 250 s windows for array processing. Modeled acoustic travel time from the volcano to the station has been removed. a) Correlation value for coherent IVLP (0.01-0.1 Hz) detections originating from a similar azimuth as Kasatochi. Three significant pulses of infrasound are detected, all with high correlation values. b) Beamformed IVLP waveforms. Black waveform segments correspond to coherent acoustic signal, as determined in a). The second pulse is the most impulsive and energetic. A fourth longer, lower amplitude pulse is also detected. c) RMS pressure in the 0.01-0.1 Hz band for each coherent window. d) Log-frequency spectrogram between 0.01-5 Hz. The first three pulses all have similar frequency content and are focused below 0.1 Hz with little variability during the pulse. Similar results are obtained for IS59 and IS18.

Table 5.3. List of modeled eruption origin time and durations for the Kasatochi eruption pulses and Okmok eruption. Satellite observations are determined from GOES imagery, while seismic origin times and durations are taken from [*Waythomas et al.*, 2008]. The modeled eruption interval is derived by subtracting the modeled acoustic travel time to IS53 from the first and last recorded infrasound at the array. The origin time difference represents the difference between the seismic and acoustic.

Pulse	Seismic Onset	Satellite Obs.	Modeled Eruption Interval at Source	Origin Time Difference (min)	Acoustic Duration (min)	Seismic Duration (min)
Kas 1	22:01	22:30	21:59:44 - 00:03:04	-1.3	123.3	68
Kas 2	01:50	02:30	01:34:44 - 02:47:14	-15	59	27
Kas 3	04:35	05:00	04:20:34 - 04:53:54	-14	33	35
Kas 4	07:12	N/A	06:53:54 - 08:46:14	-18	112	46
Okmok	19:43	20:00	19:41:54 - 05:00:00	-1	>540	N/A

eruption signal begins at 06:53:54. This pulse has IVLP acoustic energy and continues for a longer time period (>5 hours). A fifth pulse of activity focused in the MB band is also detected beginning around 1200 UTC. Due to the low S/N of Pulse 4 and 5, we focus our analysis on the first three pulses. The spectrogram in Figure 5.3d shows the majority of the acoustic energy lies below 0.1 Hz for the first four pulses and IVLP energy is sustained for the duration of each pulse with little variation.

Three clear eruption pulses were recorded at IS59 and IS18 in the IVLP band as well. Similar characteristics are present for all three pulses at these two stations. Three IVLP pulses are also detected at IS56 and IS10, although at much lower S/N. Higher wind-induced noise levels mask the pulses at IS30 and only weak identification is made. Pulses 4 and 5 are not as clearly detected at the other stations.

The shape and power of the acoustic spectra of each of the three main pulses are broadly similar. Figure 5.4a shows the I53 0.01-10 Hz power spectral density (PSD) typical of each of the main Kasatochi eruption pulses at IS53, plotted along with a typical background PSD (black) at the station and the predicted large scale turbulence (LST) jet noise spectrum centered at 0.04 Hz (gray). The spectrum for all three pulses has a similar shape and amplitude, composed of a broadband signal with a single spectral peak centered between 0.04-0.075 Hz. All three pulses are well above the background noise spectrum (e.g. 40-45 dB S/N at 0.1 Hz). Pulse 1 and Pulse 3 are centered at ~0.75 Hz with similar amplitudes, while Pulse 2 is centered at 0.04 Hz and has higher amplitude. Pulse 1 has a sharper roll-off at higher frequencies than the other pulses. The majority of the acoustic energy for all three pulses at IS53 is focused below 1 Hz. Above ~2 Hz, the signal is no longer above the background noise. Spectra for the Kasatochi eruption pulses have a similar shape at the other IMS stations. Figure 5.4b is a PSD typical of Pulse 2 at IS53, IS18, and IS59. Although the overall power levels are lower, the shape and center frequency for IS18 and IS59 spectra are consistent with that at IS53. Spectral comparisons for Pulse 1 and 3 show similar results. Due to the lower S/N, it is difficult to compare spectra over a broad frequency band for IS30, IS56, and IS10.

The shape of the spectra for the three pulses broadly resembles that of the LST jet spectrum (Fig. 5.4a). Here the LST spectrum is centered at 0.04 Hz to match that of Pulse 2. The center frequency and roll-off do not match as well at higher frequencies (>0.5 Hz),

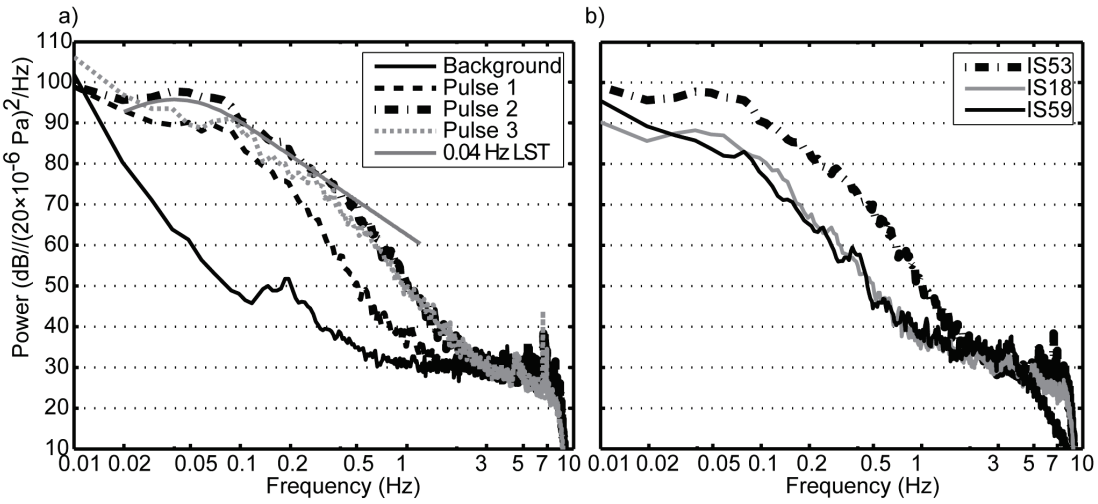

Figure 5.4. Kasatochi spectra. a) PSD typical of the three Kasatochi eruption pulses at IS53 (dotted lines), and their comparison to a typical background noise spectrum (black). Each spectrum is composed of 20 minute data segments. The spectra all have a similar shape with a peak between 0.04-0.075 Hz, and broadly resemble the LST spectrum predicted from jet noise (gray). Differences in the Kasatochi spectra and LST spectrum at higher frequencies may be due to increased attenuation. b) PSD of Pulse 2 at IS53, IS18, and IS59. The spectral shape and peak frequency between the pulses is similar, suggesting the frequency dependent propagation effects are similar between the stations and do not affect the general spectral shape.

which is likely related to increased attenuation at higher frequency. Section 5.6.3 discusses this in more detail.

5.5.3 Kasatochi Satellite Observations

Three prominent eruption pulses are observed in satellite imagery during the Kasatochi eruption. Due to its higher temporal resolution (30 minutes), GOES satellite imagery is used to constrain emission origin times. Pulse 1 is first observed at August 7 2230 (Fig. 5a) and the next two pulses the following day at 0230 and 0500 (Fig. 5b-c). Each of the pulses produce substantial umbrella clouds that initially spread radially until the prevailing wind fields control the plumes dispersion and transport them south. The

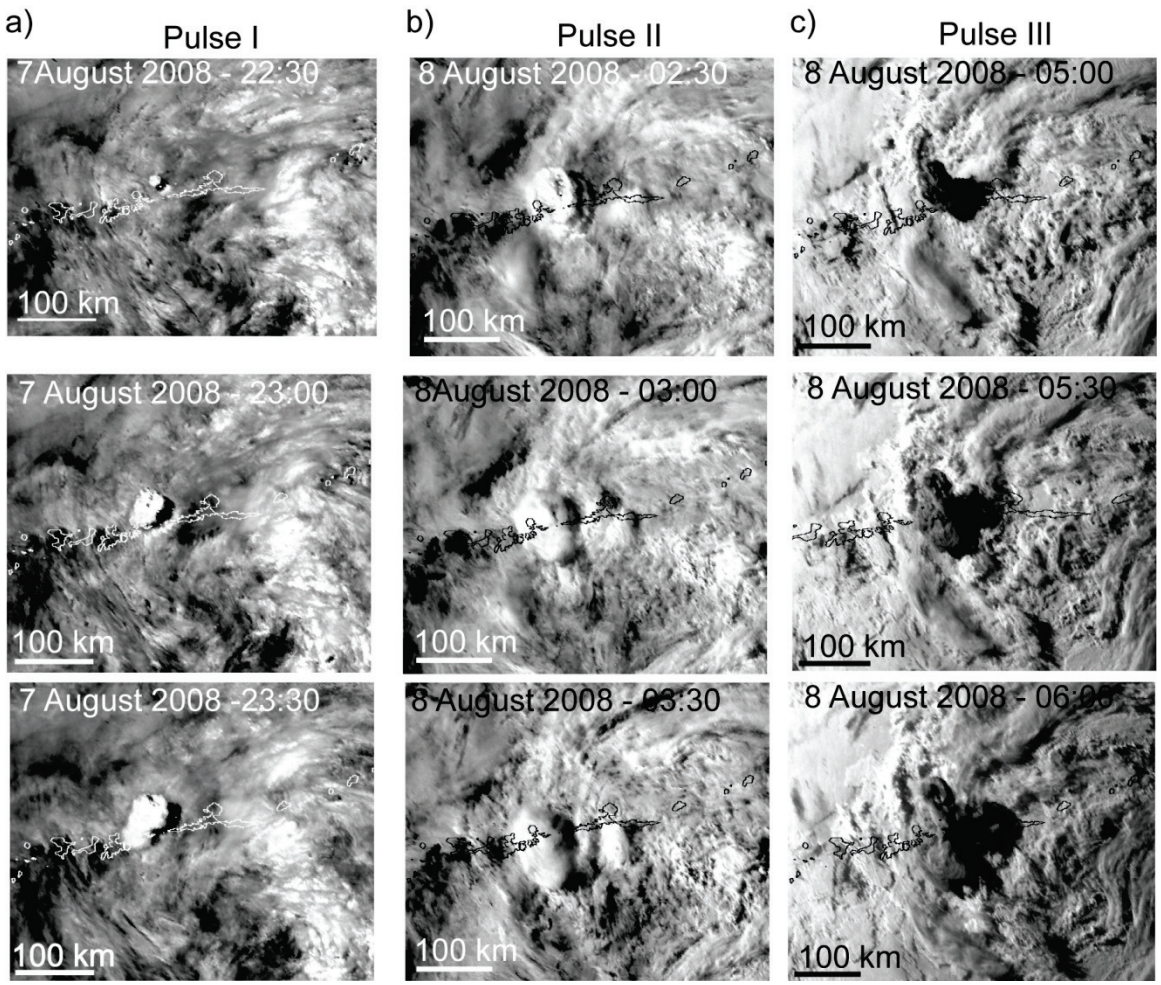

Figure 5.5. GOES visible images of the beginning of the three primary pulses that occurred during the Kasatochi eruption. Band one (VIS) imagery shows the beginning of the three different pulses: a) 2230, b) 0230, and c) 0500. Each pulse forms an umbrella cloud, the first two being vapor/steam rich (white) while the last pulse was more ash-rich (gray).

plume is then caught in a large-scale circulation gyre that transports the plume in a counterclockwise direction. The two initial umbrella clouds are more vapor/gas rich (determined from their white color in the visible imagery) while Pulse 3 is more ash-rich (determined from its darker color).

Five clear, high quality MODIS images were collected over the 25 hour eruption period, and imaged Pulse 1 and 3. As observed in the GOES imagery, Pulse 1 begins shortly after August 7 2220 with a small plume followed by the eruption of a large umbrella cloud observed (Fig. 6). The plume is transported to the southwest and then to the east in a counter clockwise gyre. An image collected at August 8 2305 shows that the eruption ended with just a small gas/steam plume connected to the volcano.

Temperatures collected from the TIR imagery suggest the plumes for all three eruption pulses were injected into the lower stratosphere with maximum plume tops ranging between 15–17 km. The main features of the plume dispersal are apparent in the TIR imagery as well. Velocity measurements could not be used to estimate accurate maximum plume heights, as the velocity differences between the wind fields at altitudes ranging between 10–16 km did not vary more than 4.4 m/s (the most accurate velocity measurement able to be acquired using the low-spatial resolution GOES data). Though the velocities measured still indicate the plume was transported within a range of altitudes ranging between 10 -16 km.

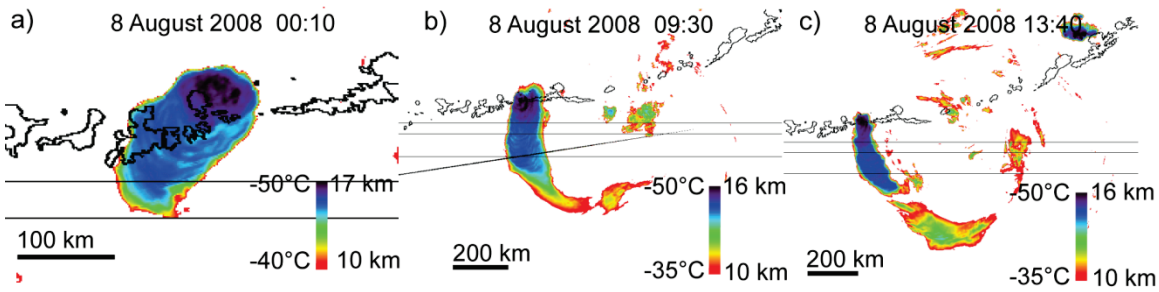

Figure 5.6. MODIS TIR (Band 31) imagery of the minimum temperatures of the Kasatochi eruption plumes at a) August 8 0010, b) August 8 0930 and c) August 8 1340. During the eruption period minimum temperatures recorded in this band were -52°C, suggesting a plume height of ~16 km maintained for each of the primary eruption pulses.

5.5.4 Okmok Infrasound Observations

IVLP energy from Okmok is detected at IS53, IS30, and IS59 with the highest S/N at IS53. All IVLP signals have relatively low S/N and detection is affected by local noise conditions. Higher S/N levels in the MB band (0.1-0.5 Hz) allow a clearer identification of the coherent signal in the I53 data (Fig. 7). Possible, although minor, MB band detection of the Okmok eruption may exist at IS56 and IS18. Assuming an eigenray calculated travel time of 6966 s from Okmok to IS53, sustained infrasound signals from Okmok begin at July 12 19:41:54 and last for at least 9 hours (Fig. 7, Table 3). Correlation values are lower than Kasatochi and hover between ~0.4-0.6 (Fig. 7a), with the detection threshold value set at 0.5. Filtered waveforms show a fairly steady, continuous signal increasing slightly at ~2200 (Fig. 7b). The large increase in infrasound between July 13 ~0130-0200 in Fig. 7b is wind related, as seen by the lack of acoustic detections. Acoustic signals taper off around July 13 0400. Spectral energy is focused below ~0.5 Hz and is fairly constant throughout the eruption. The most energetic eruption phase (July 12 ~1945-2130) was also detected in the MB and IVLP bands at I30, Japan.

The power and shape of the PSD curves for the IS53 Okmok signals all roughly agree (Fig. 8). The shape of the spectrum broadly follows that of Kasatochi and the jet noise spectrum, but also generally resembles the wind-noise dominated background spectrum (black). The low S/N for the Okmok eruption thus does not allow a clear determination if the spectra resemble that of jet noise. Acoustic energy is concentrated between 0.01-0.5 Hz. S/N and correlation values at IS53 are much lower than those from Kasatochi, even though the volcano is closer by ~400 km. However, the eruption is still clearly recorded at >3 stations for >8 hours.

5.5.5 Okmok Satellite Observations

The Okmok eruption was captured in satellite imagery collected by the GOES and MODIS sensors. Initially a large ash-rich umbrella cloud was produced and identified in the GOES VIS (Fig. 9a) and TIR imagery at July 12 2000. The plume grew radially from the vent for over an hour and transitioned into a more gas vapor rich plume at July 12 2100 (Fig. 9b). After the initial gravitational spreading ended the plume began to be transported by the dominant windfield to the southeast. A large plume continued to be

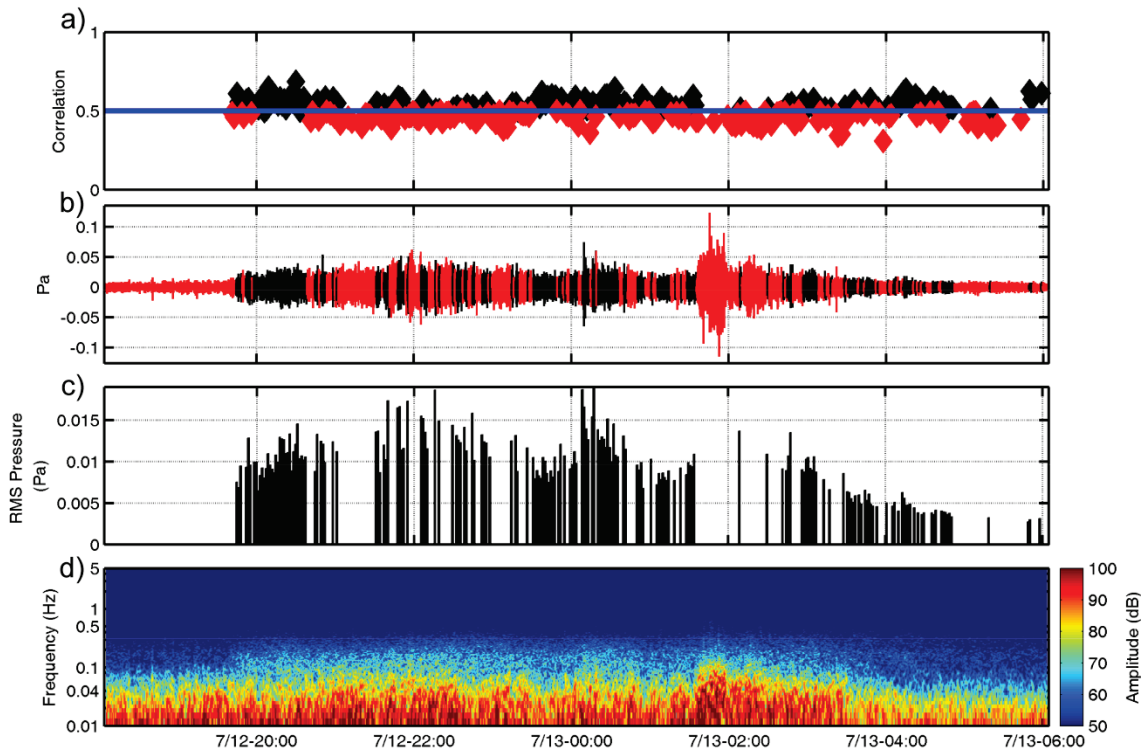

Figure 5.7. IS53 infrasound data for the Okmok eruption. a) Correlation values for each window, primarily between 0.4-0.6 Hz. b) MB (0.1-0.5 Hz) bandpassed, beamformed infrasound. Black segments indicate coherent signals. c) RMS pressure. Pressure values are much lower for Okmok than Kasatochi. d) 0.1-5 Hz log-frequency spectrogram. The Okmok signal is fairly constant and spectral amplitudes decrease above 1 Hz. Modeled acoustic travel time from the volcano to the volcano has been removed.

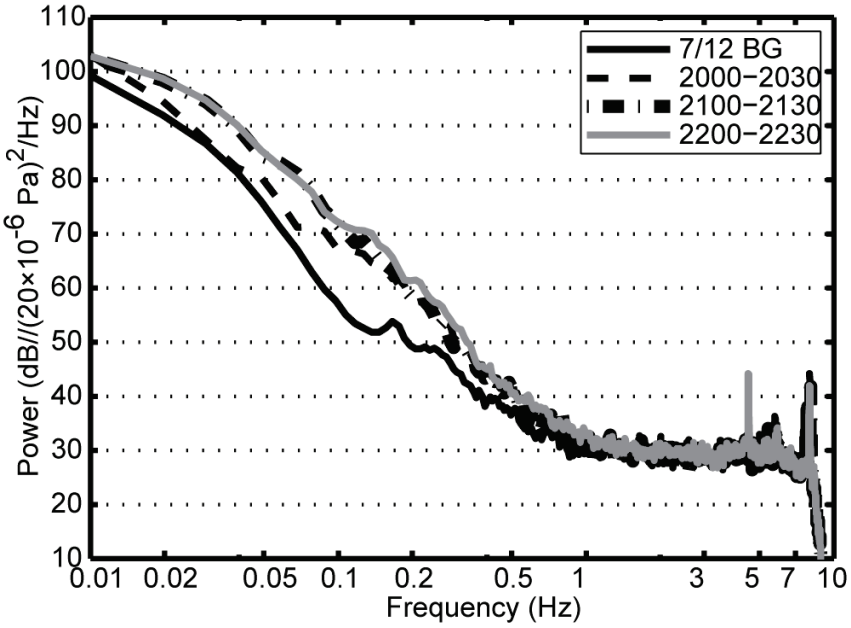

Figure 5.8. PSD for IS53 recordings of Okmok eruption. Three half hour sections from July 12, 2008 are selected and then beamformed. The black line represents a typical background noise spectrum. Infrasound rises above the background below ~1 Hz, and has the highest S/N in the MB band (0.1-0.5 Hz). The shape of all three spectra is similar, but the S/N is not high enough to robustly compare to the jet noise spectrum. Modeled acoustic travel time from the volcano to the volcano has been removed.

erupted from the vent for at least 13 hours, as observed at July 13 1000. The temperatures and dispersal pattern of the plume captured in the satellite data indicate that the plume reached a maximum altitude ranging between 15-17 km.

Four MODIS images were collected during the eruption period (Fig. 5.10). The first two images were collected during the beginning of the eruption (July 12 2145 and 2320) with two collected after the main eruption phase (July 13 0855 and 1300). At 2145 a large ash-rich umbrella cloud was observed measuring 138 x 96 km. By 2320 the MODIS image shows the plume grows in size (210 x 125 km) and has transitioned into a gas rich plume (Fig. 5.10). Minimum temperatures collected from these images were -62

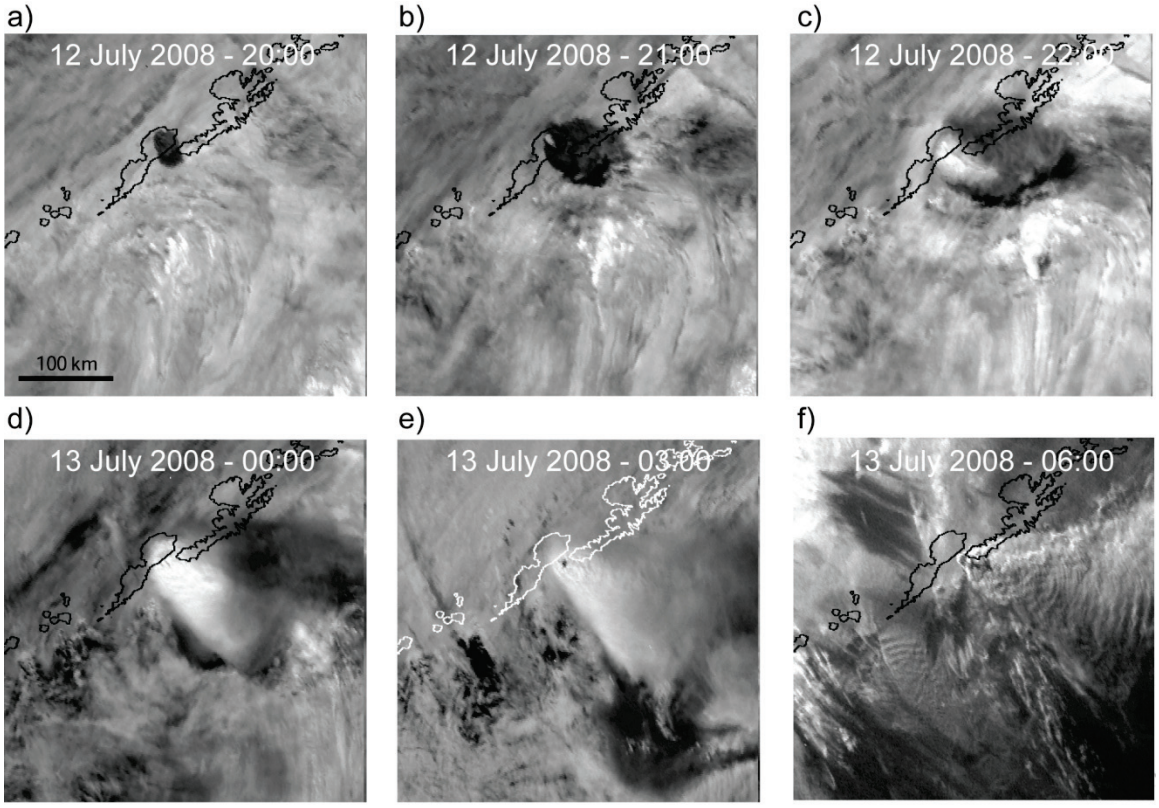

Figure 5.9. GOES VIS images depicting the progression of eruption cloud produced during the Okmok eruption on July 12-13. a-c) Band 1 (VIS) imagery depicting the transition from the initial ash-rich plume (a-2000, b-2100) to a more vapor rich plume by c-2200. The eruption initially produced a plume controlled by radially spreading (a-d) which transitioned into a plume that was transported by the prevailing wind fields (e-f, 0300-0600). The gravity waves at 2130 and 2300 UTC mentioned in the text are not shown here.

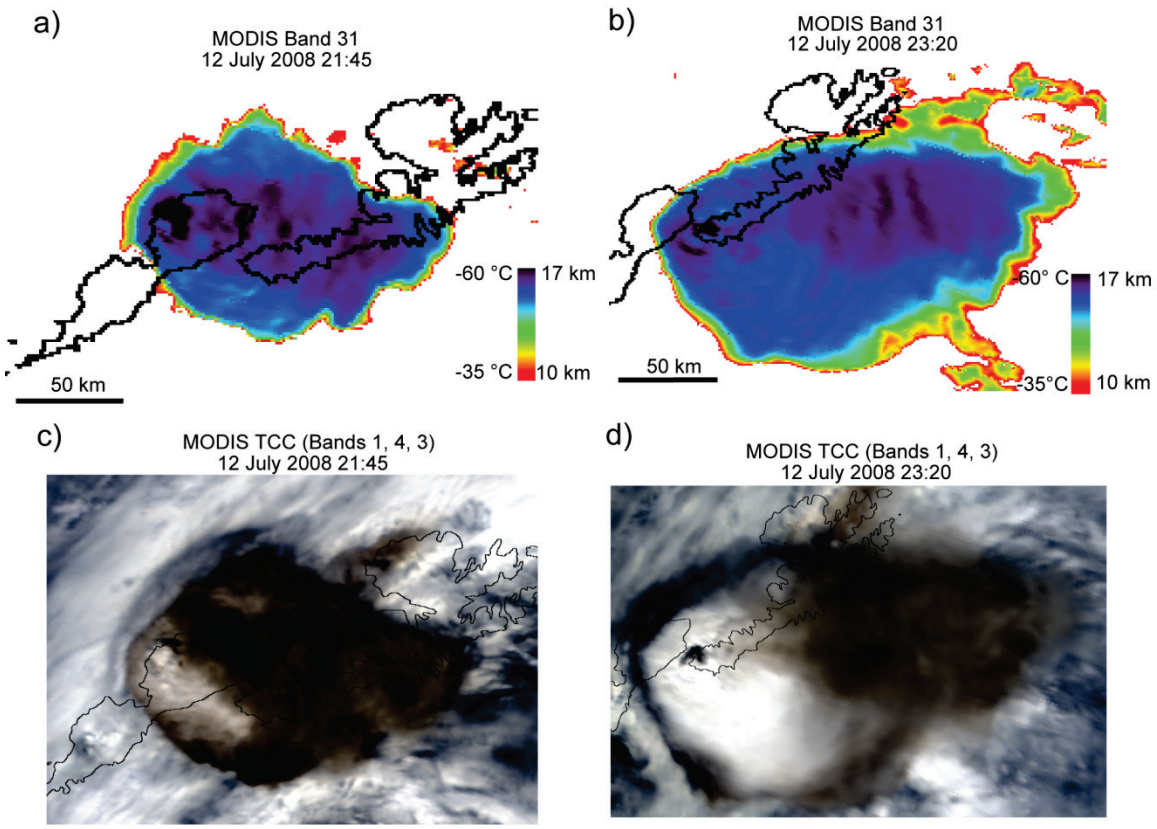

Figure 5.10. MODIS TIR (Band 31) (a-b,) and True Color Composite (Bands 1, 4, 3) (c-d) imagery of the Okmok eruption. Thermal imagery shows minimum temperatures of the plumes and the associated plume height estimates (a-b). Note the black areas of the plumes suggest portions of the plume that overshot the neutral buoyancy level and hence undercooled. Visible imagery shows the transitions of an ash-rich to a vapor-rich plume (c-d).

and -58 °C, respectively which are approximately 10°C cooler than temperatures of the surrounding atmosphere. These cooler temperatures indicate that undercooling of the plume has occurred (Fig. 5.10) and risen above its neutral buoyancy height. The undercooling is caused by the plume continuing to rise and decompress past its neutral buoyancy height [*Woods and Self*, 1992], and this observation is validated by the plume producing gravity waves that were captured by the GOES VIS imagery (Fig. 5.9). Two gravity waves were weakly detected in the imagery at 2130 and 2300.

5.6. Discussion

5.6.1 Eruption Origin Times and Durations

The estimated IVLP acoustic origin time for Kasatochi Pulse 1 (August 7 21:59:41) is similar to that listed by AVO (2201) and detected in the next available satellite image (2230) (Table 2), thus the estimated acoustic travel time seems reasonable. Further agreement is seen in the ray tracing results to IS59 and IS18, with predicted origin times of ~2204 and 2155, respectively. Thus the Pulse 1 acoustic origin time estimate seems robust. However, the predicted acoustic origin times for Pulse 2, 3, and 4 are earlier than those estimated by the AVO and satellite imagery by ~15 minutes (Table 2). For the Okmok eruption, the acoustic origin time (July 12 19:41:54) precedes the continuous seismic tremor (July 12 1943) by less than 2 minutes and is considered in good agreement with the satellite observations as well.

Multiple explanations for the discrepancies in the origin times are possible. Decoupling between the seismic and acoustic source (and thus timing) is possible, as the IVLP acoustic signals for Pulse 2, 3, and 4 may begin prior to the AVO detected seismicity and emissions visible in the satellite imagery. The relatively large (50 s) window lengths in processing the IVLP data also provide a constraint on the accuracy of the acoustic origin time. Inaccuracies in the atmospheric models would cause errors in the acoustic travel times and thus discrepancies between the inferred onsets. For example, the predicted arrivals at the IMS stations get refracted in the thermosphere. If we assume the rays get ducted in the stratosphere and use a typical stratospheric arrival celerity of ~0.30 km/s (compared to ~0.26 for thermospheric arrivals), then the rays are predicted to arrive at IS53 ~15 minutes earlier, in agreement with the seismic origin times. Thus the

discrepancies for the origin times of Kasatochi Pulse 2, 3, and 4 may be due to stratospheric, rather than thermospheric, arrivals at the arrays. Unaccounted for variability in the atmospheric profiles could create stratospheric ducting to the stations. Recent updates to the G2S models and potential inclusion of a gravity wave spectrum [*Gibson et al.*, 2008] may resolve some of the smaller-scale atmospheric features and provide more realistic propagation estimates.

Another possible atmospheric variation could be related to the eruption itself. Heavy particle loading in the lower 20 km of the atmosphere from the first Kasatochi pulse could scatter and/or refract sound into the stratospheric waveguide. The radiation of gravity waves from the volcano may also perturb the atmospheric temperature and velocity fields and may enhance stratospheric ducting. This could possibly explain why the later eruption pulses are consistent with stratospheric ducting celerities. Constraints on the amount of ash and gas particles during the initial eruption pulse are not currently available.

The infrasound durations from Kasatochi are generally longer than the seismically derived durations (Table 3). Pulse 3 is the exception, where the durations are within 2 minutes of each other. Infrasound recorded at a distant array is expected to be longer than at the source due to dispersion and multipathing during propagation (Fig. 5.2b). The predicted time difference between the first and last Kasatochi eigenrays is 709 s (11.8 min), which can be considered an upper bound on the overestimate of the acoustic eruption signal duration. As mentioned before, the seismic and acoustic source may also be decoupled. Significant emissions often produce noticeable infrasound [*Fee et al.*, 2010; *Steffke et al.*, 2010], thus the acoustic durations may coincide with the principal degassing episodes above the vent while the seismicity is more representative of subsurface activity.

5.6.2 Comparing Kasatochi and Okmok Eruptions

Although the 2008 Kasatochi and Okmok eruptions both ejected ash to similar heights within the stratosphere (~15-17 km), the infrasound at the IMS arrays is much higher for Kasatochi (Figures 5.3 and 5.7). For example, IS53 signals levels are much lower for the Okmok eruption (e.g. ~20 dB), even though it is closer to the array than

Kasatochi. The lower frequency content for the Kasatochi eruption (Figures 5.4 and 5.8) is indicative of a longer period and possibly more energetic acoustic source. The elevated infrasound and lower frequency content for Kasatochi are consistent with the more explosive nature of the Kasatochi eruption, as evidenced by the higher amount of fine ash (300 kt) and SO_2 (~1.5 TG) compared to Okmok (150 kt fine ash and ~0.1 TG SO_2) [*Corradini et al.*, 2010; *Prata et al.*, submitted].

Ash and gas emissions from the eruptions reached similar heights (~15-17 km maximum) (Figures 5.5,6,9,10). This is unexpected considering the apparently higher acoustic energy from Kasatochi. No significant wind or temperature impediment is apparent between 15-17 km that would inhibit plume rise. Examination of the atmospheric profiles at both volcanoes shows the tropopause (which would inhibit plume rise) lies at ~9-10 km. Thus the ~15 km upper limit for the Kasatochi and Okmok plumes is assumed to be related to the eruptions themselves and not an atmospheric effect.

5.6.3 Jet Noise from Kasatochi and Okmok and its Implications

The acoustic spectra produced by Kasatochi Volcano on August 7-8, 2008 recorded at distant arrays (>2000 km) largely resembles the similarity spectra for LST (Fig. 5.4a) [*Tam et al.*, 1996] and the spectra from explosive eruptions observed at regional distances [*Fee et al.*, 2010; *Matoza et al.*, 2009]. Kasatochi produced a broadband spectrum with a single dominant peak centered in the IVLP band and a frequency roll-off similar to that of the LST spectrum. The small-scale turbulence (SST) spectrum [*Tam et al.*, 1996] has a much broader shape and does not closely resemble the Kasatochi spectrum, suggesting LST is more likely to be the dominant noise source. This suggests high jet Mach numbers, which is consistent with the explosive nature of the Kasatochi eruption pulses. The peak frequency and spectral shape for IS18 and IS59 Kasatochi spectra (Fig. 5.4b) are similar to that for IS53, thus propagation is possibly not affecting the general shape of the spectrum at the lower frequencies. The spectra from Kasatochi Pulse 1 appears to have a sharper roll-off than the other pulses (Fig. 5.4a), and this may be related to thermospheric refraction (thus encountering increased attenuation at higher frequencies). The increased roll-off at higher frequencies provides further evidence that Pulse 1 is thermospheric while Pulse 2, 3, and 4 are stratospheric.

The mismatch between the Kasatochi and LST spectra at higher frequencies is likely related to increased attenuation at these frequencies. The PE predicted transmission loss for the path between Kasatochi and IS53 as a function of frequency between 0.01-1 Hz is shown in Figure 5.11a. The predicted transmission loss at higher frequencies (e.g. ~177 dB at 1 Hz) is significantly greater than that at low frequencies (e.g. ~129 dB at 0.1 Hz). If the calculated transmission loss is applied to the recorded spectrum to estimate the source spectrum, the dominant source frequency of the Kasatochi eruption signals would be at relatively high frequencies (>1 Hz), which is inconsistent with the assumed large jet diameter, high jet velocity, and stratospheric ash emissions. Further, a drastic decrease in transmission loss at 0.25 Hz (compared to lower frequencies) is predicted (Fig. 5.11a). Thus it seems that the predicted transmission loss provides unrealistic source spectrum predictions as it overestimates transmission loss at high frequencies.

The primary source of predicted loss is the molecular attenuation process in the thermosphere. Figure 5.11b shows the total estimated absorption as a function of height [*Sutherland and Bass*, 2004] for the frequencies used in Figure 5.11a. For higher frequency acoustic energy (e.g. >0.25 Hz) that propagates through the thermosphere, significantly higher amounts of absorption are predicted (up to 1 dB/km). Thus a disproportional amount of attenuation is predicted for higher frequency acoustic energy traveling in the thermosphere compared to lower portions of the atmosphere. Changes in the ducting height due to wind and temperature variability [*Gibson et al.*, 2008] will significantly affect the estimated transmission loss, and thus the modeled transmission loss in Figure 5.11a should be taken as a coarse estimate. Another potential method of finding the atmospheric transfer function would be to do it empirically. Comparing the spectra of an energetic source at various calibrated local, regional, and telesonic stations could provide an empirical atmospheric transfer function, as well a means to validate the current atmospheric and propagation models. Unfortunately, no near-source acoustic observations exist for the Kasatochi or Okmok eruptions.

The peak jet frequency is the most accessible acoustically-derived parameter for volcanic jets, as only high S/N jetting signals and broadband sensors are necessary. The

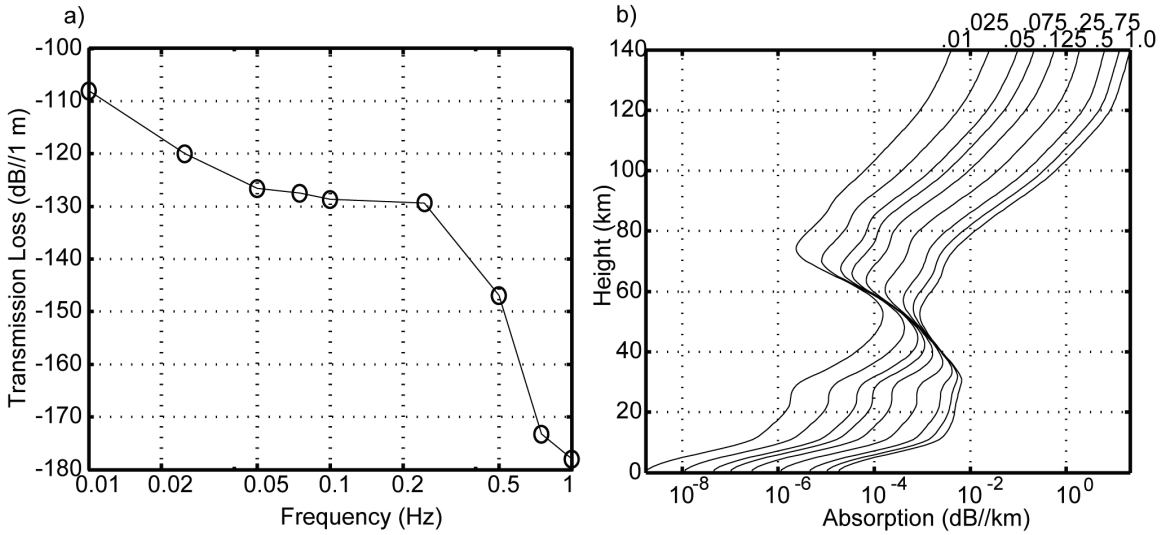

Figure 5.11. Frequency-dependent transmission loss and absorption. a) Predicted transmission loss between Kasatochi and IS53 on August 8, 2008 0000. The transmission loss is calculated using the PE at discrete frequencies between 0.01-1 Hz, but utilizes an incomplete representation of atmospheric variability [*Gibson et al.*, 2008]. b) Absorption as a function of height after Sutherland and Bass [2004]. Total absorption is calculated for the frequencies in a), with each curve labeled at the top of the plot. Absorption increases with increasing frequency. Increasing absorption in the troposphere is followed by a decrease in the stratosphere. Absorption again increases in the mesosphere and thermosphere.

peak frequencies of the Kasatochi eruption spectra (0.04-0.075 Hz) (Fig. 5.4a) are similar to that from the paroxysmal Plinian stage of the August 17, 2006 Tungurahua eruption, which ejected ash to ~24 km. The frequencies are significantly lower than the peak frequencies for the March 8, 2005 phreatic eruption of Mount St. Helens (~0.2 Hz) and the July 15, 2006 and February 6, 2008 Tungurahua eruptions (~0.4 Hz) [*Fee et al.*, 2010; *Matoza et al.*, 2009]. Due to the remote location of Kasatochi, we do not have constraints on the jet velocity or diameter. However, the very low jet frequency points to a large jet diameter to velocity (D/U) ratio (Eq. 5.). Assuming similar noise generation and Strouhal numbers, we can use estimates of S_t from a comparable eruption at Tungurahua (S_t~0.4

[*Matoza et al.*, 2009]) to estimate the D/U ratio to be between ~5-10 for Kasatochi. Although the Okmok spectrum is above the noise at IS53 below ~0.5 Hz (Fig. 8), the entire broadband spectrum is not discernible and thus comparison to the similarity spectra is not possible. Before estimation of the jet source parameters can be made using the Strouhal number (Eq. 5.4) the peak Strouhal numbers of hot, multiphase jets needs to be determined, as well as better constraints on jet velocity and diameter.

The double-peaked jetting spectrum from Tungurahua [*Fee et al.*, 2010; *Matoza et al.*, 2009] is not observed at Kasatochi. *Fee et al.* [2010] proposed that the first Tungurahua spectral peak may be due to jet-crater interactions, while the second from LST. Interaction between the jet flow and the crater at Kasatochi may be vastly different than Tungurahua. The jet at Tungurahua is presumed to be overpressurized due to its observed large width (wider than the crater) [*Fee et al.*, 2010; *Matoza et al.*, 2009], and thus the turbulent flow likely interacted with the eroded crater. Kasatochi's ~0.75 km wide by 250 m deep crater [*Smithsonian*, 2008b] may be too wide or shallow to significantly affect the jet. Further, the Kasatochi jet pressure at the vent may not have been significantly greater than the ambient, thus limiting the amount of decompression and expansion of the jet to less than that of the crater width. Turbulence within the high velocity jet would then be the dominant acoustic source.

The three Kasatochi eruption pulses provide a unique opportunity to examine the effects of particles on the jet noise spectrum. Pulse 1 and 2 clearly have ash-poor, steam-rich jets while Pulse 3 has a much more ash-rich plume (Fig. 5). Presumably the first two eruption pulses vaporized the lake, leaving little water to be incorporated into the Pulse 3 jet and plume. The addition of a large amount of solid particles to the plume is predicted to inhibit turbulence [*Sparks et al.*, 1997] and thus jet noise. In addition, sound from the jet flow interacting with the solid ash particles would produce a different type of sound [*Woulff and McGetchin*, 1975] and likely a different spectrum. At Kasatochi the jet spectra at all arrays vary little in response to an increase in ash particles. This observation is consistent with those at Tungurahua, where the jet spectrum was relatively stable over periods of hours despite the fact that jet particle concentrations likely changed [*Fee et al.*, 2010; *Matoza et al.*, 2009]. One explanation may be related to the location of the LST. Instability waves should form along the edges of the jet and propagate downstream, thus

limiting their interactions with the interior of the jet where the highest concentration of particles exists. Thus far, little work has been published on the jet noise produced from solid particle laden jets, and future work is required to confirm these speculations.

5.7. Conclusions

Sustained, broadband infrasound recordings from the 2008 eruptions of Kasatochi and Okmok volcanoes are recorded at over six IMS arrays. Propagation modeling primarily predicts thermospheric ducted arrivals. The acoustic signals are focused at low frequencies (0.01-0.5 Hz) and are indicative of ash and gas injection into the stratosphere, in accordance with previous observations of energetic eruptions. The Kasatochi eruption produced higher infrasound at the arrays than Okmok, although both erupted ash to similar heights within the stratosphere (15-17 km). Acoustically derived origin times for the Okmok eruption and first pulse of the Kasatochi eruption are in agreement with the seismic and remote sensing origin times. However, the predicted acoustic origin times of thermospheric arrivals for the second, third, and fourth Kasatochi eruption pulses precede the seismic and remote sensing origin time by ~15 minutes. For these pulses, the actual acoustic origin time may precede the seismic and visual origin time, or more likely, an incomplete model of atmospheric variability would predict inaccurate acoustic propagation paths and travel times. Stratospheric arrivals for these pulses with typical celerities of ~ 0.30 km/s would predict an origin time in line with seismic estimates. It is possible that the first eruption pulse introduced (1) dense ash and hot gas layers that could refract or scatter sound into the stratospheric waveguide and (2) a gravity wave field perturbed the atmospheric propagation conditions, possibly leading to enhanced stratospheric ducting for the later pulses.

Spectra from the Kasatochi eruption recorded at telesonic distances resemble the similarity spectra predicted for man-made jets and those from other recent large eruptions, suggesting scalable acoustic source processes. The three main Kasatochi eruption pulses have broadband spectra peaked between 0.04-0.075 Hz with similar spectral shapes between pulses and arrays. Satellite observations reveal the first two Kasatochi eruptions pulses are steam-rich and ash-poor, while the third is ash-rich. The inclusion of ash

particles in the jet of the third Kasatochi eruption pulse does not appreciably change the acoustic spectrum. A better understanding of particle-laden jet noise processes would aid in hazard mitigation and characterization of the gas thrust (jet) region of large eruptions.

An attempt to quantitatively estimate the Kasatochi source spectrum by modeling the propagation loss as a function of frequency provides unrealistic attenuation factors. Future empirical studies of infrasound recordings at varying distances may help validate atmospheric models and further characterize large volcanic eruptions at telesonic distances. Advances in atmospheric models may also reduce the considerable uncertainty in current propagation modeling.

Acknowledgements

A version of this chapter is being published as: Fee, D., A. Steffke, and M. Garces (in press), Characterization of the 2008 Kasatochi and Okmok eruptions using remote infrasound arrays *Journal of Geophysical Research-Atmospheres.* The authors wish to thank the entire ASHE team. We are grateful once again to Doug Drob for providing the G2S models. Helpful conversations with Ken Arnoult and Robin Matoza helped improve the manuscript. The manuscript was improved by three thoughtful reviews. This research was supported by NOAA via University of Mississippi subcontract 09-09-022.

CHAPTER 6: CONCLUSIONS AND FUTURE WORK

The following chapter synthesizes conclusions from earlier chapters and discusses future areas of work in volcano acoustics relevant to this dissertation.

6.1 Conclusions

The preceding chapters demonstrated the utility of using infrasound to constrain volcanic eruptions by providing important source parameters. Although the four volcanoes studied here displayed a wide range of eruption styles, infrasound was able to provide insight into the timing, location, intensity, escalation, and character of each eruption.

Chapters 2 and 3 presented the diversity of acoustic signals from Kilauea volcano. The 2007 East Rift Zone fissure eruptions were exclusively located and timed using infrasound. At Halema'uma'u, persistent degassing and transient degassing bursts caused the overlying gas-filled cavity to resonate. Modeling the tremor source assuming both Helmholtz and acoustic resonance provides reasonable estimates of the volume and dimensions of the cavity. Changes in the tremor frequency and energetics during the study period are correlated with presumed changes in cavity dimensions, degassing, magma flux, and the lava level within the cavity. From this chapter it is clear that geometric constrictions affect the type of acoustic signal emitted from the Halema'uma'u vent, as well as affecting the temperature, seismic-acoustic coupling, and style of degassing.

In Chapter 4, five case studies of infrasound from Tungurahua Volcano are used to determine the acoustic signature of ash emissions. Although thousands of transient explosions were recorded, sustained intense eruptions were found to produce substantially more ash. These eruptions were identifiable from their spectral shape and frequency content. Chapter 5 confirms the assertions of Chapter 4. Intense, low frequency, sustained infrasound from Kasatochi and Okmok Volcanoes are coincident with hazardous high-altitude ash emissions. Similar to Tungurahua, these eruptions display the characteristic jet noise spectrum, which is identifiable at telesonic distances. Chapter 5

also demonstrates how the relative vigor and known, stationary location of volcanoes make them prime sources for acoustic propagation studies.

6.2 Future Work

6.2.1 Resonance

The identification of Helmholtz resonance at Kilauea Volcano in Chapter 3 presents an avenue of potential research. To date no other observations of Helmholtz resonance at volcanoes have been reported. However, numerous volcanic cavities may be able to support Helmholtz resonance, particularly at low viscosity, less explosive volcanoes like Kilauea. More detailed study of Helmholtz resonance will require better constraints on the sound speed, as it is the largest unknown in determining the volume and other cavity characteristics. Numerous types of flow induced resonances [*Rockwell and Naudascher*, 1979] may also be applicable at volcanoes and present another potential research area.

6.2.2 Jet Noise

The identification of volcanic jet noise could be a major step forward in volcano acoustics and volcanology in general. Considerable research has been made on man-made jet noise (see [*Tam*, 1998; *Tam et al.*, 2008] for reviews), and some of this work may be applicable to volcanic jets. For example, important parameters such as jet velocity and diameter may be deduced from the Strouhal number, which can be ascertained through the frequency, velocity, and width of the jet. More recordings of constrained volcanic jets are necessary to determine the range of Strouhal numbers for volcanic jets.

The double-peaked spectrum from Tungurahua volcano must also be examined further, as it presents a considerable departure from the single-peaked man-made jet noise spectrum. Chapter 4 postulates that interactions of the jet with the volcanic crater may be a significant source of infrasound and responsible for the first Tungurahua spectral peak. This interaction will likely be most relevant to volcanoes with heavily eroded craters and over-expanded jets [*Woods and Bower*, 1995].

Two avenues of future research in volcano aeroacoustics are comparing infrasonic observations with numerical and laboratory modeling. Recent numerical modeling of compressible jet flows [*Ogden et al.*, 2008a; *Ogden et al.*, 2008b] has shown marked improvement. This type of modeling may soon be able to estimate the acoustics produced from supersonic jet flows. Laboratory work has also shown promise. *Clarke et al.* [2009] performed analogue experiments of Vulcanian eruptions and examined jet flow characteristics. Turbulence structures within the jets are clearly present. *Solovitz and Mastin* [2009] simulated volcanic jetting by injecting a stream of particles into a jet and looked at the overall entrainment of air. The effect of solid particles and high temperatures on volcanic jet noise needs to be addressed.

6.2.3 Ash and Aviation

The recent eruption of Eyjafjallajökull Volcano, Iceland severely interrupted air travel in the North Atlantic and Europe and raised the relevance of volcanic ash and aviation. The ASHE project has shown promise in using infrasound and remote sensing to detect and notify the aviation authorities of hazardous volcanic eruptions. Chapters 4-5 demonstrated that high-altitude ash emissions are coincident with low frequency volcanic jetting. However, further work is necessary to confirm this relationship. Numerous other Vulcanian-Plinian eruptions have recently been recorded with high-resolution infrasound microphones, particularly at IMS stations. The recent eruptions of Redoubt Volcano, Alaska and Sarychev Volcano, Russia are two prime targets for studies similar to Chapters 4-5.

The automatic identification of the jet noise signature is also relevant to ash monitoring. Rapid identification of the jet noise spectrum may lead to improved early detection and notification of volcanic eruptions. Neural networks [e.g. *Ham et al.*, 1999] are a logical choice for identification. Volcanic jetting (and/or ash emissions) may indeed have other characteristic features besides its spectrum that should be explored.

Although near real-time monitoring of volcanoes using global infrasound networks is attractive, one major obstacle is the long travel time from source to receiver. For example, sound will take about one hour to travel every 1000 km. Deployment of more, or at least well-positioned, arrays can help reduce this impediment.

6.2.4 Propagation Studies

A proper understanding of the source itself must be made before robust propagation estimates are made. Although volcanoes may be good sources of infrasound and thus appealing for propagation studies, they may also have complex and dynamic sources. As suggested in Chapter 5, telesonic propagation studies using volcanoes would greatly benefit from robust source recordings. The author suggests local and regional array recordings be combined with telesonic arrays. Atmospheric models may then be properly validated. The recent 2009 Redoubt, Alaska eruption was recorded by infrasound microphones at 12 km [*McNutt et al.*, 2009] and numerous telesonic IMS arrays [*Arnoult et al.*, 2009] . Note that other geophysical data (e.g. seismic, remote sensing) may be necessary to get accurate onset times and locations if infrasonic source recordings are not possible.

REFERENCES

.

Almendros, J., B. A. Chouet, P. B. Dawson, and C. Huber (2002), Mapping the sources of the seismic wave field at Kilauea Volcano, Hawaii, using data recorded on multiple seismic antennas, *Bulletin of the Seismological Society of America*, *92*(6), 2333-2351.

Arellano, S. R., M. Hall, P. Samaniego, J.-L. Le Pennec, A. Ruiz, I. Molina, and H. Yepes (2008), Degassing patterns of Tungurahua volcano (Ecuador) during the 1999-1006 eruptive period, inferred from remote spectroscopic measurements of SO2 emissions, *Journal of Volcanology and Geothermal Research*, *176*, 151-162.

Arnoult, K., J. V. Olson, C. Szuberla, S. R. McNutt, M. Garces, D. Fee, and M. A. Hedlin (2009), Infrasound Array Observations of the Recent Explosive Eruptions of Mt. Redoubt, Alaska, paper presented at American Geophysical Union, Fall Meeting 2009.

Arnoult, K. M., J. V. Olson, C. A. Szuberla, S. R. McNutt, M. Garces, D. Fee, and M. Hedlin (in review), Infrasound Observations of the Recent Explosive Eruptions of Okmok and Kasatochi Volcanoes, Alaska, *J. Geophys. Res.*

Assink, J. D., L. G. Evers, I. Holleman, and H. Paulssen (2008), Characterization of infrasound from lightning, *Geophysical Research Letters*, *35*(15).

Barba, D., S. Arellano, P. Ramon, P. Mothes, A. Alvarado, G. Ruiz, and L. Troncoso (2006), Cronologia de los Eventos Eruptivos de Julio y Agosto del 2006 del Volcan Tungurahua, paper presented at Resumenes extendidos de las 6th Jornadas en Ciencias de la Tierra, EPN - DG, Quito - Ecuador.

Brown, D., and M. Garces (2008), Ray Tracing in an Inhomogeneous Atmosphere with Winds, in *Handbook of Signal Processing in Acoustics*, edited by D. Havelock, S. Kuwano and M. Vorlander, pp. 1437-1460, Springer, New York.

Buckingham, M. J., and M. A. Garces (1996), Canonical model of volcano acoustics, *Journal of Geophysical Research, B, Solid Earth and Planets*, *101*(4), 8129-8151.

Cansi, Y. (1995), An automatic seismic event processing for detection and location; the P.M.C.C. method, *Geophysical Research Letters*, *22*(9), 1021-1024.

Cansi, Y., and A. Le Pichon (2008), Infrasound Event Detection Using the Progressive Multi-Channel Correlation Algorithm, in *Handbook of Signal Processing in Acoustics*, edited by D. Havelock, S. Kuwano and M. Vorlander, pp. 1425-1435, Springer, New York.

Carn, S. A., A. J. Krueger, N. A. Krotkov, S. Arellano, and K. Yang (2008), Daily monitoring of Ecuadorian volcanic degassing from space, *Journal of Volcanology and Geothermal Research*, *176*(1), 151-162.

Ceranna, L., A. Le Pichon, D. N. Green, and P. Mialle (2009), The Buncefield explosion: a benchmark for infrasound analysis across Central Europe, *Geophysical Journal International*, *177*(2), 491-508.

Chouet, B. (1985), Excitation Of A Buried Magmatic Pipe - A Seismic Source Model For Volcanic Tremor, *Journal Of Geophysical Research-Solid Earth And Planets*, *90*(NB2), 1881-1893.

Chouet, B., P. Dawson, M. R. James, and S. J. Lane (in review), Seismic source mechanism of degassing bursts at Kilauea 1. Results from waveform inversion in the 10 - 50 s band.

Chouet, B. A. (1996), New Methods and Future Trends in Seismological Volcano Monitoring, in *Monitoring and Mitigation of Volcano Hazards*, edited by R. Scarpa and R. I. Tilling, pp. 23-97, Springer-Verlag.

Christie, D. R., and P. Campus (2010), The IMS Infrasound Network: Design and Establishment of Infrasound Stations, in *Infrasound Monitoring for Atmospheric Studies*, edited by A. Le Pichon, E. Blanc and A. Hauchecorne, pp. 29-75, Springer.

Clarke, A. B., J. C. Phillips, and K. N. Chojnicki (2009), An investigation of Vulcanian eruption dynamics using laboratory analogue experiments and scaling analysis, in *Studies in Volcanology: The Legacy of George Walker*, edited by T. Thordarson, S. Self, G. Larsen, S. K. Rowland and A. Hoskuldsson, pp. 155–166, IAVCEI, London.

Corradini, S., L. Merucci, A. J. Prata, and A. Piscini (2010), Volcanic ash and SO2 in the Kasatochi and Okmok eruptions: Retrievals comparison from different IR satellite sensors, *Journal of Geophysical Research* (this issue).

de Groot-Hedlin, C. D., M. A. H. Hedlin, and D. P. Drob (2010), Atmospheric Variability and Infrasound Monitoring, in *Infrasound Monitoring for Atmospheric Studies*, edited by A. Le Pichon, E. Blanc and A. Hauchecorne, pp. 475-507, Springer.

DeFatta, D. J., J. G. Lucas, and W. S. Hodgkiss (1998), *Digital Signal Processing: A System Design Approach*, John Wiley, NY.

Drob, D. P., J. M. Picone, and M. Garces (2003), Global morphology of infrasound propagation, *Journal of Geophysical Research-Atmospheres*, *108*(D21).

Duffield, W. A., R. L. Christiansen, R. Y. Koyanagi, and D. W. Peterson (1982), Storage, migration, and eruption of magma at Kilauea volcano, Hawaii, 1971-1972, *Journal of Volcanology and Geothermal Research*, *13*, 273-307.

Evers, L. G., and H. W. Haak (2005), The detectability of infrasound in the Netherlands from the Italian volcano Mt. Etna, *Journal Of Atmospheric And Solar-Terrestrial Physics*, *67*(3), 259-268.

Evers, L. G., and H. W. Haak (2007), Infrasonic forerunners: Exceptionally fast acoustic phases, *Geophysical Research Letters*, *34*(10).

Evers, L. G., and H. W. Haak (2010), The Characteristics of Infrasound, its Propagation and Some Early History, in *Infrasound Monitoring for Atmospheric Studies*, edited by A. Le Pichon, E. Blanc and A. Hauchecorne, pp. 3-27, Springer.

Fee, D., and M. Garces (2007), Infrasonic tremor in the diffraction zone, *Geophysical Research Letters*, *34*(16).

Fee, D., M. Garces, and T. Orr (2007), Seismic and Infrasound Recordings from Kilauea Volcano: Volcanic Tremor, Lava Outbreaks, and Fissure Eruptions, paper presented at American Geophysical Union, Fall Meeting 2007, abstract #V53A-1132, San Francisco.

Fee, D., M. Garces, and A. Steffke (2010), Infrasound from Tungurahua Volcano 2006–2008: Strombolian to Plinian eruptive activity, *Journal of Volcanology and Geothermal Research*, *193*, 67-81.

Fee, D., A. Steffke, and M. Garces (in press), Characterization of the 2008 Kasatochi and Okmok eruptions using remote infrasound arrays *Journal of Geophysical Research-Atmospheres*.

Fee, D., M. Garces, M. Patrick, B. Chouet, P. Dawson, and D. Swanson (in review), Infrasonic Harmonic Tremor and Degassing Bursts from Halema`uma`u Crater, Kilauea, *Journal of Geophysical Research-Solid Earth*.

Garces, M., D. Fee, and R. S. Matoza (in review), Volcano Acoustics, in *Modeling Volcanic Processes: The Physics and Mathematics of Volcanism*, edited by S. A. Fagents, T. K. P. a. Gregg and R. C. Lopez, Cambridge Univ Press.

Garces, M., A. Harris, C. Hetzer, J. Johnson, S. Rowland, E. Marchetti, and P. Okubo (2003), Infrasonic tremor observed at Kilauea Volcano, Hawai'i, *Geophysical Research Letters*, *30*, no.20, 24.

Garces, M., J. Aucan, D. Fee, P. Caron, M. Merrifield, R. Gibson, J. Bhattacharyya, and S. Shah (2006), Infrasound from Large Surf, *Geophysical Research Letters*, *33*(L05611), doi:10.1029/2005GL025085.

Garces, M., et al. (2008), Capturing the Acoustic Fingerprint of Stratospheric Ash Injection, *Eos, Transactions, American Geophysical Union*, *89*(40).

Garces, M. A. (1997), On the volcanic waveguide, *Journal of Geophysical Research, B, Solid Earth and Planets*, *102*(10), 22,547-522,564.

Garces, M. A. (2000), Theory of acoustic propagation in a multi-phase stratified liquid flowing within an elastic-walled conduit of varying cross-sectional area, *Journal of Volcanology and Geothermal Research*, *101*(1-2), 1-17.

Garces, M. A., M. T. Hagerty, and S. Y. Schwartz (1998a), Magma acoustics and time-varying melt properties at Arenal Volcano, Costa Rica, *Geophysical Research Letters*, *25*(13), 2293-2296.

Garces, M. A., R. A. Hansen, and K. G. Lindquist (1998b), Traveltimes for infrasonic waves propagating in a stratified atmosphere, *Geophysical Journal International*, *135*(1), 255-263.

Garces, M. A., S. R. McNutt, R. A. Hansen, and J. C. Eichelberger (2000), Application of wave-theoretical seismoacoustic models to the interpretation of explosion and

eruption tremor signals radiated by Pavlof Volcano, Alaska, *Journal of Geophysical Research, B, Solid Earth and Planets*, *105*(2), 3039-3058.

Gibson, R. G., and D. E. Norris (2002), Development of an infrasound propagation modeling tool kit*Rep.*, DTRA-TR-99–47 pp, Defense Threat Reduction Agency, Fort Belvoir, VA, 22060-6201.

Gibson, R. G., D. E. Norris, and D. P. Drob (2008), Investigation of the effects of fine-scale atmospheric inhomogeneities on infrasound propagation, *Proceedings of the 30th Seismic Research Review—Ground-Based Nuclear Explosion Monitoring Technologies*, *2*(LA-UR-08-05261), 872–881.

Goerke, V. H., J. M. Young, and R. K. Cook (1965), Infrasonic Observations of the May 16, 1963, Volcanic Explosion on the Island of Bali, *J. Geophys. Res.*, *70*(24), 6017-6022.

Green, D. N., and J. Neuberg (2005), Seismic and infrasonic signals associated with an unusual collapse event at the Soufriere Hills volcano, Montserrat, *Geophysical Research Letters*, *32*(7).

Green, D. N., and J. Neuberg (2006), Waveform classification of volcanic low-frequency earthquake swarms and its implication at Soufriere Hills Volcano, Montserrat, *Journal of Volcanology and Geothermal Research*, *153*(1-2), 51-63.

Hall, M. L., C. Robin, B. Beate, P. Mothes, and M. Monzier (1999), Tungurahua Volcano, Ecuador; structure, eruptive history and hazards, *Journal of Volcanology and Geothermal Research*, *91*(1), 1-21.

Ham, F. M., T. A. Leeney, H. M. Canady, and J. C. Wheeler (1999), Discrimination of volcano activity and mountain associated waves using infrasonic data and a backpropagation neural network, *Applications And Science Of Computational Intelligence Ii*, *3722*, 344-356.

Harris, A., and M. Ripepe (2007), Synergy of multiple geophysical approaches to unravel explosive eruption conduit and source dynamics - A case study from Stromboli, *Chemie Der Erde-Geochemistry*, *67*(1), 1-35.

Holcomb, R. T. (1987), Eruptive history and long-term behavior of Kilauea Volcano, in *Volcanism in Hawaii* edited by R. W. Decker, T. L. Wright and P. H. Stauffer, pp. chap. 12., 261-350.

Houghton, B. F., D. A. Swanson, J. Rausch, and S. A. Fagents (2008), Tephra dispersal during explosive events of the 2008 eruption of Halema'uma'u Crater, Kilauea, paper presented at American Geophysical Union, Fall Meeting 2008.

Howe, M. S. (1998), *Acoustics of Fluid–Structure Interactions*, 560 pp., Cambridge University Press.

James, M. R., S. J. Lane, and B. A. Chouet (2006), Gas slug ascent through changes in conduit diameter: Laboratory insights into a volcano-seismic source process in low-viscosity magmas, *Journal Of Geophysical Research-Solid Earth*, *111*(B5).

Jaupart, C., and S. Vergniolle (1988), Laboratory models of Hawaiian and Strombolian eruptions, *Nature*, *331*(6151), 58-60.

Johnson, D. H., and D. E. Dudgeon (1992), *Array Signal Processing: Concepts and Techniques*, Simon & Schuster

Johnson, J., R. Aster, K. R. Jones, P. Kyle, and B. McIntosh (2008a), Acoustic source characterization of impulsive Strombolian eruptions from the Mount Erebus lava lake, *Journal of Volcanology and Geothermal Research*, *177*(3), 673-686.

Johnson, J. B. (2003), Generation and propagation of infrasonic airwaves from volcanic explosions, *Journal of Volcanology and Geothermal Research*, *121*(1-2), 1-14.

Johnson, J. B. (2007), On the relation between infrasound, seismicity, and small pyroclastic explosions at Karymsky Volcano, *Journal Of Geophysical Research-Solid Earth*, *112*(B8).

Johnson, J. B., R. C. Aster, and P. R. Kyle (2004), Volcanic eruptions observed with infrasound, *Geophysical Research Letters*, *31*(14).

Johnson, J. B., M. C. Ruiz, J. M. Lees, and P. Ramon (2005), Poor scaling between elastic energy release and eruption intensity at Tungurahua Volcano, Ecuador, *Geophysical Research Letters*, *32*, no.15, 15.

Johnson, J. B., J. M. Lees, A. Gerst, D. Sahagian, and N. Varley (2008b), Long-period earthquakes and co-eruptive dome inflation seen with particle image velocimetry, *Nature*, *456*(7220), 377-381.

Jones, K. R., J. B. Johnson, R. Aster, P. R. Kyle, and W. C. McIntosh (2008), Infrasonic tracking of large bubble bursts and ash venting at Erebus Volcano, Antarctica, *Journal Of Volcanology And Geothermal Research*, *177*(3), 661-672.

Jones, M., J. Riley, and T. Georges (1986), A versatile three-dimensional Hamiltonian ray—tracing program for acoustic waves in the atmosphere above irregular terrain *Rep.*, Wave Propagation Laboratory, Boulder, Colorado.

Kinsler, L. E., A. R. Frey, A. B. Coppens, and J. V. Sanders (1982), *Fundamentals of Acoustics*, Third Edition ed., 480 pp., John Wiley and Sons.

Konstantinou, K. I., and V. Schlindwein (2002), Nature, wavefield properties and source mechanism of volcanic tremor: a review, *Journal of Volcanology and Geothermal Research*, *119*, 161-187.

Kumagai, H., and B. A. Chouet (2000), Acoustic properties of a crack containing magmatic or hydrothermal fluids, *Journal Of Geophysical Research-Solid Earth*, *105*(B11), 25493-25512.

Kumagai, H., et al. (2007), Enhancing volcano-monitoring capabilities in Ecuador, *Eos, Transactions, American Geophysical Union*, *88*(23), 245-246.

Larsen, J., C. Neal, P. Webley, J. Freymueller, M. Haney, S. R. McNutt, D. Schneider, S. Prejean, J. Schaefer, and R. Wessels (2009), Eruption of Alaska volcano breaks historic pattern, *Eos, Transactions, American Geophysical Union*, *90*(20), 173-174.

Le Pichon, A., E. Blanc, and D. Drob (2005a), Probing high-altitude winds using infrasound, *Journal of Geophysical Research-Atmospheres*, *110*(D20).

Le Pichon, A., J. Vergoz, E. Blanc, J. Guilbert, L. Ceranna, L. Evers, and N. Brachet (2009), Assessing the performance of the International Monitoring System's infrasound network: Geographical coverage and temporal variabilities, *Journal of Geophysical Research-Atmospheres*, *114*.

Le Pichon, A., P. Herry, P. Mialle, J. Vergoz, N. Brachet, M. Garces, D. Drob, and L. Ceranna (2005b), Infrasound associated with 2004-2005 large Sumatra earthquakes and tsunami, *Geophysical Research Letters*, *32*(19).

Le Pichon, A., E. Blanc, D. Drob, S. Lambotte, J. X. Dessa, M. Lardy, P. Bani, and S. Vergniolle (2005c), Infrasound monitoring of volcanoes to probe high-altitude winds, *Journal of Geophysical Research-Atmospheres*, *110*(D13).

Lighthill, M. J. (1954), On Sound Generated Aerodynamically. II. Turbulence as a Source of Sound, *Proc. R. Soc. Lond.*, *A 222*, 1-32.

Lighthill, M. J. (1978), *Waves in fluids*, 496 pp., Cambridge University Press.

Liszka, L., and K. Waldemark (1995), High resolution observations of infrasound generated by the supersonic flights of Concorde, *Journal Of Low Frequency Noise & Vibration*, *14*(4), 181-192.

Lockwood, J. P., J. J. Dvorak, T. T. English, R. Y. Koyanagi, A. T. Okamura, M. L. Summers, and W. R. Tanigawa (1987), Mauna Loa 1974-1984; a decade of intrusive and extrusive activity, edited by R. W. Decker, T. L. Wright and P. H. Stauffer, U. S. Geological Survey, Reston.

Mangan, M. T., C. C. Heliker, T. N. Mattox, J. P. Kauahikaua, and R. T. Helz (1995), Episode 49 of the Pu'u 'O'o-Kupaianaha eruption of Kilauea volcano; breakdown of a steady-state eruptive era, *Bulletin of Volcanology*, *57*(2), 127-135.

Marchetti, E., M. Ripepe, A. J. L. Harris, and D. Delle Donne (2009), Tracing the differences between Vulcanian and Strombolian explosions using infrasonic and thermal radiation energy, *Earth and Planetary Science Letters*, *279*(3-4), 273-281.

Matoza, R. S., M. A. H. Hedlin, and M. A. Garces (2007), An infrasound array study of Mount St. Helens, *Journal of Volcanology and Geothermal Research*, *160*, 249-262.

Matoza, R. S., D. Fee, and M. Garces (in review), Infrasonic tremor wavefield of the Pu‘u ¯ O‘¯o crater complex and lava tube system, Hawaii, in April 2007, *J. Geophys. Res.*

Matoza, R. S., D. Fee, M. A. Garces, J. M. Seiner, P. A. Ramon, and M. A. H. Hedlin (2008), Infrasonic jet noise from volcanic eruptions, *Geophysical Research Letters*.

Matoza, R. S., D. Fee, M. A. Garces, J. M. Seiner, P. A. Ramon, and M. A. H. Hedlin (2009a), Infrasonic jet noise from volcanic eruptions, *Geophysical Research Letters*, *36*(L08303).

Matoza, R. S., M. A. Garces, B. A. Chouet, L. D'Auria, M. A. H. Hedlin, C. De Groot-Hedlin, and G. P. Waite (2009b), The source of infrasound associated with long-period events at Mount St. Helens, *Journal Of Geophysical Research-Solid Earth*, *114*.

McNamara, D. E., and R. P. Buland (2004), Ambient noise levels in the continental United States, *Bulletin of the Seismological Society of America*, *94*(4), 1517-1527.

McNutt, S. R., K. M. Arnoult, C. A. Szuberla, and S. D. Stihler (2008), Preliminary Seismic, Infrasound and Lightning Observations of the July 2008 Eruptions of Okmok Volcano, Alaska, paper presented at American Geophysical Union, Fall Meeting 2008.

McNutt, S. R., K. M. Arnoult, J. V. Olson, C. Szuberla, M. E. West, and E. Clark (2009), Local Infrasound Observations of the Explosive Eruptions of Redoubt Volcano, Alaska, March-April 2009, paper presented at American Geophysical Union, Fall Meeting 2009.

Melton, B. S., and L. F. Bailey (1957), Multiple signal correlators, *Geophysics*, *22*, 565.

Mikumo, T. (1968), Atmospheric pressure waves and tectonic deformation associated with the Alaskan earthquake of March 28, 1964, *J. Geophys. Res.*, *73*, 2009-2025.

Mikumo, T., and B. A. Bolt (1985), Excitation mechanism of atmospheric pressure waves from the 1980 Mount St. Helens eruption, *Geophys. J. R. Astr. Soc*, *81*, 445-461.

Moran, S. C., R. S. Matoza, M. A. Garces, M. A. H. Hedlin, D. Bowers, W. E. Scott, D. R. Sherrod, and J. W. Vallance (2008), Seismic and acoustic recordings of an unusually large rockfall at Mount St. Helens, Washington, *Geophysical Research Letters*, *35*(19).

Morrissey, M. M., and L. G. Mastin (2000), Vulcanian Eruptions, in *Encyclopedia of Volcanoes*, edited by H. Sigurdsson, Academic Press.

Morrissey, M. M., and B. A. Chouet (2001), Trends in long-period seismicity related to magmatic fluid compositions, *Journal of Volcanology and Geothermal Research*, *108*(1-4), 265-281.

Morse, P. M., and K. U. Ingard (1968), *Theoretical Acoustics*, 927 pp., Princeton University Press, Princeton, New Jersey.

Ogden, D. E., G. A. Glatzmaier, and K. H. Wohletz (2008a), Effects of vent overpressure on buoyant eruption columns: Implications for plume stability, *Earth and Planetary Science Letters*, *268*(3-4), 283-292.

Ogden, D. E., K. H. Wohletz, G. A. Glatzmaier, and E. E. Brodsky (2008b), Numerical simulations of volcanic jets: Importance of vent overpressure, *Journal of Geophysical Research-Solid Earth*, *113*(B2).

Okamura, A. T., J. J. Dvorak, R. Y. Koyanagi, and W. R. Tanigawa (1988), Surface deformation during dike propagation, edited by E. W. Wolfe, U. S. Geological Survey, Reston.

Olson, J. V., and C. A. Szuberla (2008), Processing Infrasonic Array Data, in *Handbook of Signal Processing in Acoustics*, edited by D. Havelock, S. Kuwano and M. Vorlander, pp. 1487-1496, Springer, New York.

Orr, T. R., M. R. Patrick, K. M. Wooten, S. D.A., T. Elias, A. J. Sutton, D. C. Wilson, and M. P. Poland (2008), Explosions, tephra, and lava: a chronology of the 2008 summit eruption of Kīlauea Volcano, Hawai`i, *Eos, Transactions, American Geophysical Union*, *89*(53), Fall Meet. Suppl., Abstract V11B-2018.

Patrick, M. R., D. Wilson, D. Fee, T. Orr, and D. Swanson (in review), Shallow degassing events as a trigger for very-long-period seismicity at Kīlauea Volcano, Hawai‘i, *Bulletin of Volcanology*.

Patrick, M. R., A. J. L. Harris, M. Ripepe, J. Dehn, D. A. Rothery, and S. Calvari (2007), Strombolian explosive styles and source conditions: insights from thermal (FLIR) video, *Bulletin Of Volcanology*, *69*(7), 769-784.

Perret, F. A. (1950), Volcanological Observations, *Carnegie Inst. Wash. Publ.*

Petersen, T., S. De Angelis, G. Tytgat, and S. R. McNutt (2006), Local infrasound observations of large ash explosions at Augustine Volcano, Alaska, during January 11-28, 2006, *Geophysical Research Letters*, *33*(12).

Pierce, A. D. (1981), *Acoustics - An introduction to Its Physical Principles and Applications*, McGraw-Hill, New York.

Poland, M., A. O. Miklius, T., J. Sutton, C. Thornber, and D. Wilson (2008), New Episodes of Volcanism at Kilauea Volcano, Hawaii, *Eos Trans.*, *89*(5), doi:10.1029/2008EO050001.

Poland, M. P., A. J. Sutton, and T. M. Gerlach (2009), Magma degassing triggered by static decompression at Kilauea Volcano, Hawai'i, *Geophysical Research Letters*, *36*.

Prata, A. J. (2009), Satellite detection of hazardous volcanic clouds and the risk to global air traffic, *Natural Hazards*, *51*(2), 303-324.

Prata, A. J., G. Gangale, L. Clarisse, and F. Karagulian (submitted), Ash and sulphur dioxide in the 2008 eruptions of Okmok and Kasatochi - insights from high spectral resolution satellite measurements, *J. Geophys. Res.*

ReVelle, D. O. (1975), Studies of sounds from meteors, *Sky and Telescope*, *49*, 87–91.

Richards, A. F. (1963), Volcanic sounds, investigation and analysis, *Journal Of Geophysical Research-Solid Earth*, *68*, 919-928.

Riedel, K. S., and A. Sidorenko (1995), Minimum Bias Multiple Taper Spectral Estimation, *IEEE Trans. Sig.Proc.*(43), 188-195.

Ripepe, M., and E. Marchetti (2002), Array tracking of infrasonic sources at Stromboli volcano, *Geophysical Research Letters*, *29*(22), 2076.

Ripepe, M., P. Poggi, T. Braun, and E. Gordeev (1996), Infrasonic waves and volcanic tremor at Stromboli, *Geophysical Research Letters*, *23*(2), 181-184.

Ripepe, M., D. Delle Donne, G. Lacanna, E. Marchetti, and G. Ulivieri (2009a), The onset of the 2007 Stromboli effusive eruption recorded by an integrated geophysical network, *Journal Of Volcanology And Geothermal Research*, *182*(3-4), 131-136.

Ripepe, M., S. De Angelis, G. Lacanna, P. Poggi, C. Williams, E. Marchetti, D. Delle Donne, and G. Ulivieri (2009b), Tracking Pyroclastic Flows at Soufrière Hills Volcano, *Eos Trans.*, *90*(27), doi:10.1029/2009EO270001.

Rockwell, D., and E. Naudascher (1979), Self-Sustained Oscillations of Impinging Free Shear Layers, *Annual Review of Fluid Mechanics*, *11*, 67-94.

Rossiter, J. E. (1964), Wind-tunnel experiments on the flow over rectangular cavities at subsonic and transonic speeds, *G. B. R. Aircr. Establ. Tech. Rep. 64037; also G. B. Aeronaut. Res. Counc. Rep. Memo.*(3438), 32.

Ruiz, M., J. M. Lees, and J. B. Johnson (2006), Source constraints of Tungurahua volcano explosion events, *Bulletin of Volcanology*, *68*(5), 480-490.

Seiner, J. M. (1984), Advances in high speed jet aeroacoustics, *AIAA Pap*, *84-2275*.

Smithsonian, I. (2006), Tungurahua, in *Bulletin of the Global Volcanism Network (BVGN)*, edited.

Smithsonian, I. (2008a), Kasatochi, *Bulletin of the Global Volcanism Network (BVGN)*, *33*(07).

Smithsonian, I. (2008b), Okmok, *Bulletin of the Global Volcanism Network (BVGN)*, *33*(06).

Solovitz, S. A., and L. G. Mastin (2009), Experimental study of near-field air entrainment by subsonic volcanic jets, *Journal Of Geophysical Research-Solid Earth*, *114*.

Sparks, R. S. J., M. I. Bursik, S. N. Carey, J. S. Gilbert, L. S. Glaze, H. Siggurdsson, and A. W. Woods (1997), *Volcanic Plumes*, 574 pp., John Wiley and Sons, New York.

Stearns, H. T. (1925), The 1924 eruption of the Hawaiian volcano, *Scientific American*, *132*, 242-243.

Steffke, A., D. Fee, M. Garces, and A. Harris (in press), Identifying eruption chronologies, plume heights and eruption styles at Tungurahua volcano: Integrating thermal infrared satellite and infrasound data, *Journal of Volcanology and Geothermal Research*.

Steffke, A., D. Fee, M. Garces, and A. Harris (in review), Identifying eruption chronologies, plume heights and eruption styles at Tungurahua volcano: Integrating thermal infrared satellite and infrasound data, *Journal Of Volcanology And Geothermal Research*.

Sutherland, L. C., and H. E. Bass (2004), Atmospheric absorption in the atmosphere up to 160 km, *Journal of the Acoustical Society of America*, *115*(3), 1012-1032.

Swanson, D., K. Wooten, and T. Orr (2009), Buckets of ash track tephra flux From Halema'uma'u Crater, Hawai'i, *Eos, Transactions, American Geophysical Union*, *90*(46), 427.

Szuberla, C. A. L., K. M. Arnoult, and J. V. Olson (2006), Discrimination of near-field infrasound sources based on time-difference of arrival information, *Journal Of The Acoustical Society Of America*, *120*(3), EL23-EL28.

Tahira, M., M. Nomura, Y. Sawada, and K. Kamo (1996), Infrasonic and acoustic-gravity waves generated by the Mount Pinatubo eruption of June 15, 1991, in *Fire and Mud*, edited by C. G. Newhall and R. S. Punongbayan.

Tam, C. K. W. (1995), Supersonic Jet Noise, *Annual Review Of Fluid Mechanics*, *27*, 17-43.

Tam, C. K. W. (1998), Jet noise: Since 1952, *Theoretical And Computational Fluid Dynamics*, *10*(1-4), 393-405.

Tam, C. K. W., M. Golebiowski, and J. M. Seiner (1996), On the two components of turbulent mixing noise from supersonic jets, *AIAA Pap*, 96-1716.

Tam, C. K. W., K. Viswanathan, K. K. Ahuja, and J. Panda (2008), The sources of jet noise: experimental evidence, *Journal Of Fluid Mechanics*, *615*, 253-292.

Thomas, C. (2008), Array Signal Processing, in *Handbook of Signal Processing in Acoustics*, edited by D. Havelock, S. Kuwano and M. Vorlander, pp. 1655-1665, Springer, New York.

Vergniolle, S., and M. Mangan (2000), Hawaiian and Strombolian Eruptions, in *Encyclopedia of Volcanoes*, edited by H. Sigurdsson, Academic Press.

Vergniolle, S., and J. Caplan-Auerbach (2006), Basaltic thermals and subplinian plumes: Constraints from acoustic measurements at Shishaldin volcano, Alaska, *Bulletin of Volcanology*, *68*(7-8), 611-630.

Vergniolle, S., G. Brandeis, and J. C. Mareschal (1996), Strombolian explosions .2. Eruption dynamics determined from acoustic measurements, *Journal of Geophysical Research-Solid Earth*, *101*(B9), 20449-20466.

Walker, K. T., and M. A. H. Hedlin (2010), A Review of Wind-Noise Reduction Methodologies, in *Infrasound Monitoring for Atmospheric Studies*, edited by A. Le Pichon, E. Blanc and A. Hauchecorne, pp. 141-182, Springer.

Wang, M. (2005), Computation of trailing-edge aeroacoustics with vortex shedding, *Center for Turbulence Research Annual Research Briefs*, 379-388.

Waxler, R., and K. E. Gilbert (2006), The radiation of atmospheric microbaroms by ocean waves, *Journal Of The Acoustical Society Of America*, *119*(5), 2651-2664.

Waxler, R., K. E. Gilbert, and C. Talmadge (2008), A theoretical treatment of the long range propagation of impulsive signals under strongly ducted nocturnal conditions, *Journal of the Acoustical Society of America*, *124*(5), 2742-2754.

Waxler, R., C. L. Talmadge, S. Dravida, and K. E. Gilbert (2006), The near-ground structure of the nocturnal sound field, *Journal Of The Acoustical Society Of America*, *119*(1), 86-95.

Waythomas, C. F., D. J. Schneider, and S. G. Prejean (2008), The 2008 Eruption of Kasatochi Volcano, Central Aleutian Islands, Alaska: Reconnaissance Observations and Preliminary Physical Volcanology, paper presented at American Geophysical Union, Fall Meeting 2008.

Whitaker, R. W., and D. E. Norris (2008), Infrasound Propagation, in *Handbook of Signal Processing in Acoustics*, edited by D. Havelock, S. Kuwano and M. Vorlander, pp. 1497-1519, Springer, New York.

Willis, M., M. Garces, C. Hetzer, and S. Businger (2004), Infrasonic observations of open ocean swells in the Pacific: Deciphering the song of the sea, *Geophysical Research Letters*, *31*(19).

Wilson, C. R. (1967), Infrasonic pressure waves from aurora: a shock wave model, *Nature*, *216*(131-133).

Wilson, C. R., S. Nichparenko, and R. B. Forbes (1966), Evidence of two sound channels in the polar atmosphere from infrasonic observations of the eruption of an Alaskan volcano, *Nature*, *211*, 163-165.

Wilson, D., T. Elias, T. Orr, M. Patrick, J. Sutton, and D. Swanson (2008), Small Explosion From New Vent at Kilauea's Summit, *Eos Trans.* , *89*(22), doi:10.1029/2008EO220003.

Wilson, L., R. S. J. Sparks, H. T.C., and W. N.D (1978), The Control of Volcanic Column Heights by Eruption Energetics and Dynamics, *Journal of Geophysical Research-Solid Earth*, *83*(B4), 1829-1836.

Woods, A. W. (1995), The Dynamics Of Explosive Volcanic-Eruptions, *Reviews of Geophysics*, *33*(4), 495-530.

Woods, A. W., and S. Self (1992), Thermal Disequilibrium At The Top Of Volcanic Clouds And Its Effect On Estimates Of The Column Height, *Nature*, *355*(6361), 628-630.

Woods, A. W., and S. M. Bower (1995), The Decompression Of Volcanic Jets In A Crater During Explosive Volcanic-Eruptions, *Earth and Planetary Science Letters*, *131*(3-4), 189-205.

Woulff, G., and T. R. McGetchin (1975), Acoustic Noise from Volcanoes: Theory and Experiment, *Geophys. J. R. Astr. Soc*, *45*, 601-616.

Yamasato, H. (1997), Quantitative analysis of pyroclastic flows using infrasonic and seismic data at Unzen volcano, Japan, *Journal of Physics of the Earth*, *45*(6), 397-416.

Yamasato, H. (1998), Nature of Infrasonic Pulse Accompanying Low Frequency Earthquake at Unzen Volcano, Japan, *Bull. Volcanol. Soc. Japan*, *43*, 1-13.

Yokoo, A., T. Tameguri, and M. Iguchi (2009), Swelling of a lava plug associated with a Vulcanian eruption at Sakurajima Volcano, Japan, as revealed by infrasound record: case study of the eruption on January 2, 2007, *Bulletin of Volcanology*, *71*(6), 619-630.